

The University of Southern Queensland
Faculty of Health, Engineering and Sciences

**Restart of a 2D Hypersonic Inlet at Mach 6 using Active
Slot Flow Control**

A dissertation submitted by

Lachlan Noller

in fulfilment of the requirements of

ENG4111 and 4112 Research Project

towards the degree of

Bachelor of Engineering (Honours) BENH

Submitted: October, 2019

Abstract

Optimal scramjet inlet performance is essential for sustained hypersonic flight. Variations from the ideal inlet operating conditions will lead to decreased air compression efficiency. Severe decreases in inlet performance can occur if a scramjet inlet ‘unstarts’. Scramjet engine unstart can occur if the combustion induced pressure rise is too high, or if the angle of attack is beyond its operating limits, or if flight at off-design Mach numbers is attempted. Past research has primarily focused on the development of techniques which prevent unstart from occurring. However, recent research has focused on methods which restart the inlet if it has unstarted. This work primarily focuses on developing a restart mechanism which is able to restart a 2D single ramp hypersonic inlet at Mach 6. Initial investigations were conducted using computational simulation methods to develop potential restart techniques. Experiments were conducted in the TUSQ hypersonic wind tunnel to verify the accuracy of the computational simulations. Results from simulations demonstrated two potential methods of inlet restarting exist: throat suction and sonic injection near the start of the compression surface. Experimental results for the started scramjet inlet matched the simulation reasonably well, however some differences were observed due to transitional boundary layer effects which were not accounted for in the simulations. Opportunities for further work include experimental testing of the proposed restart techniques along with further development of numerical simulations to achieve a more faithful representation of the experimental results.

University of Southern Queensland
Faculty of Health, Engineering & Sciences

ENG4111/2 <i>Research Project</i>
--

Limitations of Use

The Council of the University of Southern Queensland, its Faculty of Health, Engineering & Sciences, and the staff of the University of Southern Queensland, do not accept any responsibility for the truth, accuracy or completeness of material contained within or associated with this dissertation.

Persons using all or any part of this material do so at their own risk, and not at the risk of the Council of the University of Southern Queensland, its Faculty of Health, Engineering & Sciences or the staff of the University of Southern Queensland.

This dissertation reports an educational exercise and has no purpose or validity beyond this exercise. The sole purpose of the course pair entitled “Research Project” is to contribute to the overall education within the student’s chosen degree program. This document, the associated hardware, software, drawings, and other material set out in the associated appendices should not be used for any other purpose: if they are so used, it is entirely at the risk of the user.

Executive Dean

Faculty of Health, Engineering & Sciences

Certification of Dissertation

I certify that the ideas, designs and experimental work, results, analyses and conclusions set out in this dissertation are entirely my own effort, except where otherwise indicated and acknowledged.

I further certify that the work is original and has not been previously submitted for assessment in any other course or institution, except where specifically stated.

Lachlan Noller



Acknowledgements

I must first thank all of my supervisors. David, your guiding hand throughout this whole journey has been invaluable to my learning over the past year. Despite my endless annoying questions and coming to you with my tail between my legs because I have damaged yet another piece of equipment, your patience and easy going spirit has made my thesis experience extremely enjoyable. Fabs, I cannot even begin to thank you for all your help when it comes to running Eilmer (and Linux in general). Regardless of your extreme work load or location around the globe, you were always happy to make the time to look at where I was going wrong with things (but never hesitant to make a cheeky comment). Byrenn, if I could've had a someone to write my thesis you would be the first person I would hire. Your extensive knowledge in all things computers including Latex and Matlab has been invaluable in constructing my thesis. My experiments would have also never happened without your help running the tunnel, setting up the DAQ and Schlieren.

From a manufacturing perspective, a huge thanks must go to the workshop staff Bryan, Oliver and Nathan and also to the Z block technical staff Terry and Graham. My endless trips to make "just one more part" were never turned away and always happily taken on.

On a more general note, my parents Mark and Kerry require endless praise for dealing with all my complaining and always reminding me to chase what I enjoy doing. Also, thanks must go to Liam Channer for his friendship over the past three years from talking

over assignment/thesis issues to throwing general banter at one another. Finally, I would like to thank my girlfriend Amy for taking a back-seat while I've been on my thesis journey. Her unending support and words of encouragement have kept me from losing focus and motivation.

Table of Contents

Abstract	i
Acknowledgements	iv
List of Figures	x
List of Tables	xv
Nomenclature	xvi
Chapter 1 Introduction	1
1.1 Background	1
1.2 Problem Statement	5
1.3 Dissertation Outline	6
Chapter 2 Background	7
2.1 Scramjet Overview	8
2.1.1 Scramjet Operation	8
2.1.2 The Inlet	9
2.1.3 Inlet Starting	10
2.1.4 The Isolator	11
2.1.5 Inlet/Isolator Unstart	14
2.2 Hypersonic Fundamentals	15
2.3 Shock Reflections	20
2.4 Shock Interactions	20

2.5	Viscous Interactions	21
2.5.1	Hypersonic Shock Wave/Boundary Layer Interactions	25
2.6	Schlieren flow visualisation	28
Chapter 3	Literature Review	30
3.1	Unstart Control	31
3.2	Restart Control	33
3.3	Literature Gap	35
Chapter 4	Model Design	36
4.1	Model Geometry	37
4.2	Ramp boundary layer thickness	40
4.3	Model Scale	41
4.4	Transverse Injection	42
Chapter 5	Numerical Methodology	45
5.1	Numerical Testing Procedures	46
5.2	Eilmer4	46
5.3	Grid Definition	47
5.4	Boundary Condition Definition	49
5.5	Simulation Sequence	50
5.6	Mesh Independence Study	50
Chapter 6	Numerical Results and Discussion	52
6.1	Mesh Independence Study	53
6.2	Self-Started Inlet	54
6.3	Unstart Injection	58
6.4	Unstart Sustainment	60
6.5	Restart Mechanisms	62
6.5.1	Throat Suction	62
6.5.2	Mid-Ramp Injection	63
6.5.3	Tip Injection	65
6.6	Restart	66

6.6.1	Throat Suction	66
6.6.2	Mid-Ramp Injection	67
6.6.3	Tip Injection	69
6.7	Evaluation of Restart Mechanisms	71
Chapter 7	Experimental Methodology	72
7.1	Test Model	73
7.2	Test Facility	75
7.3	Experimental Testing Procedures	77
7.4	Instrumentation and Setup	79
7.4.1	Schlieren Visualisation	79
7.4.2	Ramp Pressure Transducers	80
7.4.3	Data acquisition and calibration	81
Chapter 8	Experimental Results and Discussion	82
8.1	Self-Started Inlet	83
8.1.1	Initial Model Configuration	83
8.1.2	Second Model Configuration	85
8.1.3	Final Model Configuration	88
8.2	Unstart Injection	90
Chapter 9	Results Analysis and Discussion	91
9.1	Boundary Layer Thickness Comparison	92
9.2	Shock Angle Comparison	93
9.3	Ramp Pressure Comparison	94
9.4	Conclusion of Results	98
Chapter 10	Conclusion	100
10.1	Review of Thesis	100
10.2	Key Findings/Outcomes	101
10.3	Recommendations for Further Work	103
Bibliography		104

Appendix	109
Appendix A - Project Specification	110
Appendix B - Project Requirements	112
Appendix C - Project Plan	113
Appendix D - Risk Assessment	114
Appendix E - MATLAB Code	116
A.1 Scramjet Inlet Geometry Calculations	116
A.2 Oblique Shock Wave Angle Function	120
A.3 Viscosity Function	121
Appendix F - Model Drawings	123
Appendix G - Model Modifications	129
Tip Injection	129
Side Wall Thickness	131
Window Design	133
Model Roof	135
Appendix H - Eilmer4 Input Scripts	137
Self-Started Inlet Script	137
Unstart Injection Inlet Script	140
Unstarted Inlet Script	144
Restart Mechanism Inlet Script	147
Restarted Inlet Script	150

List of Figures

1.1	Specific impulse variation with flight Mach number for engines with hydrogen fuel	2
1.2	Boeing X51-A WaveRider scramjet demonstrator	3
2.1	Two dimensional schematic of a ramjet engine	8
2.2	Two dimensional schematic of a scramjet engine	9
2.3	Flow and shock geometry of an inlet at designed Mach number, higher than designed Mach number and lower than designed Mach number . .	9
2.4	Scramjet inlet station definitions	10
2.5	Starting and maximum contraction ratio limits	11
2.6	Single normal shock forming in a constant area duct	12
2.7	Flow pattern and static wall pressure distribution of a complete normal shock train	13
2.8	Flow pattern and static wall pressure distribution of a complete oblique shock train	13
2.9	Unstart due to separation bubble at inlet throat	15
2.10	Subsonic particle emitting sound waves	16
2.11	Supersonic particle emitting sound waves depicting Mach cone	17
2.12	Comparison between Mach wave angle and Oblique wave angle	17
2.13	Oblique shock wave notation	18
2.14	Solid reflection of a shock wave from a solid boundary	20
2.15	Types of shock interaction	21

2.16	Temperature profile in a hypersonic boundary layer	22
2.17	Mapping of a compressible boundary layer to an incompressible boundary layer flow	23
2.18	Solution of the Blasius equation	24
2.19	Compressible boundary layer profiles	25
2.20	Shock wave/boundary layer interaction examples	26
2.21	Planar shock wave / boundary layer interaction	27
2.22	Expansion wave formed by a downward turning surface	28
2.23	Schematic of a typical Schlieren setup	29
2.24	Schlieren image of wedge in supersonic flow	29
4.1	SOL Inlet Geometry	39
4.2	Displacement of leading shock wave on inlet compression ramp due to boundary layer formation	41
4.3	Mach cone formed by the TUSQ Mach 6 nozzle	42
4.4	Schematic of transverse injection flow field	43
4.5	Comparison of upstream separation distance and penetration height for different pressure ratios	43
4.6	Pressure ratio vs transverse direction jet penetration varying with slot widths	44
5.1	Blocking of inlet mesh	47
5.2	Mesh constructed inside inlet blocks with clustering towards constant temperature no-slip walls	48
5.3	Inlet mesh with Tangential Injection mid-ramp	49
5.4	Blocks and boundary conditions for the computational simulations	50
5.5	Location of averaged data points along isolator midline	51
6.1	Plotted results from mesh independence study	53
6.2	Pressure contour of inviscid simulation of inlet at 5 ms having reached steady conditions	54
6.3	Location of inviscid data collection points	55

6.4	Schlieren of simulation showing impulsive starting of inlet	56
6.5	Self-started inlet pressure variation over 50 ms flow duration	57
6.6	Temperature contours of self-started inlet simulation at various times . .	58
6.7	Temperature contours of the inlet at 5 ms after initiation of unstart injection for various unstart injection pressures	59
6.8	Unstart injection pressure variation due to isolator flow blockage at data locations 1 and 8 for the 100 kPa injection pressure	60
6.9	Temperature contours from two inlet cases at 5 ms after removal of the unstart injection	61
6.10	Density contours of started inlet and sustained-unstarted inlet	62
6.11	Temperature contour of inlet throat restart suction mechanism using suction at 200 Pa at 10 ms	63
6.12	Restart suction mechanism pressure variation	63
6.13	Temperature contour of mid-ramp restart injection at 1 ms with a 100 kPa injection using various injection angles	64
6.14	Temperature contours for the tip injection case at various times relative to the initiation of the mechanism with 100 kPa injection pressure . . .	65
6.15	Restart tip injection temperature variation	66
6.16	Temperature contour of inlet 5 ms after deactivation of inlet suction . .	67
6.17	Restart suction mechanism deactivation pressure variation	67
6.18	Temperature contours of inlets 5 ms after deactivation of the mid-ramp injection	68
6.19	Pressure variation at data location 6 with removal of mid-ramp injection	69
6.20	Temperature contours of restarted inlets 5 ms after deactivation of restart tip injection	70
6.21	Pressure variation at data location 8 with removal of various tip injection durations	70
7.1	Side view of initial model mounted in TUSQ hypersonic wind tunnel . .	73
7.2	Top view of initial model mounted in TUSQ hypersonic wind tunnel . .	74
7.3	Isometric rendering of experimental inlet model	74

7.4	General arrangement of the wind tunnel facility	75
7.5	TUSQ Mach 6 nozzle sketch	76
7.6	Barrel pressure history	76
7.7	Initial Model Ramp	78
7.8	Second model ramp	78
7.9	Final ramp configuration	79
7.10	Z-type Schlieren System	80
7.11	Mounting for pressure transducer	81
7.12	Cross-section of 3D printed ramp showing arrangement of transducer mounting	81
8.1	Run 915 at 30 ms flow duration	83
8.2	Run 915 barrel and test section pressure history	83
8.3	Run 916 at 30 ms flow duration	84
8.4	Run 916 barrel and test section pressure history	84
8.5	Reflected leading shock wave	85
8.6	Run 934 at 30 ms flow duration	86
8.7	Run 934 barrel and test section history	86
8.8	Raw experimental static pressure measurements over steady test dura- tion (refer to Figure 4.1 for positions of data locations)	87
8.9	Run 932 at 30 ms flow duration	88
8.10	Run 932 barrel and test section history	88
8.11	Wedge shielding injection components of final ramp configuration . . .	89
8.12	Run 933 Schlieren of self-started inlet prior to unstart injection and upon unstart injection at the isolator rear	90
8.13	Run 933 Schlieren of self-started isolator prior to unstart injection and upon unstart injection at the isolator rear	90
9.1	Comparison of simulation and experimental boundary layer thickness at steady state conditions	92
9.2	Comparison of simulation and experimental shock wave angles at steady state conditions	93

9.3	Simulated shock interaction and reflection in isolator	94
9.4	Comparison of pressure measurements obtained analytical, numerical and experimental results	95
9.5	Simulated density contour of started inlet indicating separation shock angle	95
9.6	Simulated pressure contour with data locations indicated	97
9.7	Comparison of simulation and experimental separation region location within the isolator	98
C.1	Project Plan	113
D.1	Risk Assessment Matrix	114
G.1	Injector plenum cross-section	129
G.2	Ramp tip modifications with 6 mm slot	129
G.3	Final ramp assembly side view	130
G.4	Final ramp assembly side view	130
G.5	Primary model test Schlieren visualisation result at 32 ms of flow duration	131
G.6	Modifications made to left hand side model stand	132
G.7	Modifications made to right hand side model stand	132
G.8	First window design	133
G.9	Second window design	134
G.10	Final window design	134
G.11	Run 928 Tunnel and Barrel pressure history.	135
G.12	Flow collapse progression	136

List of Tables

4.1	Free stream flow conditions for model inlet design	37
4.2	Summary of flow conditions for proposed inlet design	38
5.1	Front side location of 1mm wide injection/suction ports located in the x-direction from the ramp tip	48
6.1	Tabulated results from mesh independence study	53
6.2	Simulated vs Analytical inlet flow conditions	55
6.3	Pressures at data locations at 10 ms after restart suction activation . . .	63
6.4	Maximum pressure achieved upon removal of tip injection	71
7.1	Experimental Test Conditions	76
10.1	Risk Assessment	115

Nomenclature

a	Speed of sound (m/s)
A	Cross-sectional Area (m ²)
c	Speed of light (m/s)
c_o	Speed of light in a vacuum (m/s)
h_{pen}	Penetration height (m)
I_{sp}	Specific Impulse (Ns/kg)
M	Mach number
n	Refractive Index
P	Pressure (Pa)
\bar{q}	Momentum flux ratio
Pr	Prandtl number
R	Ideal gas constant (J/kgK)
Re	Reynolds Number
T	Temperature (K)
V	Velocity (m/s)
X_{upsep}	Upstream separation distance (m)
α	Spatial similarity variable
β	Oblique shock wave angle (°)
γ	Ratio of specific heats
δ	Boundary layer thickness (m)
θ	Deflection Angle (°)
μ	Mach Angle (°)

ρ	Density (kg/m ³)
Φ	Reflected Shock Angle (°)

Subscripts

<i>Kantrowitz</i>	Kantrowitz contraction ratio limit
<i>Isentropic</i>	Isentropic contraction ratio limit
<i>n</i>	Normal direction
<i>e</i>	Boundary layer edge
∞	Free stream
<i>inj</i>	Injection
<i>b</i>	Barrel

Acronyms

AJVG	Air Jet Vortex Generators
CFD	Computational Fluid Mechanics
CfH	Centre for Hypersonics
CR	Contraction Ratio
PIV	Particle Image Velocimetry
SOL	Shock-On-Lip condition
swbli	Shock wave/boundary layer interaction
TUSQ	USQ Hypersonic Wind Tunnel
UQ	University of Queensland
USQ	University of Southern Queensland

Chapter 1

Introduction

"Bite off more than you can chew, and then chew like hell."

- Peter Brock, 1945-2006

Contents

1.1	Background	1
1.2	Problem Statement	5
1.3	Dissertation Outline	6

1.1 Background

The ever growing interest to increase mankind's flight ability has led to the rapid growth of aircraft performance which has been enabled largely by development of new and advanced propulsion systems. The supersonic combustion ramjet (scramjet) engine is the current state of the art in hypersonic propulsion and promises to be the basis of future high speed aerospace flight. Further development of the scramjet would in theory provide superior

performance compared to the traditional solution of rocket propulsion, and may be able to achieve speeds between Mach 5 and Mach 25 (Curran & Murthy 2001).

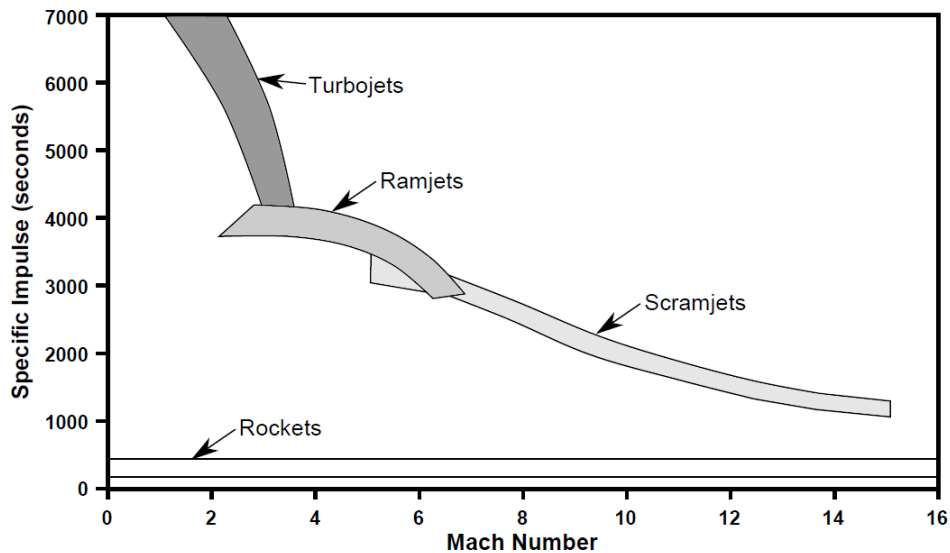


Figure 1.1: Specific impulse variation with flight Mach number for engines with hydrogen fuel adapted by Wise (2015)

Compared to rocket propulsion, air breathing engines have a higher specific impulse I_{sp} and enable significant weight savings as they are not required to carry oxidiser in the vehicle (Heiser, Pratt, Daley & Mehta 1994). Due to their potential high efficiency at high Mach numbers, there is significant research effort being invested in further developing scramjet technology. Whilst rockets are less efficient than air breathing engines, they have the ability to be used over a wide range of Mach numbers at both subsonic and supersonic conditions. The performance of air breathing engines depends greatly on their operating Mach number as seen in Figure 1.1. By using the kinetic energy of the flight vehicle, a supersonic vehicle with inlet compression can achieve the necessary compression effect, eliminating the need for internal compression mechanisms as used in traditional turbojet engines (Wise 2015). This however requires the vehicle to be brought to the operating speeds by other means of propulsion (Heiser et al. 1994). For example, the Boeing X-51A WaveRider scramjet illustrated in Figure 1.2 was carried aloft by a B-52 and then propelled to Mach 4.5 by a modified Lockheed Martin Army Tactical Missile System (ATACMS) rocket and after separating from this rocket, scramjet propulsion would take

over.

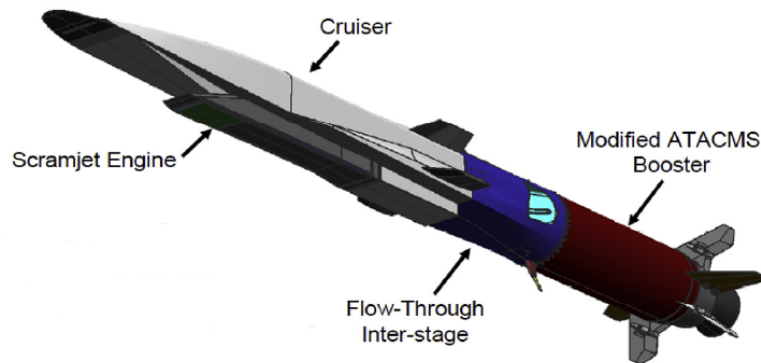


Figure 1.2: Boeing X51-A WaveRider scramjet demonstrator (Hank et al. 2008)

Travelling at hypersonic speeds presents a multitude of issues for scramjet design. Mixed compression inlets produce oblique shock waves to perform much of the air compression in a relatively efficient manner as well as reducing velocity suitable in the downstream combustor. Use of oblique shocks allows for improved total pressure recovery relative to normal shock waves. Unfortunately, all shock waves generate adverse pressure gradients which tend to cause boundary layer separation. Within the free-stream, these pressure gradients pose no issues for scramjet operation, but at locations where the pressure gradient along the engine surface induced by the shock wave is large, significant flow separation can occur. These shock wave/boundary layer interactions (swbli's) result in upstream thickening of boundary layers, displacing shock waves formed by the inlet. This leads to decreased scramjet efficiency and potentially the scramjet may produce no net thrust. At such a condition, the inlet is said to be 'unstarted'. Moreover, at the location of boundary layer separation, high localised heating occurs potentially resulting in inlet damage.

Unstart may occur if the scramjet-powered flight vehicle maneuvers beyond its acceptable angle of attack since inlet boundary layers and pressure gradients are sensitive to the flight attitude. When operating within the ramjet/ scramjet transition mode in flight Mach number ranges of 3-6 (Andreadis 2004) unstart can also be caused by thermal choking (Mashio, Kurashina, Bamba, Okimoto & Kaji 2001) triggered by increased heat release

in the combustor (Heiser et al. 1994). In 1966, the hybrid turbo-ramjet engine used to power the SR-71 Blackbird, capable of Mach 3.2 flight crashed due to engine cut-off induced by this particular form of inlet unstart (Graham 1996). Past and current research is focused on better understanding the unstart process and developing methods to better control, predict and prevent the unstart phenomenon.

The unstarted mode of inlet operation can actually be more stable than properly started mode so in more recent times, research has also focused on methods to restart the inlet if it has been unstarted. In 2011, the X51-A experienced inlet unstart when transitioning to scramjet propulsion. After detecting the unstart, the aircraft attempted to restart the inlet by orientating itself to optimise engine start conditions, but the attempted restart was unsuccessful (Li, Chang, Jiang, Yu, Bao, Song & Jiao 2018). Approaches to inlet restarting include variable geometry, inlet bleeding and energy addition (Chang, Fan, Bao, Yu & Shen 2019). However, many of these potential techniques require further research to verify their effectiveness.

1.2 Problem Statement

The motivation for this project is driven by the demand for a feasible method of scramjet inlet restarting, contributing to improved prospects for of sustained hypersonic flight. Though there is some literature on numerical simulation of hypersonic inlet restarting characteristics, there is little exploration of experimental models exhibiting an effective and feasible restart control method. The purpose of this project is to develop a practical method of active restart control.

The issue of first creating an unstarted inlet is to be addressed. The internal contraction of the inlet must be such that the inlet can self-start but can sustain a stable separation region upstream of the inlet throat. Once inducing a deliberate unstart, the inlet must remain unstarted in order to test the proposed restart mechanisms effectively. Simulations will determine as to whether the proposed inlet geometry will sustain a recirculation zone after the unstart has occurred.

The second problem addressed is application of the inlet restarting mechanism explored through the use of simulations. An experimental model is also to be tested in the TUSQ hypersonic wind tunnel in the started operation mode to verify numerical results. The restart method must be practical in real operation such that it doesn't induce any undesirable effects which may include additional oblique swept shock waves in the inlet shock geometry or high localised heating due to sharp geometry changes.

1.3 Dissertation Outline

The dissertation is organised as follows:

- **Chapter 2** addresses theory essential to the research including hypersonic theory and hypersonic inlet design parameters.
- **Chapter 3** reviews current unstart prevention methods and restart mechanisms for hypersonic inlets, identifying gaps within the literature.
- **Chapter 4** outlines the analytical design process of the 2D hypersonic inlet along with estimates of required injection pressures.
- **Chapter 5** describes the numerical methodology used along with description of simulation meshing, boundary and flow conditions.
- **Chapter 6** examines and discusses numerical results.
- **Chapter 7** describes the experimental methodology including the experimental facilities, model configurations and set up of instrumentation.
- **Chapter 8** outlines experimental results.
- **Chapter 9** compares analytical, numerical and experimental results.
- **Chapter 10** draws final conclusions on the work and suggests areas of further investigation.

Chapter 2

Background

Contents

2.1	Scramjet Overview	8
2.2	Hypersonic Fundamentals	15
2.3	Shock Reflections	20
2.4	Shock Interactions	20
2.5	Viscous Interactions	21
2.6	Schlieren flow visualisation	28

A review is presented in this chapter on background information essential to the project. The chapter begin by describing the operation of a scramjet, followed by parameters dictating scramjet inlet design. Relevant hypersonic flow theory is then outlined addressing hypersonic phenomena present in scramjet inlet operation.

2.1 Scramjet Overview

2.1.1 Scramjet Operation

To best describe the scramjet engine, the definition of the ramjet is first required. Ramjet engines have no internal moving parts, reliant upon incoming air being compressed or ‘rammed’ when entering the combustor (Heiser et al. 1994). Referring to Figure 2.1, compression of the air occurs due to a series of shock waves produced in the inlet that the air must pass through when entering the combustor, slowing air to subsonic speeds (Curran & Murthy 2001). Fuel is injected into the high temperature air causing combustion and the air now at elevated temperatures is then accelerated out through a converging-diverging nozzle to a higher velocity than the incoming air, producing thrust (Curran & Murthy 2001). When the velocity exceeds Mach 5, it becomes unreasonable to slow the air velocity to subsonic conditions within the combustor. Scramjet inlets utilise an internal geometry that ensures shock waves induced in the inlet do not slow fluid velocity to subsonic conditions but are still able to compress air substantially. This results in reduced shock losses relative to ramjets with total pressure loss in the compression process minimised. Optimal inlet operation occurs when air capture is maximised, compressing it to desired combustion conditions whilst generating as little drag and total pressure loss as possible. Fuel is injected and combusted at supersonic speed, accelerated out the supersonic nozzle producing thrust. Figure 2.2 represents geometry of a standard scramjet with a three shock inlet configuration.

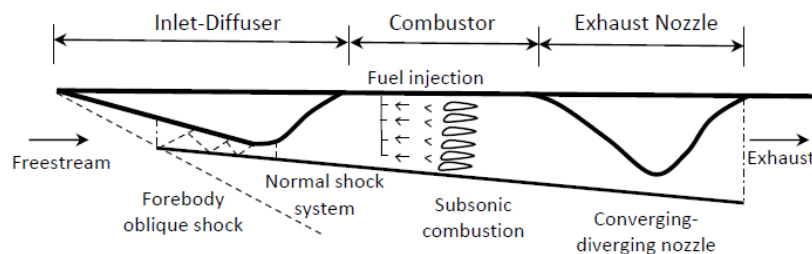


Figure 2.1: Two dimensional schematic of a ramjet engine (Geerts & Yu 2016)

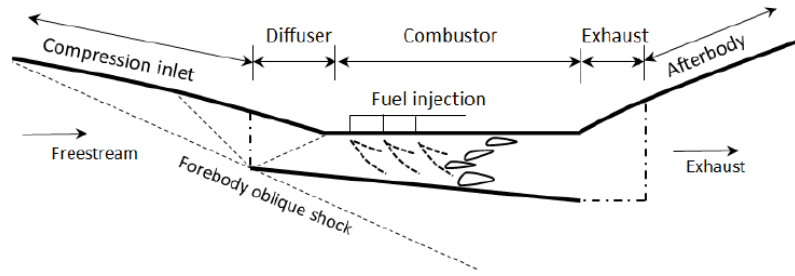


Figure 2.2: Two dimensional schematic of a scramjet engine (Geerts & Yu 2016)

2.1.2 The Inlet

A representative configuration of the scramjet inlet is as seen in Figure 2.2, using two external shock waves and one internal shock wave with two compression ramps. However, multiple other inlet configurations exist as outlined by Mahoney (1990).

The ideal operational state of a scramjet inlet is referred to as the Shock-On-Lip condition (SOL). The compression ramp shocks converge on the cowl lip and the reflected shock impinges on the upper boundary of the inlet. As shock angles vary with flight Mach number, the SOL condition cannot be established at lower or higher Mach numbers than designed as illustrated in Figure 2.3. Mach numbers higher than the designed value will envelop a shock within the inlet and combustor resulting in generation of multiple reflected shocks possibly leading to an unstart. Lower than designed Mach numbers lead to a portion of compressed air missing the inlet (referred to as spillage) decreasing the air capture mass (Shneider, Macheret & Miles 2004).

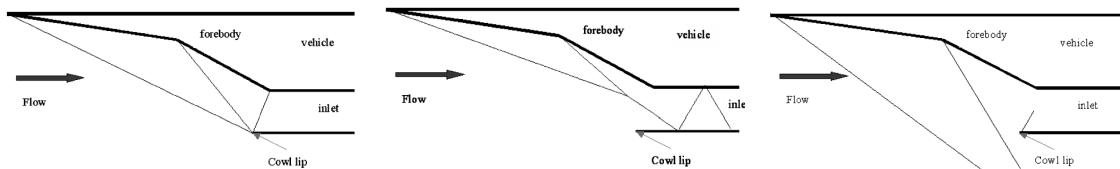


Figure 2.3: Flow and shock geometry of an inlet at (left) the designed Mach number; (centre) higher than designed Mach number; and (right) lower than designed Mach number (Shneider et al. 2004)

2.1.3 Inlet Starting

To ensure good start-ability of hypersonic inlets, the contraction ratio must not exceed a certain limit. The Kantrowitz limit (Equation 2.1) estimates the maximum contraction ratio A_2/A_4 beyond which the intake will not start. The equation assumes a normal shock to be placed at the cowl lip, station 2 referring to Figure 2.4, with the flow choked at the throat, internally contracting from station 2 to the throat located at station 4 (Curran & Murthy 2001). If the internal contraction begins at a different location, the Mach number at that point would be used rather than M_2 .

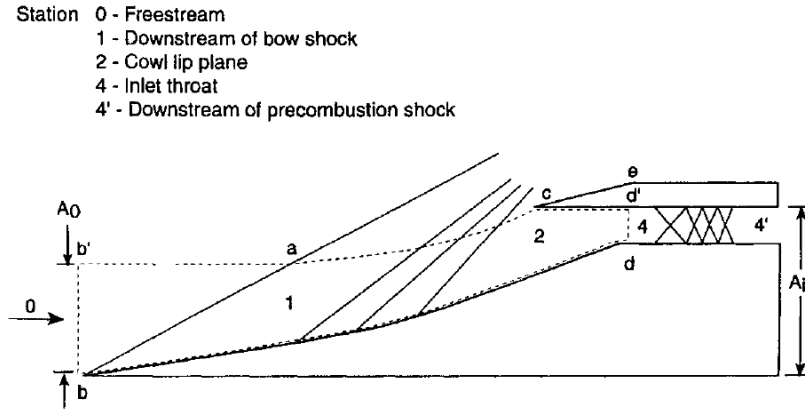


Figure 2.4: Scramjet inlet station definitions (Curran & Murthy 2001)

$$\left[\frac{A_2}{A_4} \right]_{Kantrowitz} = \frac{1}{M_2} \left[\frac{(\gamma + 1) M_2^2}{(\gamma + 1) M_2^2 + 2} \right]^{\frac{\gamma}{\gamma+1}} \left[\frac{(\gamma + 1)}{2\gamma M_2^2 - \gamma + 1} \right]^{\frac{1}{\gamma-1}} \left[\frac{1 + \gamma - 0.5 M_2^2}{\gamma + 0.5} \right]^{-\frac{\gamma+1}{2(\gamma-1)}} \quad (2.1)$$

$$\left[\frac{A_4}{A_0} \right]_{Isentropic} = M_0 \left[\frac{\gamma + 1}{2} \right]^{-\frac{\gamma+1}{2(\gamma-1)}} \left[1 + \frac{(\gamma - 1)}{2} M_0^2 \right]^{-\frac{\gamma+1}{2(\gamma-1)}} \quad (2.2)$$

However, research conducted by Moelder & Szpiro (1966) and Wie & Molder (1992) shows that the Kantrowitz criterion is overly pessimistic and intakes can indeed start at

higher contraction ratios. The maximum contraction theoretically occurs at the *isentropic* or isentropic limit (Equation 2.2) with steady inlet operation below or even close to this limit being impossible (Curran & Murthy 2001). A summary of published results is presented in Figure 2.5 for both inlet starting and maximum contraction ratios for hypersonic inlets. Note that in this figure the inverse of the contraction ratios presented as in Equation 2.1 and 2.2 is being plotted

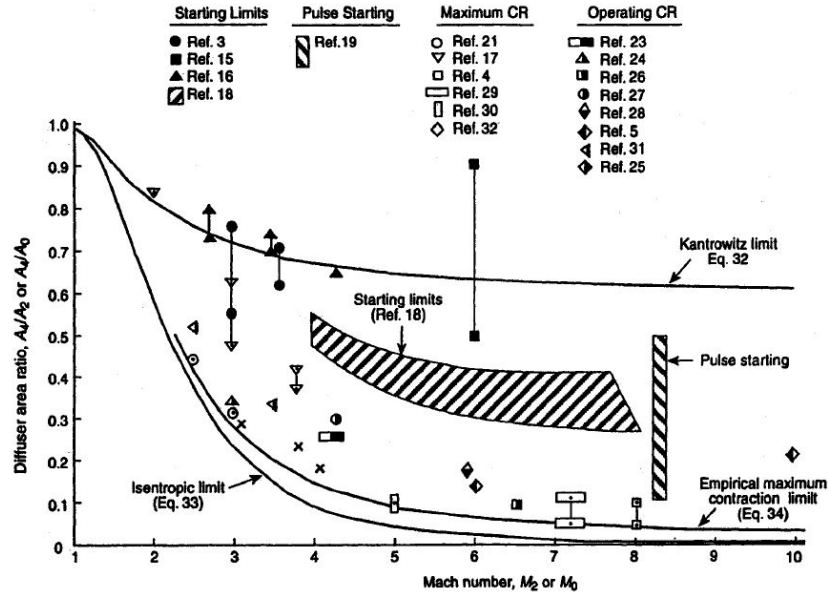


Figure 2.5: Starting and maximum contraction ratio limits (Curran & Murthy 2001)

2.1.4 The Isolator

Following compression from the inlet, the isolator provides further pre-combustion compression. The isolator is a duct connecting the inlet to the combustor, containing a series of shock waves known as a shock train. Geerts & Yu (2016) state that shock train formation can be due to upstream mixed compression inlet causing multiple swbli's imposing an adverse pressure gradient on the internal isolator boundary layer. However, the primary formation is induced due to combustion creating large back pressures causing downstream boundary layer separation in the isolator with the separations causing a series of shock-waves (Geerts & Yu 2016). Heiser et al. (1994) note that the primarily shock structure in the shock train is determined by the incoming Mach number with shock structures placed

in two major types: a single normal shock, and shock trains consisting of bifurcated normal or oblique shocks.

Depending on the Mach number magnitude, the single normal family of shock trains is generally divided into three categories (Matsuo 2003) as illustrated in Figure 2.6. At Mach numbers lower than 1.2, the swbli is weak with no noticeable separation and a relatively straight normal shock. With slightly higher Mach numbers ($1.2 < M < 1.3$), swbli becomes slightly stronger with minimal separation occurring and a curved shock forming. Increasing Mach number again ($1.3 < M < 1.5$), bifurcation of the normal shock occurs with extensive boundary layer separation and curvature of the normal shock. The formation of multiple shock structures to form a shock train takes place at isolator inflows of Mach number 1.5 shown in Figure 2.7.

As Mach number increases further, bifurcation of the normal shock becomes so pronounced such that the pure normal length is confined to the centre region of the flow field. At Mach numbers exceeding 2.0, a family of interacting oblique shock waves is observed running left to right illustrated in Figure 2.8. Static wall pressure rise within the normal shock train is far more abrupt compared to oblique shock trains with a majority of pressure rise associated with the normal shock feature. Referring to Figures 2.6 through 2.8, the length over which wall static pressure rise occurs is labelled L . The pressure rise of the oblique shock train is more gradual with expansion regions (dashed lines) downstream of compression regions (solid lines).

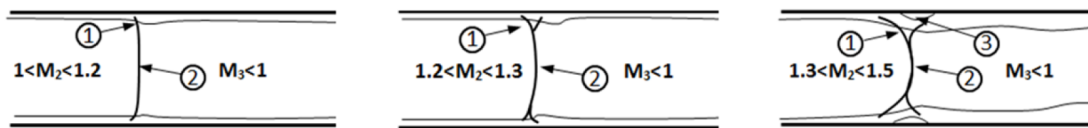


Figure 2.6: Single normal shock forming in a constant area duct (flow is left to right) (Matsuo 2003)

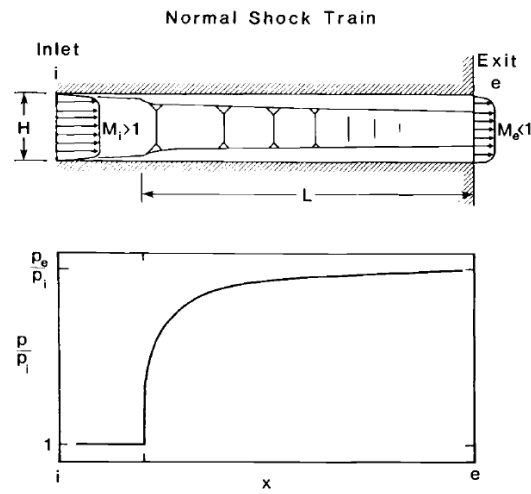


Figure 2.7: Flow pattern and static wall pressure distribution of a complete normal shock train (Anderson 1989)

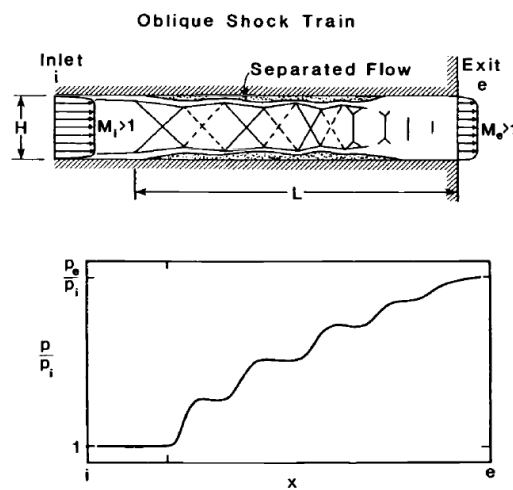


Figure 2.8: Flow pattern and static wall pressure distribution of a complete oblique shock train (Anderson 1989)

2.1.5 Inlet/Isolator Unstart

Disturbances in the isolator originating either from inlet compression effects or large combustion pressure gradients are potential causes of inlet unstart (Heiser et al. 1994). In the case of a scramjet, heat addition to supersonic flow can lead to a pressure rise to a value that cannot be matched by this shock system leading to what is known as thermal choking which forms an upstream propagating unstart shock system (Curran, Heiser & Pratt 1996), (Chang, Li, Xu, Bao & Yu 2017). Increased pressure also results in growth of the separation region at the inlet throat and an increased ramp boundary layer displacement thickness. This has the potential to cause the flow downstream of the inlet to become subsonic and outwards displacement of the leading edge shock wave resulting in spillage of flow over the inlet further contributing to the unstart. Tan, Li, Wen & Zhang (2011) found that due to shock train growth upstream from a high isolator pressure induced using air injection, pressure within the isolator began to rise. This resulted in separation region and boundary layer displacement growth at the inlet throat, eventually reaching a size causing the inlet to unstart. Flow imaging from their investigation is reproduced in Figure 2.9.

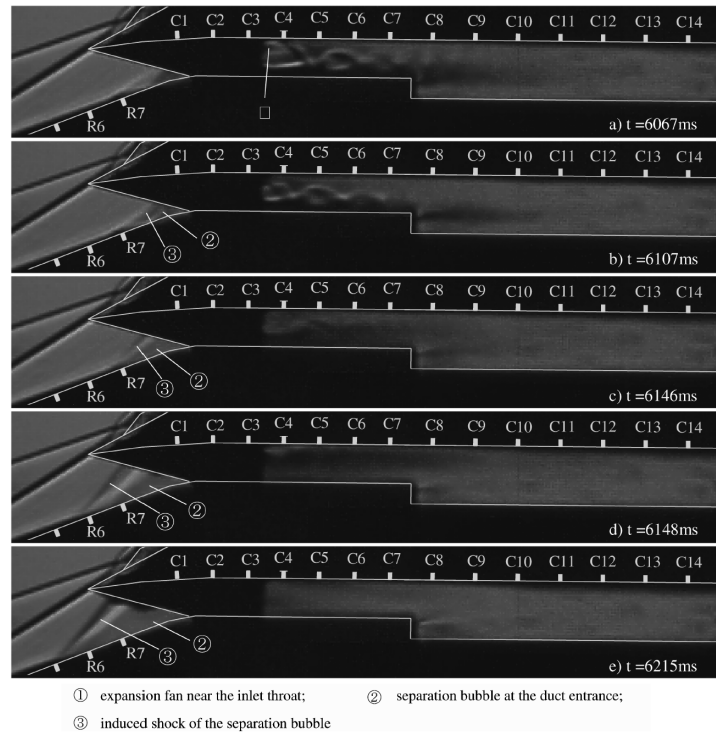


Figure 2.9: Unstart due to separation bubble at inlet throat (Tan et al. 2011)

2.2 Hypersonic Fundamentals

To better understand the operation of a scramjet, fundamental supersonic compressible flow theory must be reviewed. A flow is supersonic when the speed exceeds Mach 1 (the speed of sound). Hypersonic flow occurs when flow speed equals or exceeds speeds of Mach 5 is a generally accepted definition in literature (Pritchard 2010). In the supersonic regime, shock waves begin to envelope over the test object due to the compression of incoming gas. Air that passes through these shock waves experiences an increase in pressure, temperature and density along with a decrease in velocity (Pritchard 2010). Anderson (1989) notes unlike the transition from subsonic to supersonic flow, the supersonic to hypersonic transition does not experience a rapid change in fluid properties. Rather, hypersonic flow is regarded as the regime where specific flow phenomena becomes progressively more important to consider. Primarily, design considerations with increasing Mach number, the compressibility effects across the shock wave become progressively larger (Anderson 1989).

Mach number is defined as the ratio of flow velocity to the local speed of sound i.e. $M = V/a$ where V (m/s) is velocity and a (m/s) is local speed of sound in the fluid and thus the Mach Number is a dimensionless number (Pritchard 2010). The speed of sound a is a function of temperature and defined as

$$a = \sqrt{\gamma RT} \quad (2.3)$$

where γ is the ratio of specific heats, R (J/kgK) is the gas constant and T (K) is fluid temperature (Pritchard 2010). Thus, Mach number varies depending on fluid velocity and temperature.

Anderson (1990) explains that to visualise the formation of oblique shock waves, a small point emitting a circular expanding sound wave is envisioned moving through a stationary gas. When the particle is moving at subsonic speed, ($M < 1$), sound is emitted in all directions at the local speed of sound with the sound wave fronts closer in the direction of travel as illustrated in Figure 2.10. When the speed of the particle enters the supersonic realm, these circular sound waves begin to overlap with the particle constantly outside the family of circular sound waves as $V > a$. The disturbance envelop generated by the waves is referred to as a *Mach wave* formed tangent to the circular sound wave fronts as seen in Figure 2.11 (Anderson 1990). The interior angle of the Mach wave is referred to as the *Mach angle* and can be calculated using geometry (Anderson 1990).

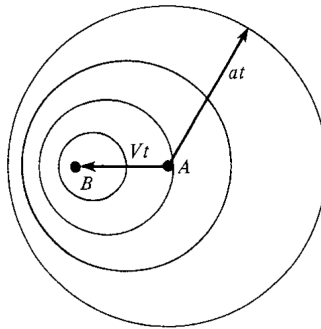


Figure 2.10: Subsonic particle emitting sound wave (Schmidt 2015)

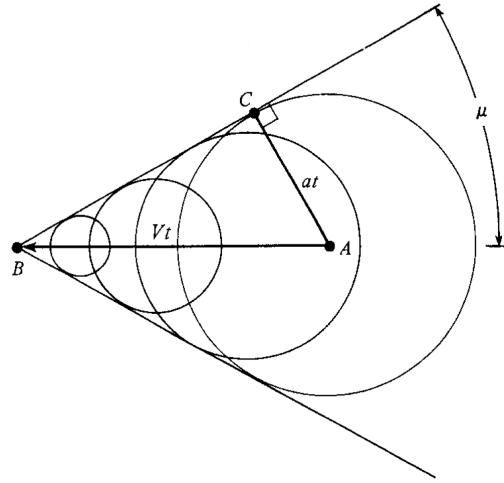


Figure 2.11: Supersonic particle emitting sound waves depicting Mach cone (Schmidt 2015)

$$\sin \mu = \frac{at}{V_t} = \frac{a}{V} = \frac{1}{M} \quad (2.4)$$

If the fluid disturbance is of finite strength, formation of an oblique shock occurs at an angle β to the free stream whereby $\beta > \mu$ as illustrated in Figure 2.12.

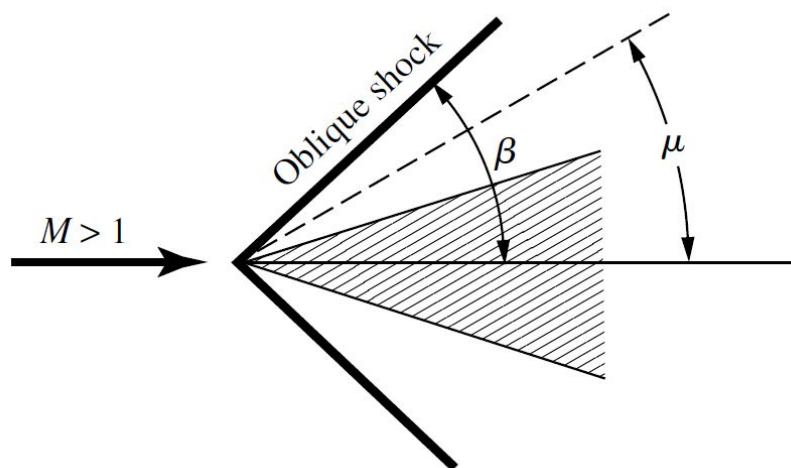


Figure 2.12: Comparison between Mach wave angle and Oblique wave angle (Anderson 2010)

To determine the changes in density, temperature, pressure and Mach number across an oblique shock wave, Conservation of Momentum, Conservation of Energy and the Continuity equation can be used to develop a series of equations shown as Equations 2.5 through to Equation 2.11 as reported by Anderson (1989). Figure 2.13 illustrates the notation for the tangential and normal velocity components, β indicates the shock angle and θ indicates the flow deflection angle. Note that tangential velocity is unaffected by the oblique shock wave.

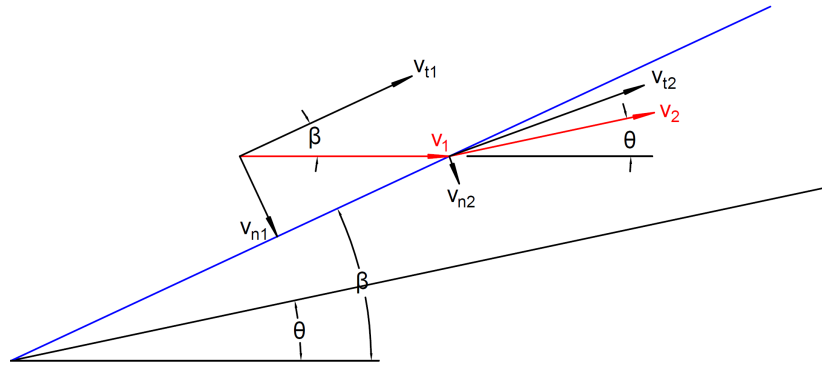


Figure 2.13: Notation of velocity, shock angle and flow deflection angle for flow through an oblique shock wave

The ratio of outlet density to inlet density, inversely equal to the ratio of inlet normal velocity to outlet normal velocity is

$$\frac{\rho_2}{\rho_1} = \frac{v_{n1}}{v_{n2}} = \frac{(\gamma + 1)M_{n1}^2}{2 + (\gamma - 1)M_{n1}^2} \quad (2.5)$$

The ratio of outlet pressure to inlet pressure is

$$\frac{p_2}{p_1} = \frac{2\gamma M_{n1}^2 - \gamma + 1}{\gamma + 1} \quad (2.6)$$

The ratio of outlet temperature to inlet temperature is

$$\frac{T_2}{T_1} = \frac{(2\gamma M_{n1}^2 - \gamma + 1)((\gamma - 1)M_{n1}^2 + 2)}{(\gamma + 1)^2 M_{n1}^2} \quad (2.7)$$

The normal Mach number is

$$M_{n2} = \left(\frac{1 + \frac{\gamma-1}{2} M_{n1}^2}{\gamma M_{n1}^2 - \frac{\gamma-1}{2}} \right)^{0.5} \quad (2.8)$$

The relationship of shock angle to deflection angle is

$$\frac{\tan \beta}{\tan \beta - \theta} = \frac{(\gamma + 1) M_{n1}^2 \sin^2 \beta}{2 + (\gamma - 1) M_{n1}^2 \sin^2 \beta} \quad (2.9)$$

The expressions for Normal Mach Number components prior and post to the shock wave are

$$M_{n1} = M_1 \sin \beta \quad (2.10)$$

$$M_{n2} = M_2 \sin (\beta - \theta) \quad (2.11)$$

To determine the oblique shock angle, the solutions reported by Rudd & Lewis (1998) can be used as presented in Equations 2.12 to Equation 2.16.

$$\tan \beta = \frac{b + 9a \tan \mu}{2(1 - 3ab)} - \frac{d(27a^2 \tan \mu + 9ab - 2)}{6a(1 - 3ab)} \times \tan \left[\frac{n}{3}\pi + \frac{1}{3} \arctan \frac{1}{d} \right] \quad (2.12)$$

where n can be 0,1,-1 corresponding to the weak shock solution, strong shock solution, and a physically meaningless solution, respectively, μ being the Mach wave angle for the pre-shock flow and

$$a = \left(\frac{\gamma - 1}{2} + \frac{\gamma + 1}{2} \tan^2 \mu \right) \tan \theta \quad (2.13)$$

$$b = \left(\frac{\gamma + 1}{2} + \frac{\gamma + 3}{2} \tan^2 \mu \right) \tan \theta \quad (2.14)$$

$$c = \tan^2 \mu \quad (2.15)$$

$$d = \sqrt{\frac{4(1 - 3ab)^3}{(27a^2c + 9ab - 2)^2}} - 1 \quad (2.16)$$

2.3 Shock Reflections

Shock reflections occur when an externally generated shock wave impinges on a surface (Anderson 2010). Referring to Figure 2.14, flow in region 2 behind the incident shock is inclined upwards at the angle θ . Flow in region 2 moving parallel to the ramp impinges on the top wall, turning downward at angle θ . This turn results in the formation of a second shock referred to as the *reflected shock wave*. The strength of this shock wave will be weaker than the impinging shock as the Mach number in region 2 is less than that in region 1 thus its reflection angle is less than that of the impinging shock wave.

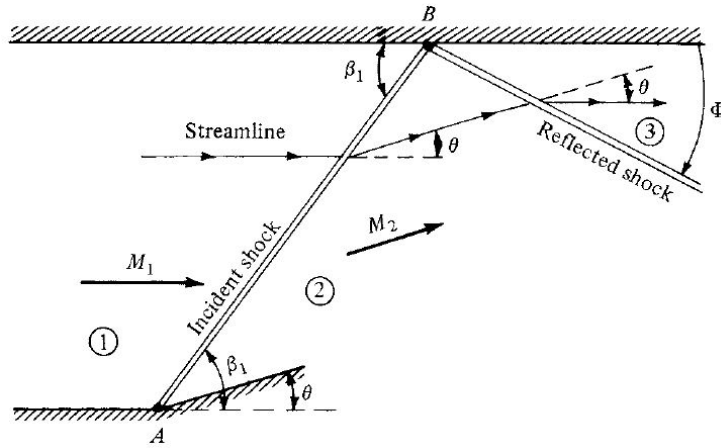


Figure 2.14: Solid reflection of a shock wave from a solid boundary (Anderson 2010)

2.4 Shock Interactions

Shock interactions occurs when two shock waves intersect causing a change in their shock angles and two common configurations are shown in Figure 2.15 (Anderson 2010). The

first interaction type is illustrated in Figure 2.15a. Flow downstream of shock D is denoted as region 4 and past shock C as region 4' with the two regions separated by a slip line EF. The direction of the slip line indicates the common direction of flow downstream of the two shock waves. The second interaction type illustrated in Figure 2.15b. At the point of intersection the two shocks merge and propagate as a stronger shock. A reflected wave is also generated as necessary to adjust the flow such that flow in regions 4 and 5 is in a common direction.

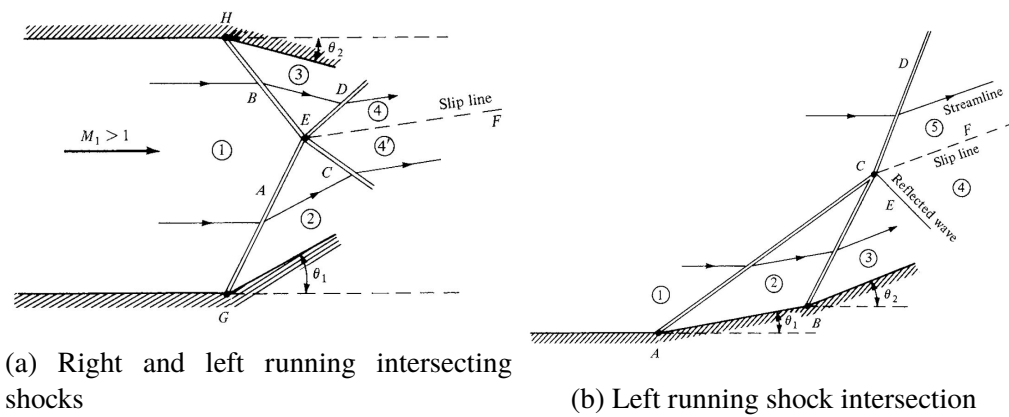


Figure 2.15: Types of shock interaction (Anderson 2010)

2.5 Viscous Interactions

Due to the action of viscosity, the flow will stagnate completely at the surfaces of the vehicle. Anderson (1989) notes that for flow over a flat plate, a boundary layer will develop on the plate's leading edge in a structured laminar form. After a certain running length, the laminar structure becomes distorted and chaotic in character, termed as turbulent.

At hypersonic conditions, high-speed boundary layers typically produce fluid properties of very low density and high viscosity resulting in the boundary layer obtaining high temperature and displacement thickness. Due to viscous interaction between the viscous boundary layer and outer inviscid flow, high rates of heat transfer are transmitted into the inlet walls. This phenomena is known as *viscous dissipation*. The high velocity gas particles within the inviscid flow dissipate some of their kinetic energy to the

slower moving particles into the slower moving boundary layer, transforming into heat energy resulting in a consequent temperature rise. A typical temperature profile within a hypersonic boundary layer can be seen in Figure 2.16.

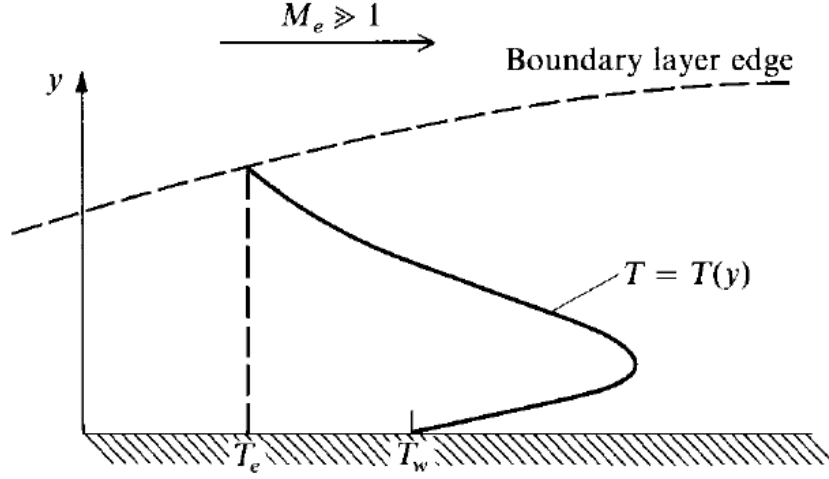


Figure 2.16: Temperature profile in a hypersonic boundary layer (Anderson 1989)

The boundary layer has a certain displacement thickness, resulting in cross-sectional area of a scramjet inlet flow to become reduced. Anderson (1989) gives the a derivation of laminar boundary layer thickness δ as

$$\frac{\delta}{x} \propto \frac{M_e^2}{\sqrt{Re}} \quad (2.17)$$

The expression shows that laminar boundary layer thickness will grow proportionally to the square of the Mach number, thus hypersonic boundary layers will have thickness far larger than low speed boundary layers of the same Reynolds number. This increased boundary layer thickness displaces the outer inviscid flow resulting in outwards displacement of shock waves that may exist above the boundary layer formation region.

Due to compressibility effects in hypersonic flows, the analytical determination of boundary layer thickness becomes substantially more difficult. Compressible boundary layers

are considerably thicker than the incompressible layer due to the high temperature and low density near the wall imposed by the no slip condition. Cantwell (1996) summarises derivations developed by Howarth and Stewartson in the 1940's based on transformations that can be used to map laminar compressible boundary layers to the incompressible form. The derivations use known solutions of the Blasius boundary layer, a similarity solution which describes the steady two-dimensional laminar boundary layer that forms on a semi-finite plate. It assumes that the the boundary layer edge lies within fluid which is slowed to 99 percent free-stream velocity. Derivations produced define a stream function for a virtual incompressible flow that carries the same mass flow, integrated to the wall, as the real compressible flow as illustrated in Figure 2.17.

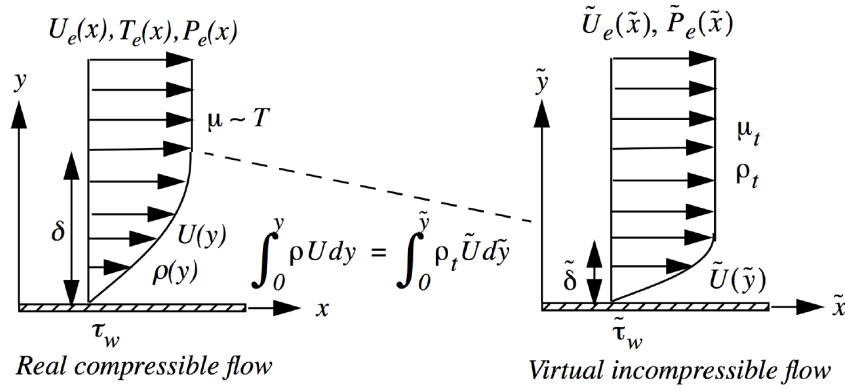


Figure 2.17: Mapping of a compressible boundary layer to an incompressible boundary layer flow (Cantwell 1996)

Derivations allow spatial similarity variables in real and virtual flow to be calculated at any point in the boundary layer where $Pr = 1$ and $\gamma = 1.4$ as

$$\alpha = \tilde{\alpha} + \left(\frac{\gamma - 1}{2} \right) M_e^2 \int_0^{\tilde{\alpha}} \left(1 - \left(\frac{\tilde{U}}{\tilde{U}_e} \right)^2 \right) d\tilde{\alpha}' \quad (2.18)$$

Using derivations outlined by Cantwell (1996) for the Blasius solution for incompressible boundary layers, the similarity variable at an incompressible boundary layer edge is obtained using Figure 2.18.

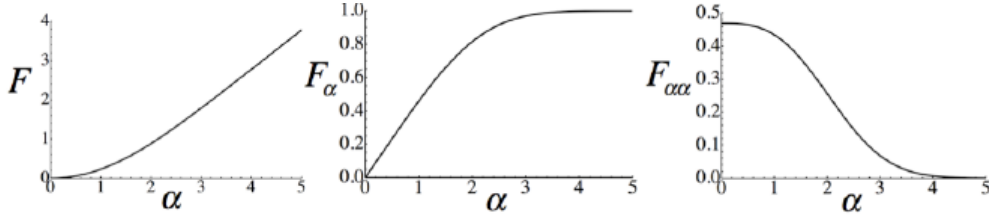


Figure 2.18: Solution of the Blasius equation for the stream function velocity and stress profile in a zero pressure gradient boundary layer (note $F_\alpha = U/U_e$) (Cantwell 1996)

Referring to Figure 2.18, Cantwell (1996) notes that at the edge of the boundary layer ($F_\alpha = U/U_e = 0.99$), the incompressible boundary layer spatial similarity variable is at $\alpha_e = \tilde{\alpha} = 3.469$. The velocity term as in Equation 2.18 is then found as

$$\int_0^{\tilde{\alpha}} \left(1 - \left(\frac{\tilde{U}}{\tilde{U}_e} \right)^2 \right) d\tilde{\alpha}' = 1.67912 \quad (2.19)$$

Using these values, the spatial similarity variable for a compressible boundary can found using the free stream Mach number as

$$\alpha = \tilde{\alpha} + \left(\frac{\gamma - 1}{2} \right) M_e^2 \int_0^{\tilde{\alpha}} \left(1 - \left(\frac{\tilde{U}}{\tilde{U}_e} \right)^2 \right) d\tilde{\alpha}' = 3.469 + 1.67912 \left(\frac{\gamma - 1}{2} \right) M_e^2 \quad (2.20)$$

The boundary layer thickness at a specific location x along the plate is obtained with the equation

$$\delta = \frac{\alpha}{\sqrt{\frac{\rho_e U_e}{2\mu_e x}}} \quad (2.21)$$

Knowing the $\alpha(\tilde{\alpha})$ value, the temperature and density within the boundary layer is able to be found with the equation

$$\frac{T(\alpha(\tilde{\alpha}))}{T_e} = \frac{\rho_e}{\rho(\alpha(\tilde{\alpha}))} = 1 + \left(\frac{\gamma - 1}{2} \right) M_e^2 \left(1 - \left(\frac{\tilde{U}(\tilde{\alpha})}{\tilde{U}_e} \right)^2 \right) \quad (2.22)$$

Numerical solutions relating the velocity and temperature profile at several different Mach numbers are shown in Figure 2.19.

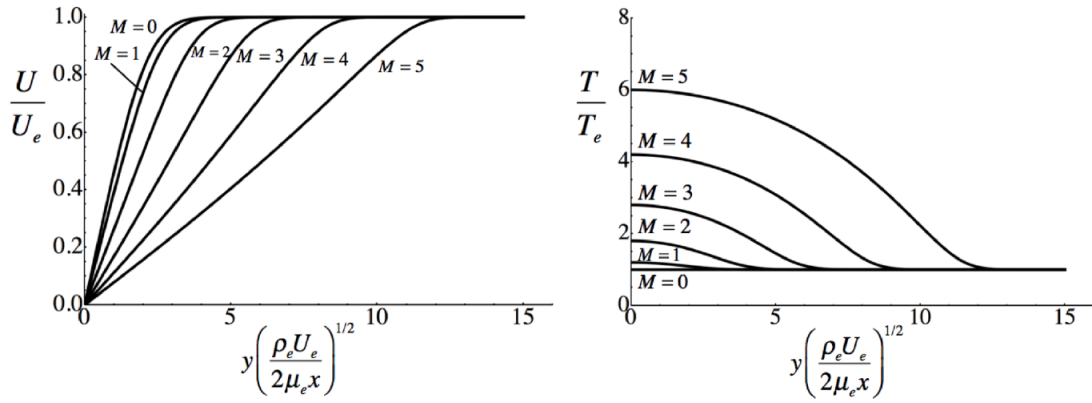


Figure 2.19: Compressible boundary layer profiles for an adiabatic plate at various Mach numbers (Cantwell 1996)

2.5.1 Hypersonic Shock Wave/Boundary Layer Interactions

With thick boundary layers produced in hypersonic conditions, external effects changing boundary layer characteristics have a greater effect on hypersonic engine performance. Most notable of these effects is Shock Wave/Boundary Layer Interactions (swbli's) which occur on both external and internal hypersonic inlet surfaces due to intense adverse pressure gradients imposed by impinging shock waves (incident shock) on the boundary layer. Sandham (2011) notes there are three general configurations in which swbli's occur: shock impingement, ramp flow, and transonic flow over a bump as seen in Figure 2.20. Shock impingement occurs when an object (for example a wedge) placed in a supersonic free stream generates a shock that impinges on the boundary layer. This results in boundary layer thickening, with higher shock strengths inducing boundary layer separation from the surface. The ramp flow model generates the interaction due to a change in wall geometry producing a shock wave as the flow is turned. Larger changes

in geometry will result in separation. These two cases are very similar and the separation is controlled by the overall pressure rise. The third case of transonic flow over a bump occurs in subsonic flows accelerated to supersonic speed which is not of concern for this research.

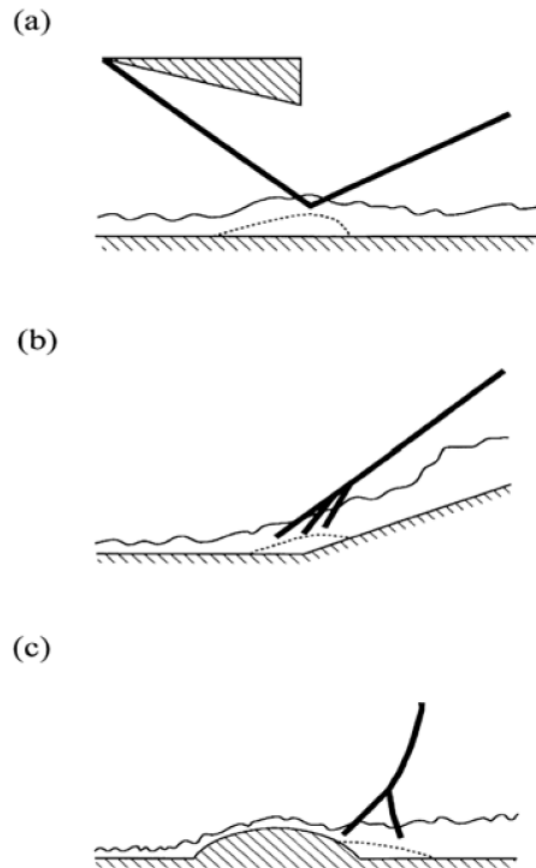


Figure 2.20: Shock wave/boundary layer interaction examples: a) shock impingement, b) ramp flow, and c) transonic flow over a bump (Sandham 2011)

Referring to the shock impingement case on a flat plate in the simplified two-dimensional flow case (i.e. homogeneous in the span wise direction), the detailed flow structure at the reflection can be further explained with reference to Figure 2.20. The externally generated impinging shock wave produces a pressure rise that is transmitted upstream in the subsonic region and causes a local boundary-layer thickening, inducing a region of flow separation from the surface referred to as a separation bubble. As the high pressure behind the shock moves upstream through the subsonic portion of the boundary layer, the separation occurs upstream of the impingement point. As the boundary layer is thick,

the separation forms a shock wave upstream of the separation bubble referred to as the separation shock formed from converging compression waves. The separated boundary eventually reattaches on the wetted surface generating a reattachment shock. Between these two generated shock waves, expansion waves are formed where the boundary turns back to the wetted surface. This makes the boundary layer relatively thin inducing a region of high local aerodynamic heating. The separation and reattachment shocks merge further away from the plate to form a reflected shock wave. A simplified description of the swbli is shown in Figure 2.21. The scale and severity of the interaction depends on whether the boundary layer is laminar or turbulent. As laminar boundary layers will separate more readily than turbulent boundary layers, laminar separation will generally lead to severe separation effects (Sandham 2011).

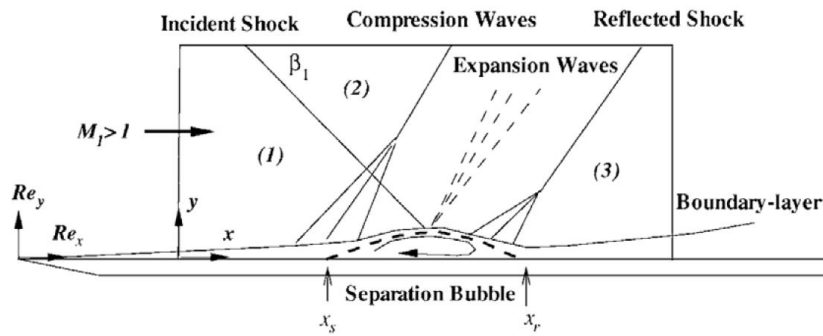


Figure 2.21: Planar shock wave / boundary layer interaction (Anderson 1989)

Anderson (2010) notes that for strong interactions, the shape of the separation may be approximated by a triangle resulting in the formation of a gas dynamic phenomena known as an expansion wave. Unlike oblique shock waves, the pressure, temperature and density continuously decreases across expansion waves and an increase in velocity is observed. Expansion waves occur when a supersonic flow is "turned away from itself" forming in the shape of a fan about the turning radius centre as illustrated in Figure 2.22.

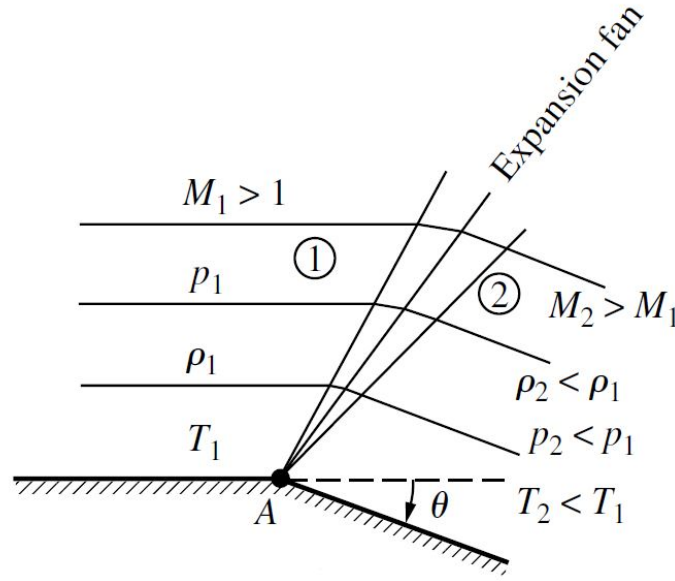


Figure 2.22: Expansion wave formed by a downward turning surface (Anderson 2010)

2.6 Schlieren flow visualisation

Schlieren flow visualisation relies on the concept that light is refracted when passing through a change in fluid density (Schmidt 2015). A typical Schlieren setup is shown in Figure 2.23. Light from a small source is collimated by focusing a mirror or lens and passes through a test field with a varying refractive index. The refractive index $n = c_o/c$ of a medium describes the change in phase speed where c is the speed of light and c_o is the speed of light in a vacuum. The light source must be small to avoid blur in the image. The parallel light is then refocused by a second lens or mirror and imaged by a camera. A knife edge is placed at the focal point of the second lens or mirror, blocking any refracted light to indicate the high density fluid regions one side and low density on the other of the captured image. Figure 2.24 shows a typical oblique shock wave captured with Schlieren flow visualisation.

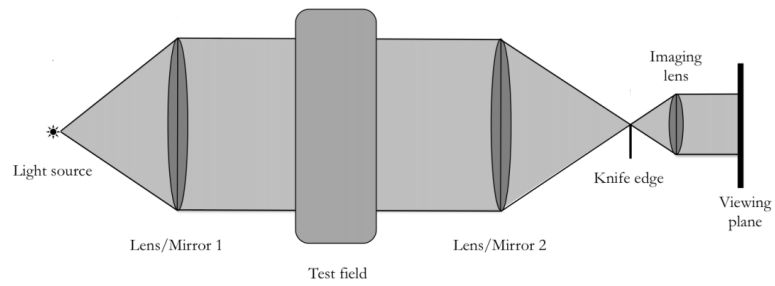


Figure 2.23: Schematic of a typical Schlieren setup (Schmidt 2015)

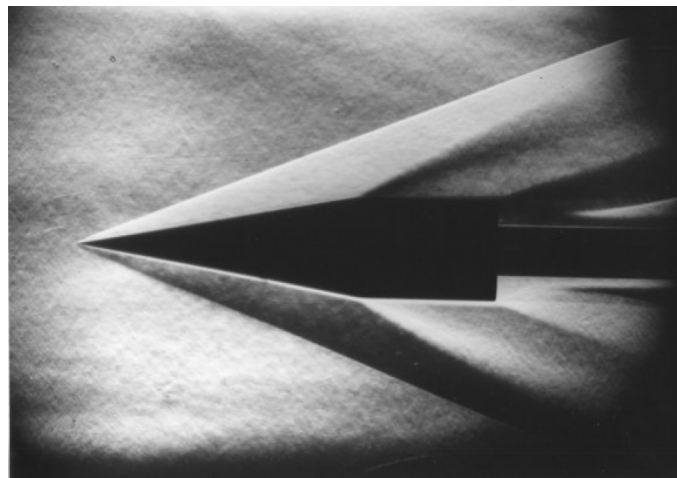


Figure 2.24: Schlieren image of wedge in supersonic flow (Schmidt 2015)

Chapter 3

Literature Review

Contents

3.1	Unstart Control	31
3.2	Restart Control	33
3.3	Literature Gap	35

A review is presented on work in the area of hypersonic inlet unstart prevention and restart mechanisms. The chapter ends by drawing conclusions on gaps observed in the literature and outlining the restart mechanisms to be explored in the presented work.

3.1 Unstart Control

Multiple investigations have been conducted to design devices to prevent unstart. The primary goal of all these devices is that they increase the momentum of the inlet boundary layers such that it better resists the adverse pressure gradient that induces boundary layer separation. The section reviews the different of unstart prevention methods.

Rimlinger, Shih & Chyu (1996) performed numerical investigations into three-dimensional swbli on a flat plate with four staggered rows of bleed holes. The focus of the computations was to examine how bleed through rows of holes affect bleed rate and the pressure and Mach number distributions. Simulations included effects with and without shock impingement and the effects of the hole spacing in streamwise and spanwise directions were also examined. Results showed two rows of bleed holes arranged in a staggered fashion placed upstream of the incident shock are adequate in blocking the shock-induced adverse pressure gradient from propagating further upstream. Results also show that the spacings between the centers of the holes can exceed the hole diameter not just in the streamwise direction, but also in the spanwise direction, and still be able to control shock-induced flow separation.

Flores, Shih, Davis & Willis (1999) numerically analysed a Mach 2.46 boundary layer flow to measure bleeding rates into a plenum through six rows of circular holes at angles of 90° and 20° to the flow arranged in staggered and non-staggered placements. Three cases were tested with case 1 having 90° staggered arrangement, case 2 having 20° staggered arrangement, and case 3 having 90° non-staggered arrangement. Results showed that case 2 produced the highest bleed rate due to the decreased required turning angle. Moreover, the staggered hole arrangement also showed a greater bleed rate compared to the non-staggered arrangement.

Doerffer & Bohning (2003) experimented with the use of both a passive ventilation cavity at the location of the swbli and a suction cavity downstream. Due to the pressure jump

at a shock wave, the ventilation cavity was exposed to a low pressure at the upstream end and a high pressure at the downstream end. This pressure difference induces a flow in the cavity in the direction opposite to the main stream. The experiment was conducted in a Mach 1.3 tunnel generating a normal swbli. Gathering data using Schlieren visualisation and pressure measurements, results showed that use of only ventilation (passive) leads to increased drag due to the generation of a thicker boundary layer. Likewise, use of ventilation and suction (hybrid) results in a thinning of the boundary layer leading to a reduced separation bubble size. However, suction alone results in additional boundary layer thinning compared to the hybrid method, thus further reducing the separation bubble size. The authors conclude that simply using suction at the passive location would be the most effective method of control.

Smith, Babinsky, Fulker & Ashill (2004) performed a similar experiment using air jet vortex generators (AJVG) to generate streamwise vortices to diminish the size of a separation bubble due to a normal swbli across a range of Mach numbers of 1.25, 1.35, 1.45 and 1.55. The AJVG injected upstream of the swbli into the lower portion of the boundary layer where momentum is already low. Taking measurements using Schlieren visualisation and oil surface flow visualisation, results showed that reattachment of the boundary occurred much earlier with the control device.

Conducting both numerical and experimental tests, Jaiman, Loth & Dutton (2004) investigated the effect mesoflap control placed upon normal swbli's. The control system involves placing a mesoflap array beneath the interaction, allowing high-pressure air from the flow downstream of the shock wave to recirculate through a cavity into the low-pressure flow upstream of the wave. The case of a normal shock at a Mach number of 1.4 interacting with the turbulent boundary layer on a flat wall was used with predictions validated with experimental results. Results determined that the onset of upstream flap defections leads to formation of a series of oblique shock waves allowing for deceleration of the flow with relatively small losses in stagnation pressure. Moreover, it was found that the number of flaps and positioning increases pressure recovery, however, deteriorates the condition

of the boundary layer behaviour.

Chang & Fan (2009) studied the effects of boundary layer bleeding on performance parameters of hypersonic inlets, testing a range of different rates of bleeding. Constructing a simulation of a three ramp rectangular scramjet inlet, the bleed mechanism was designed such that the boundary layer thickness was reduced in order to diminish separation region effects induced by high back-pressures. Results showed that this was the case, however, there was a significant reduction in overall mass capture, reducing the inlet's performance.

Souverein & Debiève (2010) experimentally explored the effects of upstream air injection through the means of continuous port air jets at 45 degrees in the transverse direction downstream into a turbulent swbli. The impinging shock was generated using a wedge placed above a flat plate in a Mach 2.3 flow. Taking measurements using Particle Image Velocimetry (PIV) in addition to hot wire anemometry, a reduction of the separation region was observed, however, complete suppression did not occur.

Pasquariello, Grilli, Hickel & Adams (2014) used both numerical and experimental investigations explored the use of a joint air jet and suction mechanism. The mechanism utilised a joint duct embedded in a wall located at a separation region formed from an impinging shock wave to an upstream higher pressure location to create a pressure feedback. The recirculation region was generated using a wedge above a flat plate in a Mach 2.3 flow. Results showed that the suction part of the control was able to reduce the size of the separation region when located at the rear of the separation bubble.

3.2 Restart Control

The following section summarises recent work on hypersonic inlet restarting. Similar to unstart prevention, the main aim of the mechanisms is to add momentum to the unstarted flow to allow the inlet to re-enter a started state.

Through numerical simulation, Yuan & Liang (2006) explored the characteristics of restarting a 2D mixed compression dual ramp scramjet. The unstart was induced by gradually increasing the inflow Mach number into the inlet. As the inflow velocity increased, the inclined backward shock wave in front of the inlet due to the unstart moved into the isolator and the size of the separation bubble gradually became smaller. As the Mach number continued to increase, the inclined unstart shock and separation bubble eventually disappeared and the inlet restarted. The restarting Mach number was far higher than the starting Mach number, however, slightly lower than the inlet design Mach number.

Grainger et al. (2014), through a coupled numerical-experimental investigation, utilised sliding variable doors on a 2D scramjet inlet at Mach 6 to examine inlet starting. A wedge protruding in the rear of the inlet simulated back pressure due to combustion, inducing an unstart. Retraction of the doors at high speed generated a started condition. Results showed that with no back pressure initially, with the door opening mechanism activated, the inlet achieved a started condition. However, at a back pressure induced due to internal wedge protrusion into the inlet, the control mechanism was unable to start the inlet.

Chang et al. (2019) produce numerical simulations to explore the possibility of using heat addition to generate an external shock as a restarting method. Simulating a dual ramp mixed compression scramjet in Mach 5.9 conditions, two cases were explored. The first case exposes the model directly to the Mach 5.9 flow and the second case initially applies a Mach 2 flow then Mach 5.9 to induce an unstart. Results showed once the energy is deposited, a parabolic shock wave is induced by the heated region and then interacts with the separation bubble. The restart performances rely heavily on energy addition parameters. Using energy addition properly, results showed better inlet performance and more importantly enables the inlet restart again, otherwise the large separation bubble still exists. Moreover, the energy addition always increased the mass flow rate, decreasing pressure losses. However, performance was not increased once the scramjet had restarted leading to the conclusion the mechanism should only be operated in the event of an unstart.

3.3 Literature Gap

From the reviewed literature, a great quantity of work investigates mechanisms to prevent unstart occurring. However, some of these mechanisms may not be effective when applied to restart an inlet from an unstart due to the high volume of low momentum fluid of which is required to be removed in order allow the inlet to restart.

Literature reviewed with regards to restart mechanisms primarily rely on numerical simulation with the outcomes of these studies not experimentally verified. Therefore, the actual viability of any of these methods for flow control remains uncertain. Given its relatively positive results in terms of inlet unstart prevention, research which explores the use of air injection or suction at the inlet as a means of inlet restarting is proposed. Application of either slotted air injection or slot suction should be investigated experimentally. But the effectiveness of varying injection locations, pressures and velocities should first be examined to achieve an optimal design of experiments through CFD.

The air injection restart method will aim to add momentum to the large boundary layer formed during the unstart to reduce its thickness. Tests will be conducted by tangentially injecting into the flow. Moreover, investigations could be conducted with injection air at various angles, attempting to increase momentum in the boundary layer and reducing separation. The suction restart method in which the target is removing low momentum boundary layer fluid to reduce its thickness can also be explored. The slotted suction port is to be located at the rear of the swbli at the inlet throat to remove low momentum air at the source of propagation.

Similar to investigations conducted by Tan et al. (2011), it is proposed that a slotted air injection port at the rear of the isolator will be used to induce unstart comparable to thermal choking. Simulations will be conducted to determine the required pressure needed to sustain an unstart even after the injection has been removed.

Chapter 4

Model Design

Contents

4.1	Model Geometry	37
4.2	Ramp boundary layer thickness	40
4.3	Model Scale	41
4.4	Transverse Injection	42

Design of a 2D single ramp dual compression inlet is achieved using analytical approaches. Specifications for the required inlet geometry to achieve the shock-on-lip condition is provided. Calculation of the laminar boundary layer thickness on the inlet ramp is used to estimate the amount of spillage incurred by the inlet. Maximum model size for the TUSQ hypersonic wind tunnel is determined by defining the Mach cone formed by the flow core at the nozzle exit. Estimates are made on the required pressure from the unstart injection to induce enough of a flow blockage in the isolator to cause an unstart.

4.1 Model Geometry

Shock properties over the model scramjet inlet is to be found for the inflow conditions specified in Table 4.1.

Property	Symbol	Value
Mach Number	M_1	5.85
Static Pressure	p_1	740 Pa
Static Temperature	T_1	73 K
Gas Constant	R	287
Ratio of Specific Heats	γ	1.4

Table 4.1: Free stream flow conditions for model inlet design

By testing a range of different ramp angles for geometric compatibility with the test section and nozzle, the adopted ramp angle was 12 degrees. With this value, along with the above conditions in Table 4.1, the shock angle and the post shock flow conditions were determined using Equations 2.5 through 2.16 assuming the weak shock solution ($n = 0$).

First Shock Calculations

The leading shock angle β_1 is calculated

$$\begin{aligned}
 \mu &= \sin\left(\frac{1}{M_\infty}\right) = 2.983 \times 10^{-3} \\
 a &= \left(\frac{\gamma-1}{2} + \frac{\gamma+1}{2} \tan^2 \mu\right) \tan \theta = 0.0425 \\
 b &= \left(\frac{\gamma+1}{2} + \frac{\gamma+3}{2} \tan^2 \mu\right) \tan \theta = 0.2551 \\
 c &= \tan^2 \mu = 2.771 \times 10^{-9} \\
 d &= \sqrt{\frac{4(1-3ab)^3}{(27a^2c+9ab-2)^2}} - 1 = 0.02896 \\
 \beta_1 &= \tan^{-1} \left(\frac{b+9a \tan \mu}{2(1-3ab)} - \frac{d(27a^2 \tan \mu + 9ab - 2)}{6a(1-3ab)} \times \tan \left[\frac{n}{3} \pi + \frac{1}{3} \arctan \frac{1}{d} \right] \right) = 19.77^\circ
 \end{aligned}$$

Using this result, flow parameters downstream of the leading shock are found

$$\begin{aligned}
 M_{n1} &= M_1 \sin \beta = 1.979 \\
 p_2 &= p_1 \left(\frac{2\gamma M_{n1}^2 - \gamma + 1}{\gamma + 1} \right) = 3.2561 \text{ kPa}
 \end{aligned}$$

$$\rho_2 = \rho_1 \left(\frac{(\gamma+1)M_{n1}^2}{2+(\gamma-1)M_{n1}^2} \right) = 0.0931 \text{ kg/m}^3$$

$$T_2 = \frac{P_2}{R \times \rho_2} = 121.92 \text{ K}$$

Second Shock Calculations

Using above flow parameters, the angle of the second shock is found to be

$$\beta_2 = 13.45^\circ$$

and this results in flow parameters downstream of the second shock being

$$M_{n2} = 1.686$$

$$M_3 = 3.349$$

$$p_3 = 10.258 \text{ kPa}$$

$$\rho_3 = 0.202 \text{ kg/m}^3$$

$$T_3 = 176.59 \text{ K}$$

Table 4.2 summarises flow conditions from the foregoing analysis.

Table 4.2: Summary of flow conditions for proposed inlet design

	Pressure (Pa)	Density (kg/m³)	Temperature (K)	Mach No.
<i>Free Stream</i>	740.0	0.0353	73.0	5.85
<i>Downstream Shock 1</i>	3256.1	0.0931	121.9	4.30
<i>Downstream Shock 2</i>	10258	0.2024	176.6	3.35

Using MATLAB, inlet geometry was obtained by finding the intersection point of the two shock wave angles, placing the cowl tip at this point to achieve the SOL condition with a 10 mm isolator height as shown in to Figure 4.1.

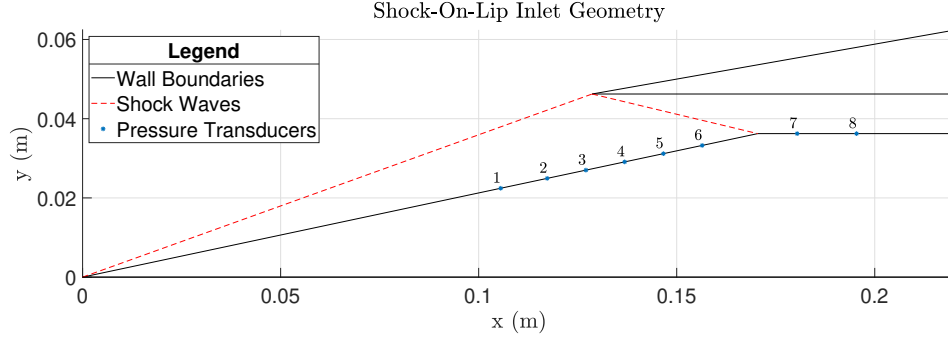


Figure 4.1: Inlet geometry at Mach 5.85 for the SOL condition, numbering indicates pressure transducer locations

To ensure that the inlet would self-start, the contraction ratio (CR) must not be greater than that of the Kantrowitz limit calculated below as

$$\left[\frac{A_2}{A_4} \right]_{Kantrowitz} = \frac{1}{M_2} \left[\frac{(\gamma + 1) M_2^2}{(\gamma + 1) M_2^2 + 2} \right]^{\frac{\gamma}{\gamma+1}} \left[\frac{(\gamma + 1)}{2\gamma M_2^2 - \gamma + 1} \right]^{\frac{1}{\gamma-1}} \left[\frac{1 + \gamma - 0.5 M_2^2}{\gamma + 0.5} \right]^{-\frac{\gamma+1}{2(\gamma-1)}}$$

$$\left[\frac{A_2}{A_4} \right]_{Kantrowitz} = 1.5071$$

At SOL conditions with the specified isolator height a contraction ratio approximately equal to 1.9 is found. Thus, according to the Kantrowitz limit, the inlet will not self start. Referring to Figure 2.5, using a contraction ration of $A_4/A_2 = 0.526$ lies above the isentropic limit along with being inside the designated starting limits. This suggests that the inlet should self-start. Numerical results will further verify the start-ability of the inlet.

4.2 Ramp boundary layer thickness

To estimate the maximum displacement of the leading shock, the boundary layer thickness at the end of the compression ramp is to be calculated. Using the flow properties downstream of the first shock as specified in Table 4.2 and a length of $x = 174.3$ mm corresponding to the ramp length in Figure 4.1, the spatial similarity variable at the boundary layer edge is calculated using Equation 2.20 as

$$\alpha = 3.469 + 1.67912 \left(\frac{1.4 - 1}{2} \right) (4.30)^2 = 9.678$$

Viscosity is calculated using a MATLAB function as found in Appendix E.3 and is found to be $\mu = 8.596 \cdot 10^{-6}$ Pa s. Boundary layer displacement at the end of the ramp is then found using Equation 2.21 as following where $U_e = M_e \sqrt{\gamma R T_e} = 951.588$ m/s as

$$\delta_e = \frac{9.678}{\sqrt{\frac{0.0931 \cdot 951.588}{2 \cdot 8.596 \cdot 10^{-6} \cdot 0.1734}}} \cdot 1000 = 1.78 \text{ mm}$$

Figure 4.2 shows the maximum upward displacement of the leading shock wave due to the boundary layer. Note that this calculation is actually based on the boundary layer thickness rather than the boundary layer displacement thickness so a conservative estimate for the maximum displacement effect will have been achieved.

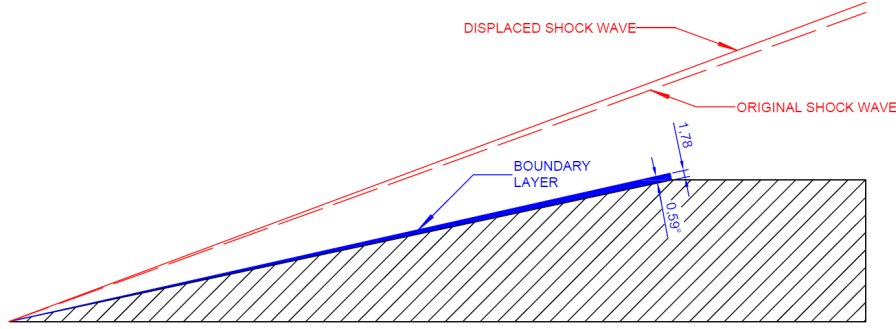


Figure 4.2: Displacement of leading shock wave on inlet compression ramp due to boundary layer formation

Seen above, the boundary layer causes minimal deflection of the leading shock wave. However, it should be noted that due to the formation of a swbli at the inlet throat there will be some growth in boundary layer thickness causing additional spillage over the cowl. Simulations will determine the severity of this additional boundary layer growth to establish if modifications to model geometry are required.

4.3 Model Scale

Due to the core flow diameter of the Mach 6 nozzle in the TUSQ Hypersonic Wind Tunnel, limitations are placed on the size of the model. The flow has an effective diameter of 160 mm at the exit of the nozzle, and this dimension can be used to specify the Mach cone downstream of the nozzle exit. Within this Mach cone region, the flow properties should be reasonably uniform and thus, the model should fit within this region. Using Equation 2.4, we find the Mach cone forms the angle

$$\mu = \arcsin\left(\frac{1}{M_\infty}\right) = \arcsin\left(\frac{1}{5.85}\right) = 9.84^\circ$$

Figure 4.3 shows the available testing flow space with the proposed model location. The model here is placed whereby the ramp tip is 5 mm from the nozzle exit with the centre of the isolator located along the centre-line of the nozzle flow. This allows for shifting of

the model forwards or backwards within the test section as needed.

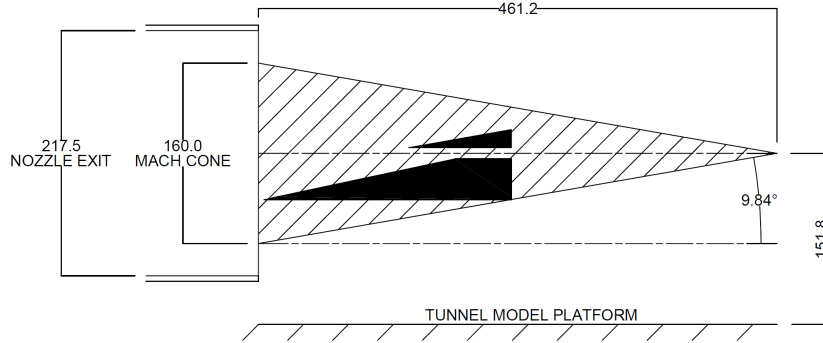


Figure 4.3: Mach cone formed by the TUSQ Mach 6 nozzle with proposed model location

4.4 Transverse Injection

In order to unstart the inlet, a transverse injection downstream in the isolator is to be implemented. In most experimental cases, testing regimes are defined through a ratio of injection to free stream momentum flux, known as the momentum flux ratio, to allow for quantification of cross-flow penetration (Dharavath, Manna & Chakraborty 2018)

$$\bar{q} = \frac{\rho_{inj} U_{inj}^2}{\rho_{\infty} U_{\infty}^2} = \frac{(\gamma P M^2)_{inj}}{(\gamma P M^2)_{\infty}}$$

Dharavath et al. (2018) explored transverse sonic slot injection primarily aimed for scramjet combustor fuel injection design. They describe that when a transverse flow comes through a slotted nozzle into supersonic flows, it expands causing a blockage due to the formation of a strong bow shock, in front of the injection point causing boundary layer separation. Directly after the injection, the boundary layer reattaches and a recompression shock is formed as illustrated in Figure 4.4.

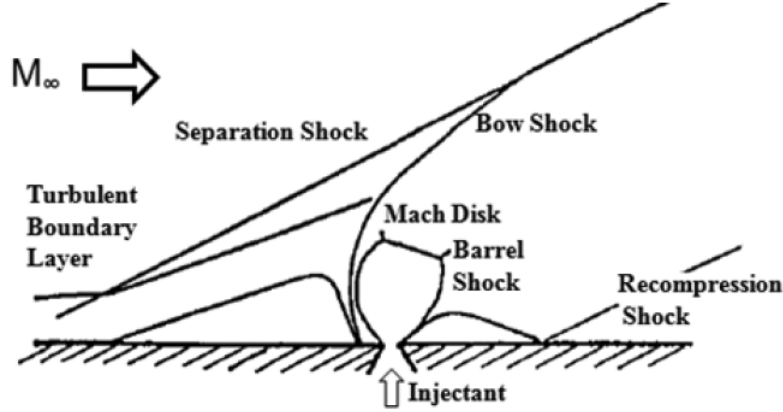


Figure 4.4: Schematic of transverse injection flow field (Dharavath et al. 2018)

Dharavath et al. (2018) conducted both experiments and simulation over a flat plate with varying sonic transverse slot injection widths and injection pressure ratios of $\frac{P_{inj}}{P_\infty} = 17.72, 25.15, 33.64, 43.15$ in an air flow of $M_\infty = 3.75$, $P_\infty = 1.20$ MPa and $T_\infty = 299$ K. Their results showed that as the pressure ratio increased, the interaction between the secondary flow and free stream pressure increased with the upstream separation point moving progressively upstream. Upstream separation distance X_{upsep} and penetration height h_{pen} for different pressure ratios are presented in Figure 4.5.

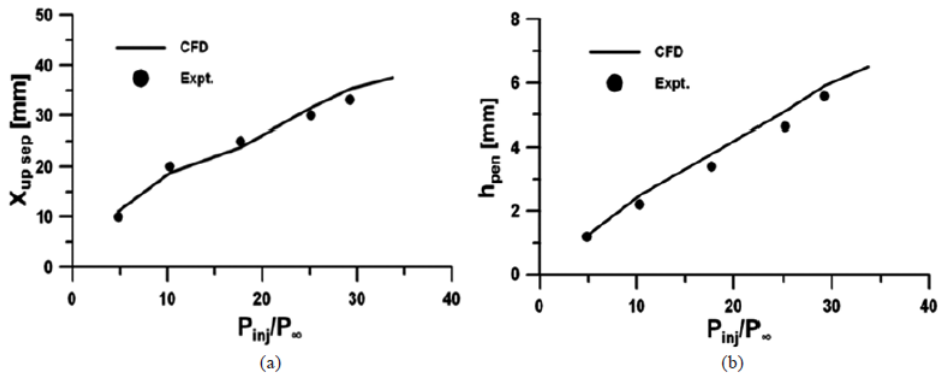


Figure 4.5: Comparison of (a) upstream separation distance and (b) penetration height with experimental data for different pressure ratios (Dharavath et al. 2018)

Simulations with differing slot widths and pressure ratios, gave the penetration results shown in Figure 4.6.

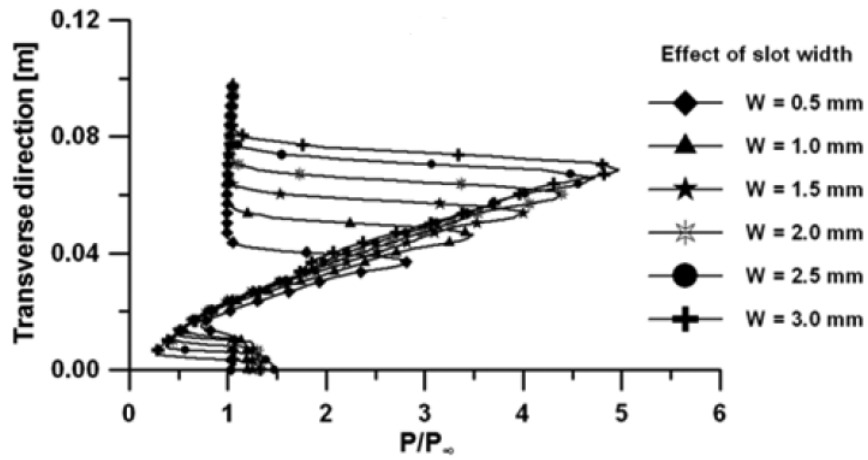


Figure 4.6: Pressure ratio vs transverse direction jet penetration varying with slot widths (Dharavath et al. 2018)

Given the inlet has an isolator height of 10 mm, referring to Figure 4.6, the required pressure ratio is $\frac{P_{inj}}{P_{\infty}} \approx 0.5$ for a 1 mm slot width. Given that $P_{\infty} = 10258.0$ Pa, the minimum injection pressure to cause a significant blockage is $P_{inj} = 5129.0$ Pa. Simulations at various pressures and slot widths will determine the required injector pressure to be used in experimentation.

Chapter 5

Numerical Methodology

Contents

5.1	Numerical Testing Procedures	46
5.2	Eilmer4	46
5.3	Grid Definition	47
5.4	Boundary Condition Definition	49
5.5	Simulation Sequence	50
5.6	Mesh Independence Study	50

This chapter begins by describing the simulations to be run on each restart mechanism, followed by a brief description of the CFD software used. Simulation grid definition, boundary conditions and sequencing of simulations is then addressed. The mesh independence study is then presented to assess simulation accuracy.

5.1 Numerical Testing Procedures

Numerical simulation is used to determine the required injection parameters in the isolator in order to produce a sustained unstart. Investigation then follows to explore the three proposed restart mechanisms:

- **Slot Suction:** Suction of the recirculation region at inlet throat using 200 Pa suction
- **Mid-Ramp Injection:** Injection of sonic air at 100 kPa at angles of 90, 45 and 12 degrees, located 90 mm in the x direction from the ramp tip
- **Tip Injection:** Transverse injection of sonic air at 100 kPa for durations of 100, 250, 500 and 1000 μ s, located 10 mm in the x direction from the ramp tip

Upon completion of the evaluation of simulation results, a final restart mechanism along with required unstart parameters are to be tested experimentally.

5.2 Eilmer4

To develop a computational model of the proposed scramjet inlet, the Eilmer4 solver will be used, developed within the CfH at UQ by Jacobs & Gollan (2016). Eilmer was originally developed as a tool to simulate and aid in design of shock tunnels and expansion tubes. More recently, Eilmer4 is being used in the simulation and design of hypersonic inlets. The code has been in use for a number of years with verification established through multiple experimental campaigns.

The Eilmer4 solver is a finite volume implementation of the compressible Navier Stokes Equations. The solver works by breaking down the flow domain into 2D planar, 2D axis-symmetric or 3D cells and expressing the governing equations in integral form over these cells. The rate of change of conserved quantities (mass, momentum, energy) is set equal to the flux of these quantities across the cell interfaces. The cells calculations are iterated over time to simulate the flow domain. Eilmer4 can model both inviscid and viscous flow, and is able to incorporate various gas models (e.g. ideal, thermally-perfect, equilibrium, multi-temperature conditions) and turbulence models. Construction of models is typically

done using multiple blocks, and either structure and unstructured grids.

The Eilmer4 program is user-controlled through a lua script that defines geometry, species mass fraction, gas models and flow conditions such as velocity, temperature, pressure as well as the boundary conditions of the model. Simulated results obtained were primarily visualised using ParaView.

Initial simulations were run on 4 CPUs in parallel on a personal computer with an Intel CORE i7 processor. However, final simulations requiring more computational resources were run in parallel on multiple cores using USQ's High Performance Computer (HPC) facility.

5.3 Grid Definition

With the geometry of the inlet defined in Figure 4.1, definition of a structured grid using 2D or 3D blocks can be completed with each block containing a finite number of cells. Given the relatively large amounts of computational time required for a 3D grid and the desire to perform multiple optimisation trials, a 2D simulation was chosen. The block geometry was defined by writing a lua script with results as presented in Figure 5.1.

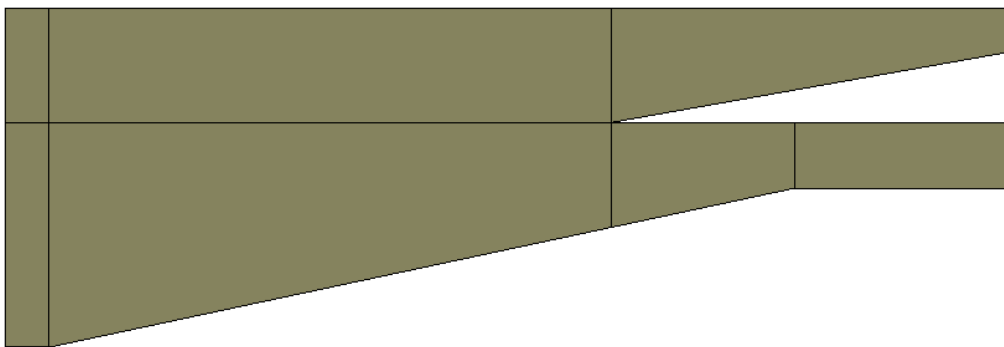


Figure 5.1: Blocking of inlet mesh

Once the initial blocking was constructed, meshing within the blocks was assigned. To effectively simulate boundary layer parameters, cells are required to be clustered towards

the assigned constant temperature (set to 300 K) no-slip walls. Eilmer4 allows for this mesh clustering using a function called *RobertsFunction* which allows for varying magnitudes of clustering towards specified block sides. Implementation of clustering in the mesh can be seen in Figure 5.2. The number of cells in x and y directions in the final simulation was significantly greater than shown, the resolution shown here is for illustration purposes.

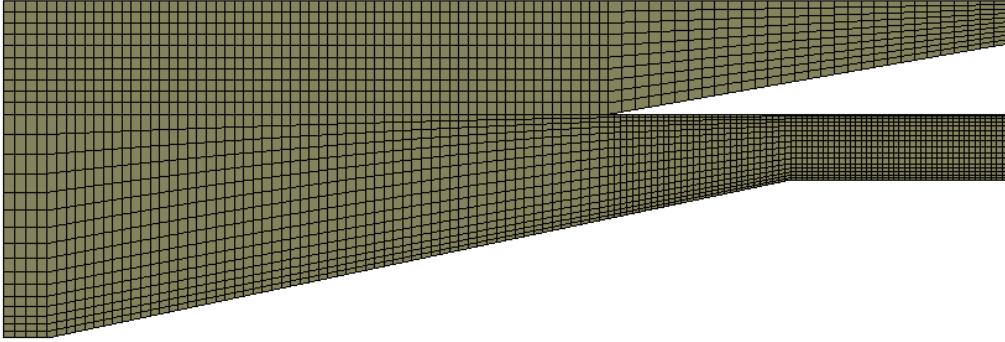


Figure 5.2: Mesh constructed inside inlet blocks with clustering towards constant temperature no-slip walls - illustrative low resolution mesh

To introduce injection and suction ports into the simulation, changes to the grid definition were required. As three restart mechanisms and one unstart injection are required, four separate grids are required to be generated. As both the unstart injection and suction port are both located in the inlet throat, the same blocking can be used for each script. Furthermore, as the tip and mid-ramp injection are located along the ramp, blocking for these scripts is also similar. However meshing will change to relocation of blocking for the different simulations. Table 5.1 outlines the location of the injection/suction ports relative to the ramp tip. Figure 5.3 shows an example of an illustrative low resolution mesh used for the mid-ramp injection.

Table 5.1: Front side location of 1mm wide injection/suction ports located in the x -direction from the ramp tip

	<i>Tip Injection</i>	<i>Mid-Ramp Injection</i>	<i>Throat Suction</i>	<i>Unstart Injection</i>
x (mm)	10.0	90.0	172.0	202.5

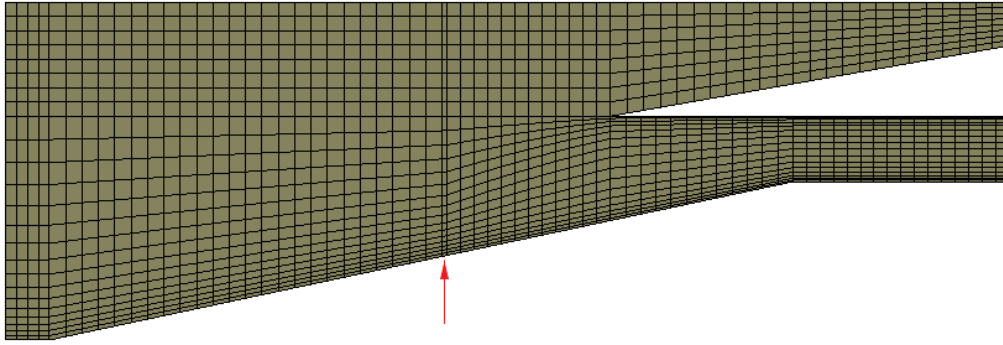
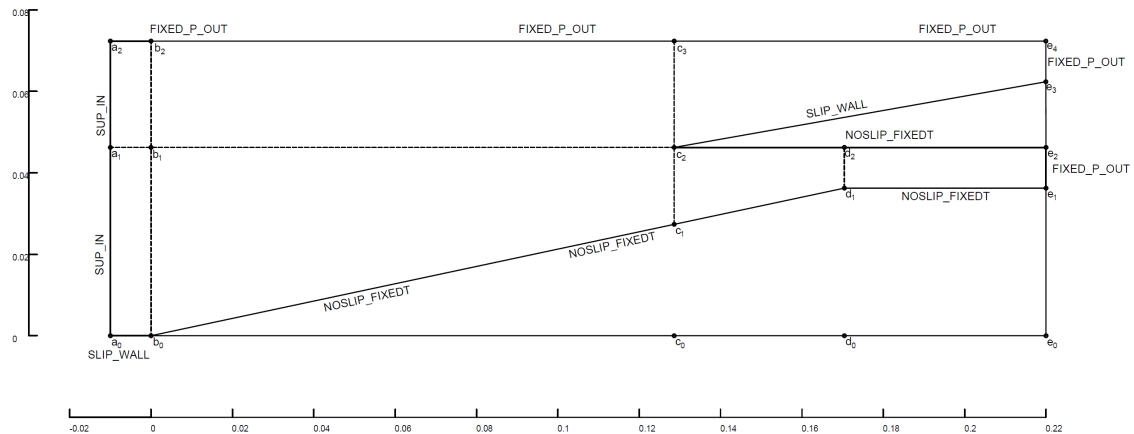


Figure 5.3: Inlet Mesh with mid-ramp injection meshing indicated with the arrow - illustrative low resolution mesh

5.4 Boundary Condition Definition

After blocking, an initial fill condition for the flow domain was specified as a low pressure ideal air, initially at 500 Pa, 300 K with zero velocity. These values were selected as they are reasonably close to values used in the test section in experimental testing.

Referring to Figure 5.4, boundaries of the initial flow domain consist of the single compression ramp (b_o to d_1), isolator walls (d_1 to e_1 and c_2 to e_2) and cowl top wall (c_2 to e_3). Inflow is set from a_o to a_2 , fixed pressure outflow set along a_2 to e_4 to e_3 and e_2 to e_1 and slip wall set from a_o to b_o . Both the compression ramp and the isolator walls were modelled as constant temperature walls at 300 K with no-slip condition with the cowl top wall set to the slip condition. The incoming supersonic flow was modelled as a viscous, laminar flow. Table 4.1 defines the initial inflow conditions used.



5.5 Simulation Sequence

The initial simulation (Start) beings using the initial fill condtion with initial incoming inflow as defined in the above section. After this, each simulation mesh calls upon the preceeding flow solution listed as follows:

1. Start
2. Unstart injection
3. Sustained unstart (same mesh as Start)
4. Restart Mechanism (Tip Injection, Mid-Ramp Injection, or Throat Suction)
5. Restart (same mesh as Start)

5.6 Mesh Independence Study

A mesh independence study was used to find the resolution required for the flow solution to be independent of the mesh resolution. The study involves the comparison of multiple simulations of increasing global grid resolutions. Parameters such as flow exit or flow entry are assessed to define the minimum cell number needed so the flow result doesn't change if the cell count is increased.

For this simulation, data measurements will be taken averaged along the inlet isolator mid-line at ten equally spaced points as illustrated in Figure 5.5. Results of the mesh independence are presented in the following chapter.

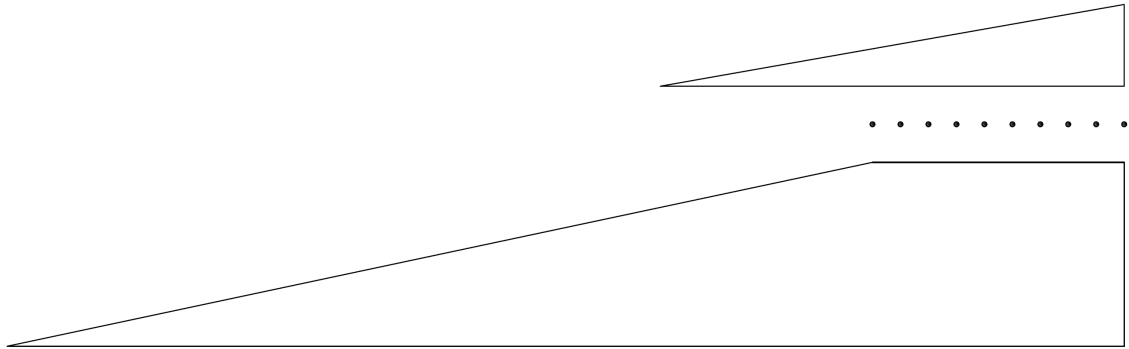


Figure 5.5: Location of averaged pressure data points along isolator midline (indicated by black dot points)

Chapter 6

Numerical Results and Discussion

Contents

6.1	Mesh Independence Study	53
6.2	Self-Started Inlet	54
6.3	Unstart Injection	58
6.4	Unstart Sustainment	60
6.5	Restart Mechanisms	62
6.6	Restart	66
6.7	Evaluation of Restart Mechanisms	71

Results from simulations of the restarting mechanisms are provided. The mesh independence study results are first presented, to define the grid resolution where mesh independence is achieved. Impulsive starting results of the inlet of both inviscid and viscous simulations are presented. Unstart injections are applied to the started inlet isolator to demonstrate the capacity to unstart the intake. Simulation of the unstart injection removal determined if the inlet would remain unstarted. Restart mechanisms are then tested through computational simulation to observe the effect they have on the inlet flow field. The chapter ends by drawing conclusions on the most effective restart mechanism.

6.1 Mesh Independence Study

The following section outlines results describes from the mesh independence study. Figure 6.1 shows the decreasing change in average density at points indicated in Figure 5.5 over a 5 ms flow duration with increasing mesh resolution. Table 6.1 lists the mesh resolution of each simulation and the percentage change between each simulation flow data. Simulations were run with 70 processors per job using 5 nodes and 14 processors per node with a total allocated memory of 100 Gb. Results from the study indicate that sufficient mesh independence is achieved when using a discretization factor of 15.

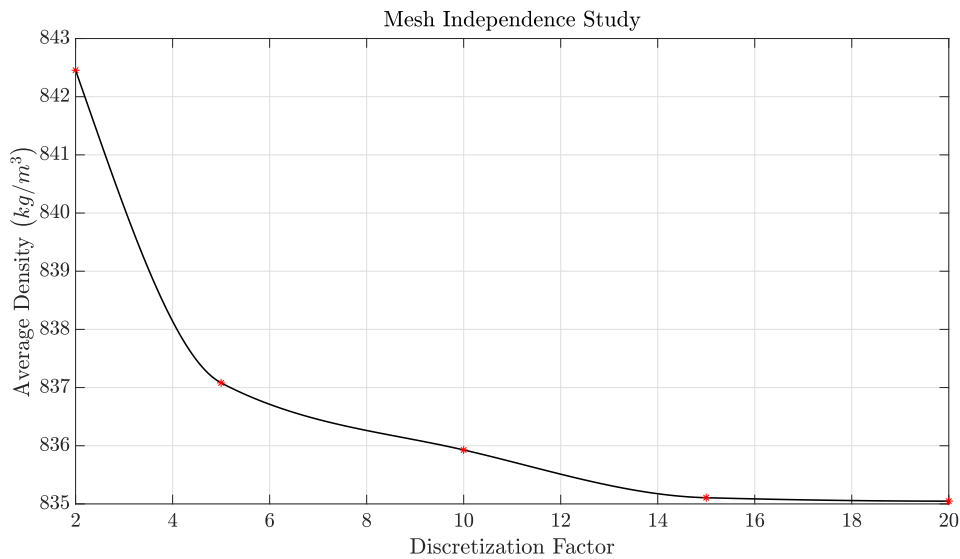


Figure 6.1: Plotted results from mesh independence study

Table 6.1: Tabulated results from mesh independence study

Discretezation Factor	Cell Count	Computational Run Time (seconds)	Percentage Density Difference (%)
2	3084	26.6	-
5	19275	623.0	0.640
10	77100	2151.4	0.138
15	173475	8675.9	0.0983
20	308400	27757.3	0.007

6.2 Self-Started Inlet

To form an inlet simulation with an unstarted flow field, a started inlet simulation must be first established. To match flow conditions similar to that seen in experimental tests, the inlet will undergo impulsive starting which ‘self-starts’ the inlet. Unlike in flight conditions where the air speed gradually increases through the inlet until reaching operational Mach numbers, impulsive starting occurs when high speed air (in this case Mach 6) enters the inlet where the air is initially at zero velocity.

A preliminary inviscid simulation of the inlet was initially conducted as a means of validation for the analytical results. Figure 6.2 shows a pressure contour of the simulation at 5 ms.

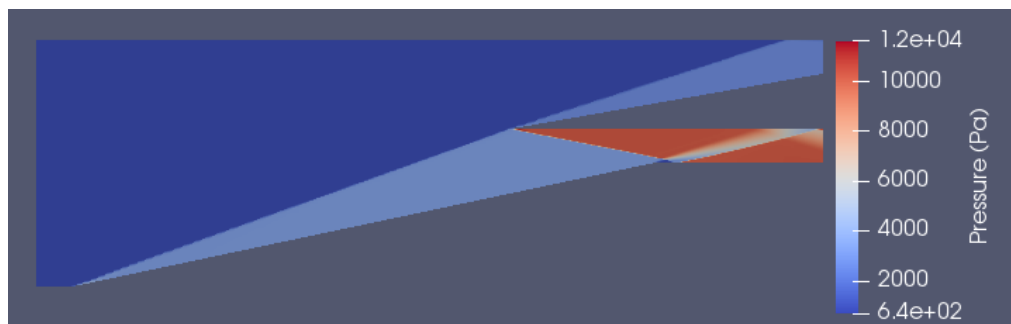


Figure 6.2: Pressure contour of inviscid simulation of inlet at 5 ms reaching steady conditions

As shown in Figure 6.2, the cowl shock does not perfectly impinge at the inlet throat corner. Rather, it impinges inside the isolator resulting in a reflected shock wave generated from the inlet ramp. This error in geometry may have resulted due to rounding error when designing the inlet. Alternatively, the CFD result may have differed due to finite shock thickness effects. Flow data was extracted from the co-ordinates illustrated in Figure 6.3. Referring to Table 6.2, simulated variables near exactly match analytical results.

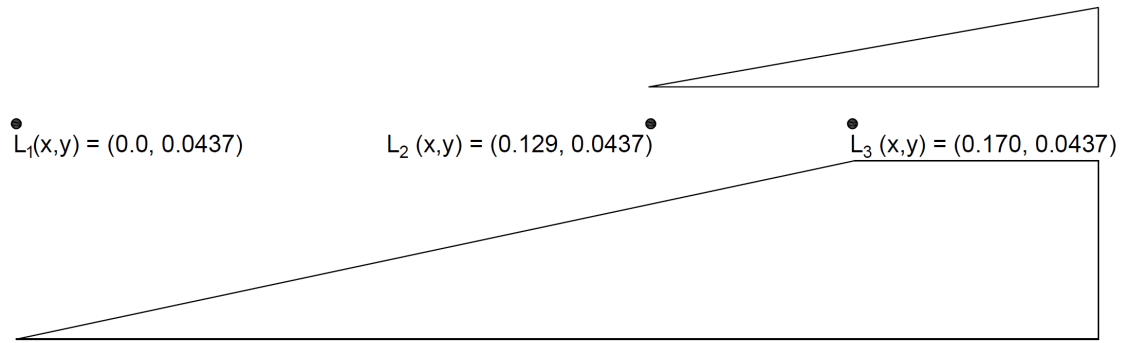


Figure 6.3: Location of inviscid data collection points (indicated by black dot points)

Table 6.2: Simulated vs Analytical inlet flow conditions

	Pressure (Pa)		Density (kg/m ³)		Temperature (K)	
	<i>Simulation</i>	<i>Analytical</i>	<i>Simulation</i>	<i>Analytical</i>	<i>Simulation</i>	<i>Analytical</i>
L_1	740	740	0.0353	0.0353	73.0	73.0
L_2	3255.0	3256.1	0.0930	0.0931	122.0	121.9
L_3	10251.6	10258.0	0.2021	0.2024	176.7	176.6

Applying the constant temperature no-slip boundary condition as outlined in section 5.4 to the simulation configuration, an viscid laminar simulation was produced. Due to adjustments made to the model established from initial experimental testing outlined in Appendix G, the isolator height was raised from 10 mm to 15 mm. Using density gradients on the inlet to view the position of the wave motion in a simulated Schlieren, the startup of the inlet can be seen in Figure 6.4. The leading shock wave is seen to impinge at the cowl tip in the first 330 μ s. A weak shock wave can be seen to be generated for the cowl tip. Reaching 500 μ s, there are no visible signs that any flow blockage occurs. An increase in density is seen at the rear of the isolator from shock wave compression from the reflected leading shock wave and cowl shock wave. This has shown that, at least for this condition, the inlet is likely to start.

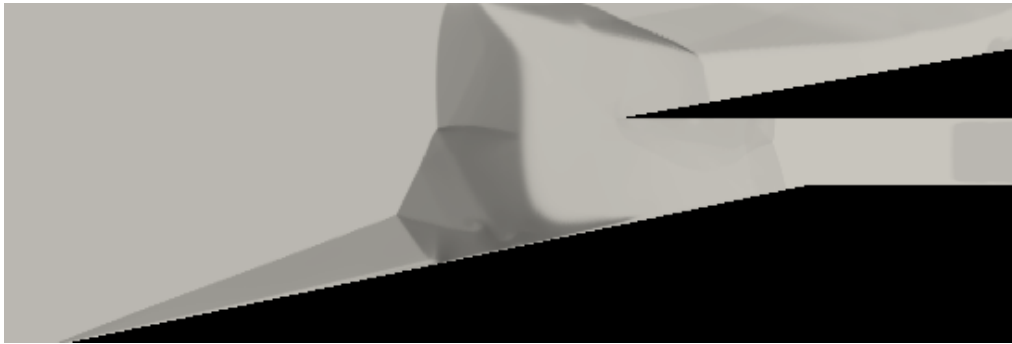
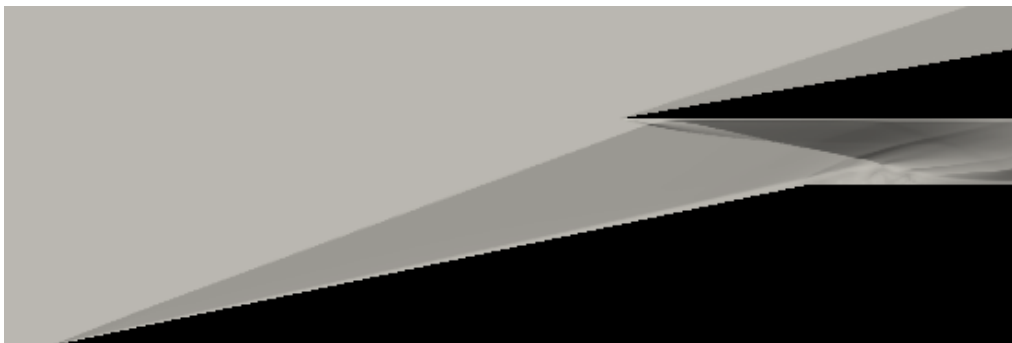
(a) 170 μs (b) 330 μs (c) 500 μs

Figure 6.4: Schlieren of simulation showing impulsive starting of inlet

Running the simulation for 50 ms, pressure variations along the ramp at data locations as indicated in Figure 4.1 at various time increments were obtained to determine when the simulation reached steady conditions as shown in Figure 6.5.

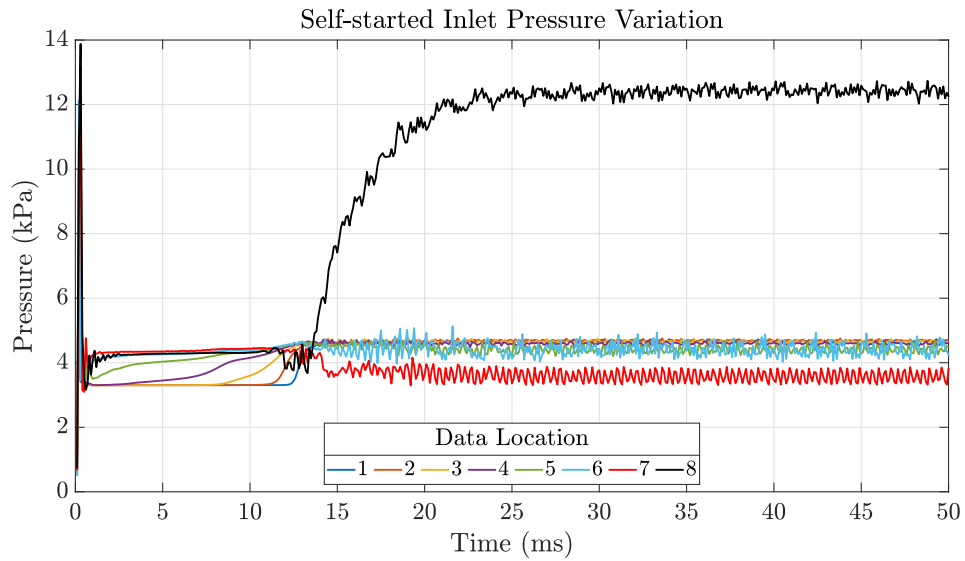
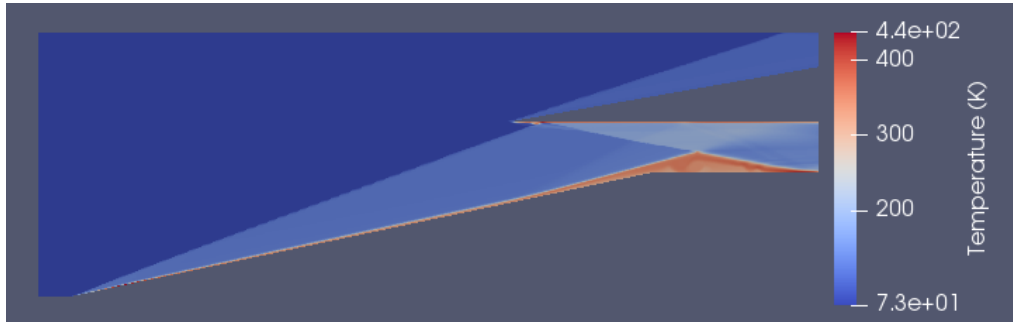
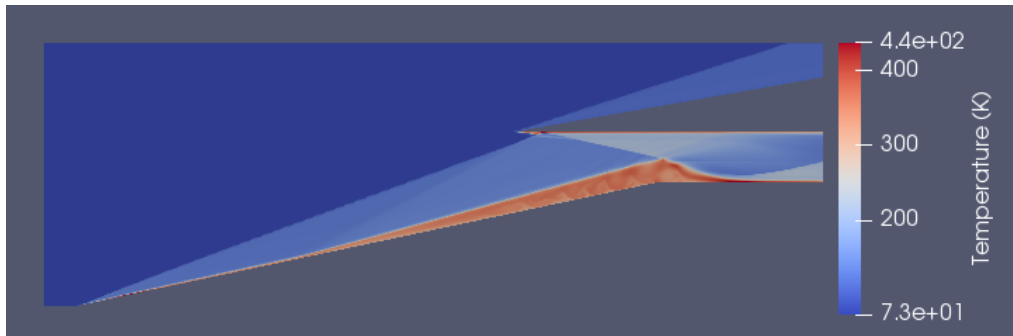


Figure 6.5: Self-started inlet pressure variation over 50 ms flow duration (refer to Figure 4.1 for positions of data locations)

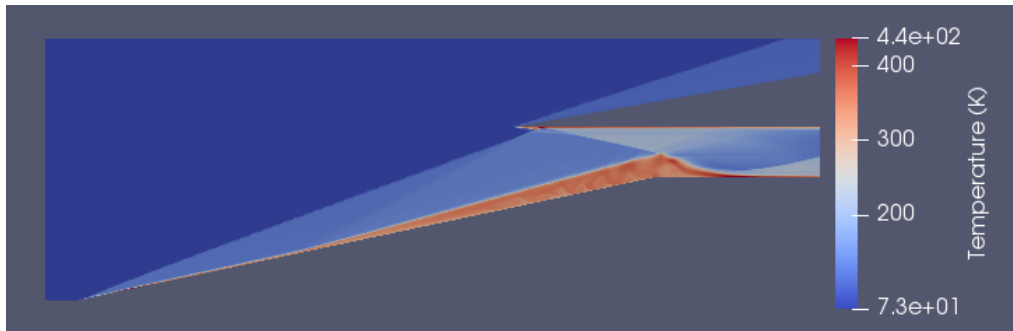
Referring to Figure 6.5, a steady increase in pressure along the ramp up to 10 ms is observed. Then from 13 ms, a high increase at data location 8 is observed, plateauing at approximately 25 ms at which time the inlet reaches steady conditions. Figure 6.6 shows growth of the separation region induced by a swbli from the cowl shock at 10, 20 and 30 ms intervals displaying the inlet reaching steady conditions. As the isolator height was raised to 15 mm, impingement of the leading shock into the upper isolator wall occurs, reflecting downward into the inlet throat contributing to growth of the separation region.



(a) 10 ms



(b) 20 ms



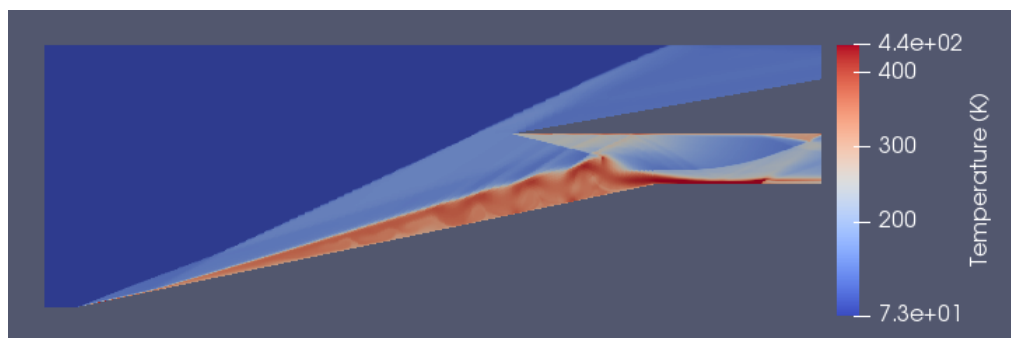
(c) 30 ms

Figure 6.6: Temperature contours of self-started inlet simulation at various times

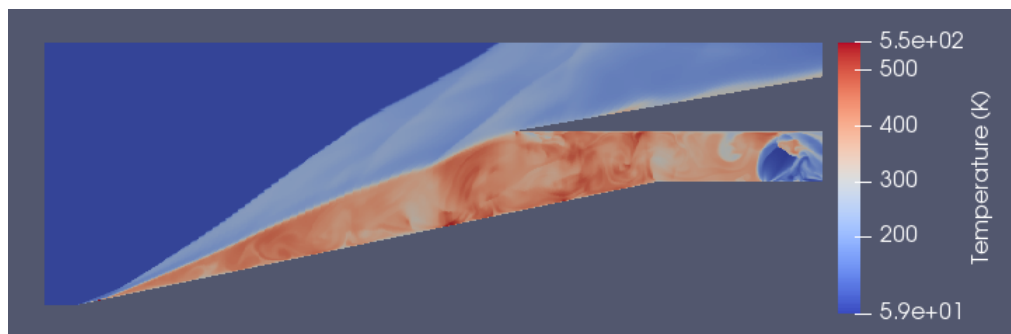
6.3 Unstart Injection

Outlined in Section 4.4, in order to have a penetration distance of approximately 10 mm in a transverse flow with a 1 mm slot width at sonic velocity, a pressure of about 5.1 kPa is required. However, as the isolator height was raised to 15 mm recalculation of this pressure is needed to limit the flow through the isolator. From Figure 4.6, it is seen that the pressure required for the injection will be larger than for the 10 mm penetration. To

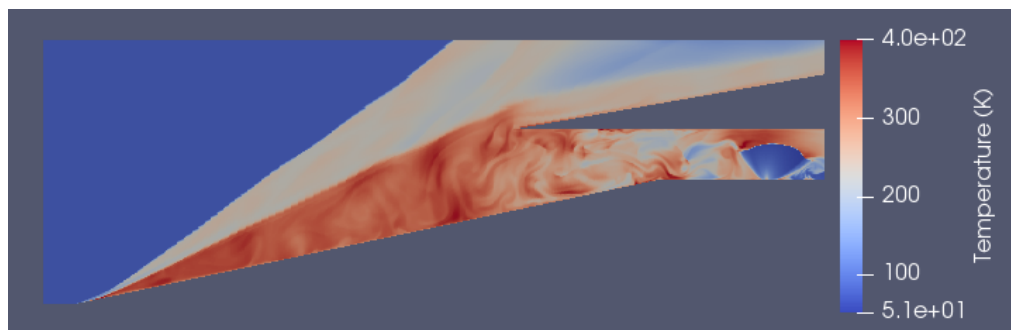
determine a pressure which causes a sufficient blockage to induce unstart, simulations were run with unstart injection pressures of 10 kPa, 50 kPa and 100 kPa. Results shown in Figure 6.7 indicate that injection pressures of 50 kPa and 100 kPa cause sufficient blockage to induce an inlet unstart whereas the 10 kPa injection does not induce a great enough blockage to cause the inlet to unstart. This result suggests that results by Dharavath et al. (2018) should not be used to directly define injection pressures required for inlet unstarting.



(a) 10 kPa



(b) 50 kPa



(c) 100 kPa

Figure 6.7: Temperature contours of the inlet at 5 ms after initiation of unstart injection for various unstart injection pressures

Figure 6.8 shows the variation in pressure that occurs after activation of the unstart injection at locations 1 and 8 for the case of the 100 kPa injection pressure. Location 8 shows an initial pressure spike after approximately 0.4 ms followed by a spike by location 1 at approximately 1.2 ms. This occurs because when the flow blockage is activated, the flow cannot all continue through the existing isolator path, thus causing a building up in pressure initially in the isolator. This pressure rise then translates upstream into the inlet, subsequently causing the pressure spike measured by location 1. As this is occurring, the increased pressure results in growth of the separation region, leading to boundary layer growth causing flow spillage. Once unstarted, the pressure in the inlet drops as flow is redirected over the cowl.

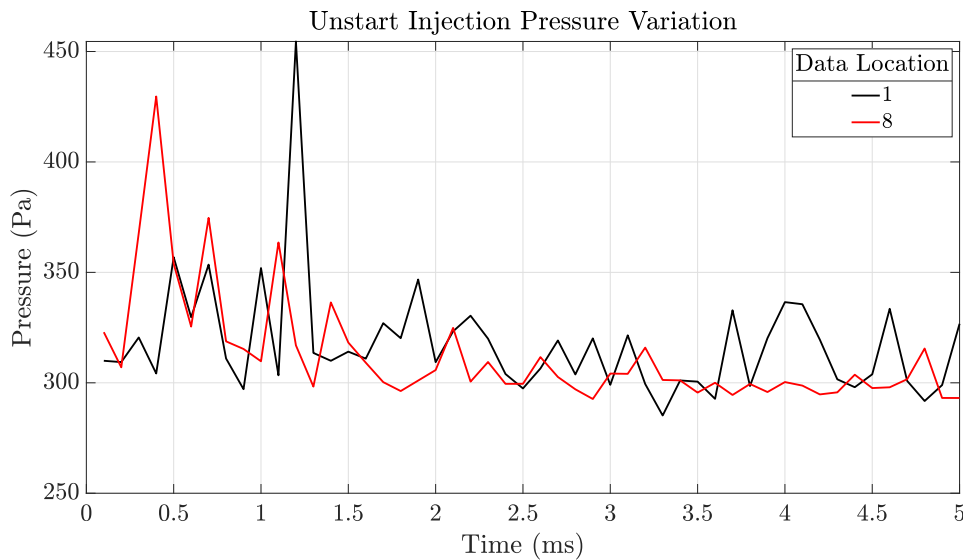
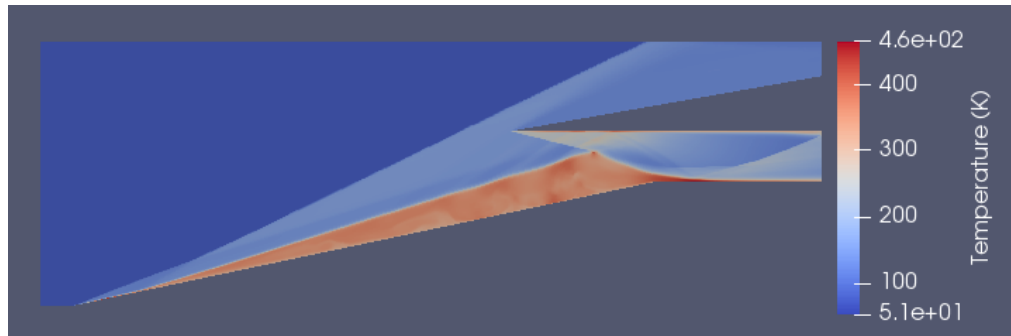


Figure 6.8: Unstart injection pressure variation due to isolator flow blockage at data locations 1 and 8 for the 100 kPa injection pressure (refer to Figure 4.1 for positions of data locations)

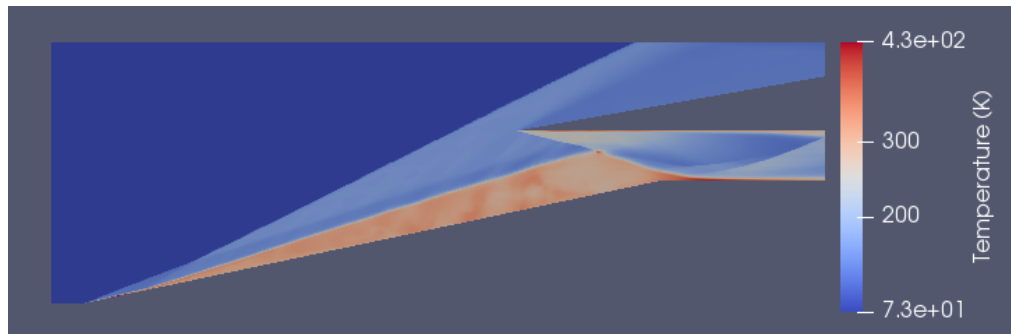
6.4 Unstart Sustainment

For accurate assessment of the restart mechanism effectiveness, the inlet must remain unstarted even after when the unstart blockage is removed. Using flow simulations with 50 kPa and 100 kPa unstart injections, results from the simulations at 5 ms after removal of the unstart injection are shown in Figure 6.9. As illustrated by Figure 6.9, the boundary

layer on the main ramp maintains significant thickness such that severe flow spillage occurs. Furthermore, both 50 kPa and 100 kPa injection cases cause essentially the same stable unstarted flow state.



(a) 50 kPa injection removed



(b) 100 kPa injection removed

Figure 6.9: Temperature contours from two inlet cases at 5 ms after removal of the unstart injection

Figure 6.10 compares the started and sustained-unstarted inlet, showing that compression is reduced at the rear of isolator for the unstarted case. Note that the sustained unstarted case shown in Figure 6.10 is actually from the 100 kPa injection case, but as noted previously, both cases generate essentially the same stable unstarted inlet flow.

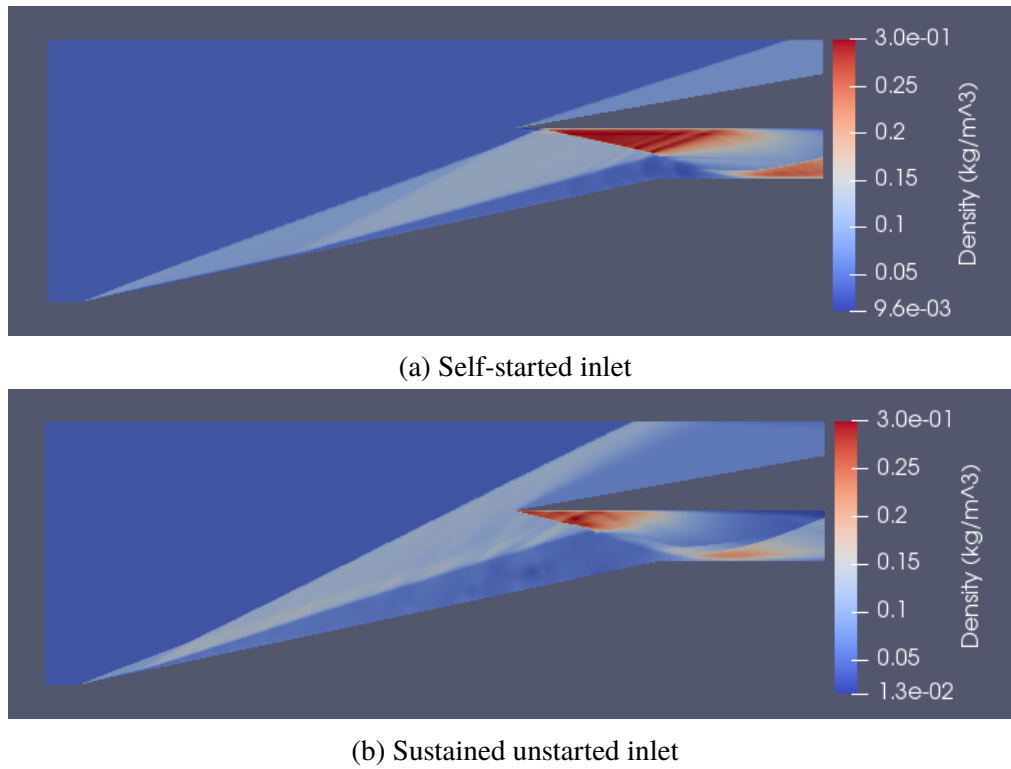


Figure 6.10: Density contours of started inlet (part a) and sustained-unstarted inlet (part b)

6.5 Restart Mechanisms

Simulations in the following section take the simulation result of the sustained-unstarted inlet as the starting point and then activate the restart mechanism.

6.5.1 Throat Suction

Figure 6.11 shows results from the 200 Pa restart suction mechanism at the inlet throat at 10 ms after initiation of the suction mechanism. The restart mechanism removes low momentum air from the inlet which decreases the boundary layer thickness allowing the inlet to restart. Figure 6.12 shows the reduction in pressure over the 10 ms period of activation of the suction port. Table 6.3 outlines final pressures measured at 10 ms.

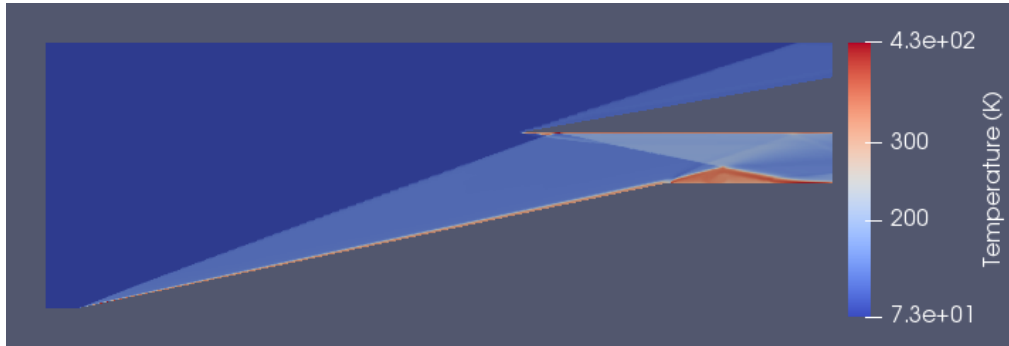


Figure 6.11: Temperature contour of inlet throat restart suction mechanism using suction at 200 Pa at 10 ms

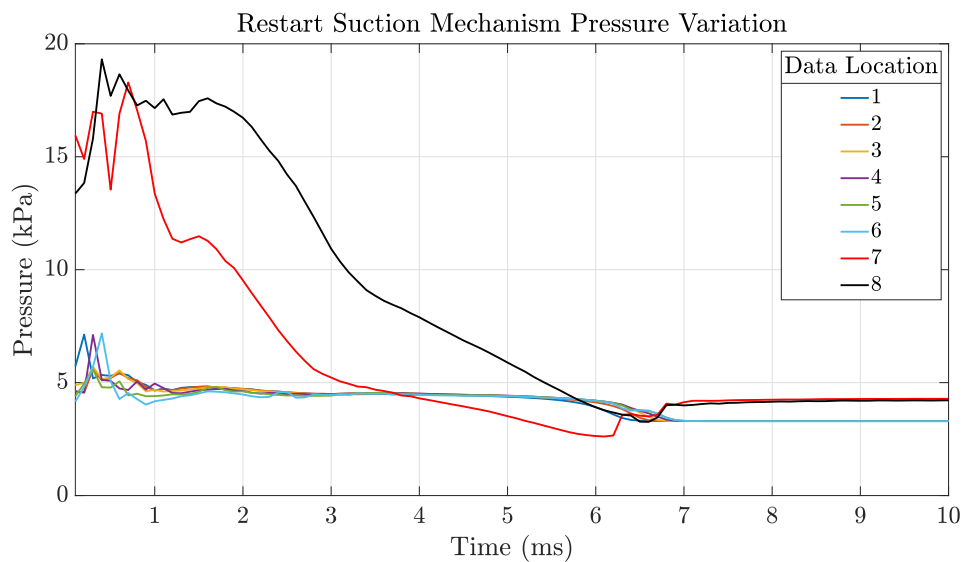


Figure 6.12: Restart suction mechanism pressure variation (refer to Figure 4.1 for positions of data locations)

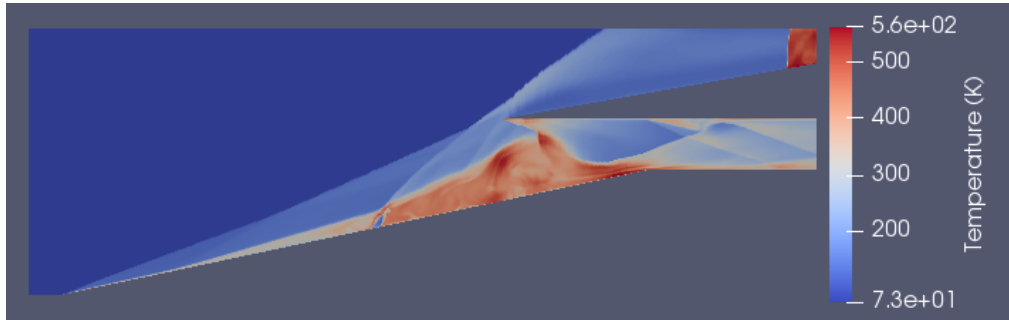
Table 6.3: Pressures at data locations at 10 ms after restart suction activation

Data Location	1	2	3	4	5	6	7	8
Pressure (kPa)	3.304	3.302	3.300	3.298	3.297	3.293	4.286	4.216

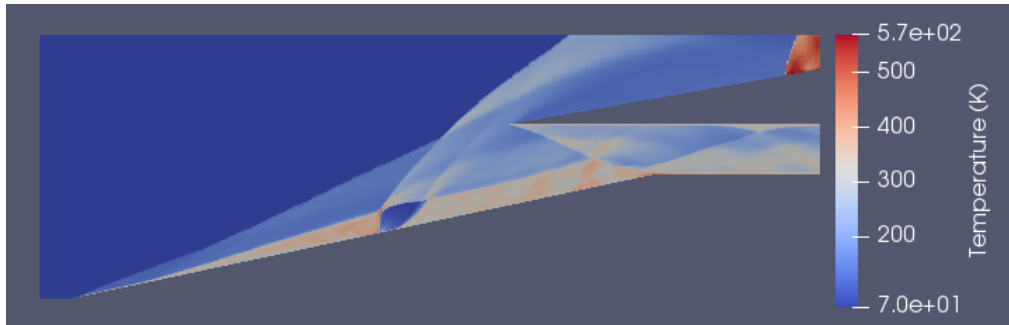
6.5.2 Mid-Ramp Injection

Figure 6.13 shows mid-ramp air injections at 12, 45, and 90 degree angles respectively after 1 ms using a 1 mm slot width. The 12 degree injection case in Figure 6.13a is seen to substantially increase the temperature of the boundary layer downstream of the

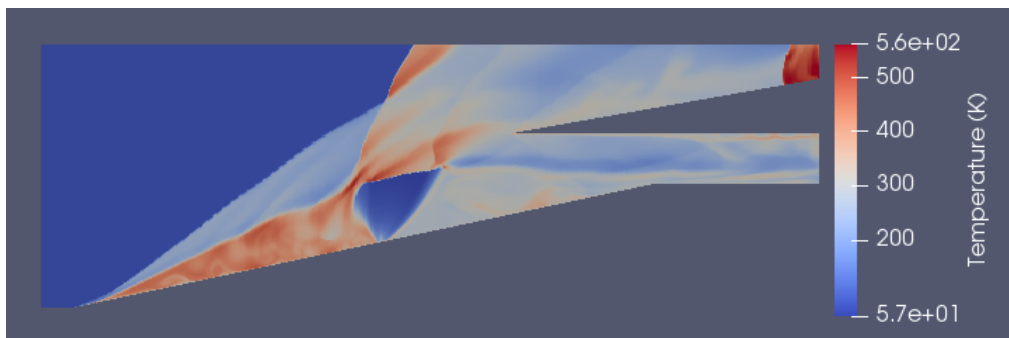
injection location resulting in thickening. Whereas the 90 degree injection in Figure 6.13c increases boundary layer thickness upstream of its location. The 45 injection as in Figure 6.13b shows a reduction in boundary layer thickness with a considerably lower boundary layer temperature than the other two injection cases. Deactivation of the injections will determine their overall effectiveness in restarting the inlet.



(a) 12 degree injection



(b) 45 degree injection



(c) 90 degree injection

Figure 6.13: Temperature contour of mid-ramp restart injection at 1 ms with a 100 kPa injection using various injection angles

6.5.3 Tip Injection

Figure 6.14 shows results of the activation of tip transverse air injections with a 1 mm slot at 100 kPa at injection times of 100, 250, 500 and 1000 μs respectively. The injection causes formation of a large bow shock at the inlet tip resulting in flow spillage over the cowl. At 1000 μs , removal of the ramp boundary layer is observed from the injected air. A high rise in temperature is observed directly upstream of the tangential injection due to the normal shock formed from the injection. Figure 6.15 shows the variation of temperature at the specified data locations along the inlet ramp, relative to the activation of the restart injection.

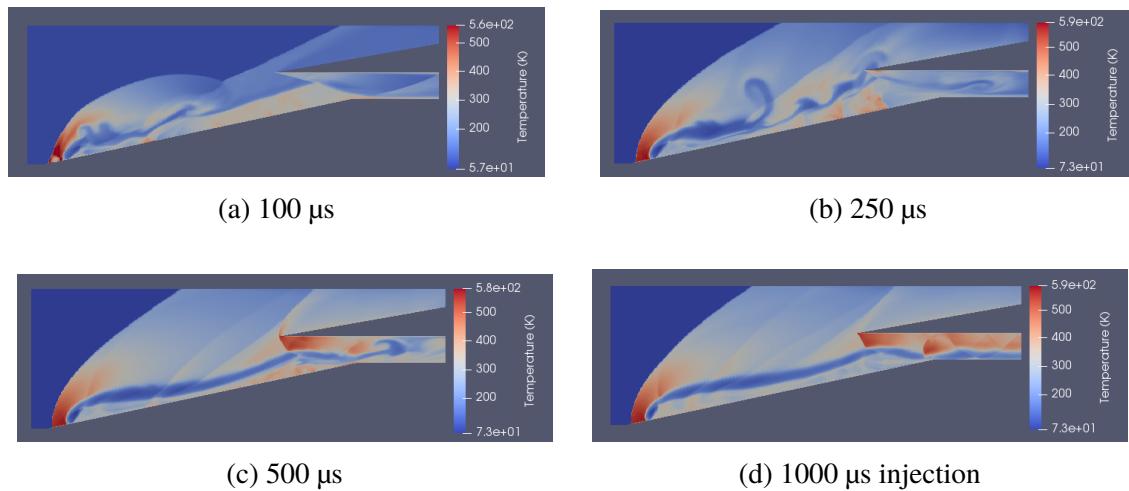


Figure 6.14: Temperature contours for the tip injection case at various times relative to the initiation of the mechanism with 100 kPa injection pressure (refer to Figure 4.1 for positions of data locations)

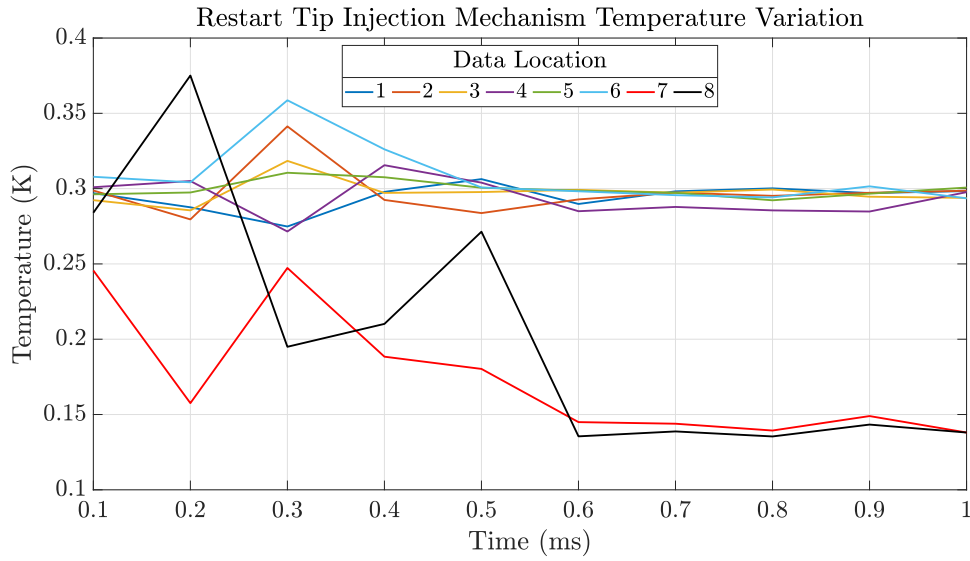


Figure 6.15: Restart tip injection temperature variation (refer to Figure 4.1 for positions of data locations)

Seen in Figure 6.15, locations 7 and 8 drop in temperature, plateauing at about 0.6 ms. This results from the jet plume from the injection entering into the isolator leading to a reduction in temperature in the isolator, reducing compression from the cowl-generated shock wave.

6.6 Restart

The following section uses flow results presented in Section 6.5 removing the restart mechanisms to determine their overall effectiveness in inlet restarting.

6.6.1 Throat Suction

Figure 6.16 shows the inlet after 5 ms after suction port deactivation. Results show that once the suction port is deactivated, the swbli generated from the cowl shock causes a regrowth of the recirculation region causing upstream boundary layer growth. This flow characteristic was also observed with the started inlet condition as seen in Figure 6.6. This similarity of these results suggests that inlet will remain in this started state. Figure

6.17 show the changes in pressures at the data locations.

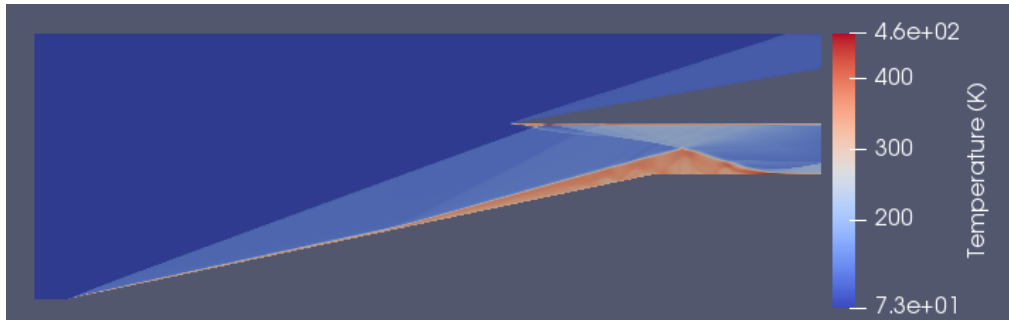


Figure 6.16: Temperature contour of inlet 5 ms after deactivation of inlet suction

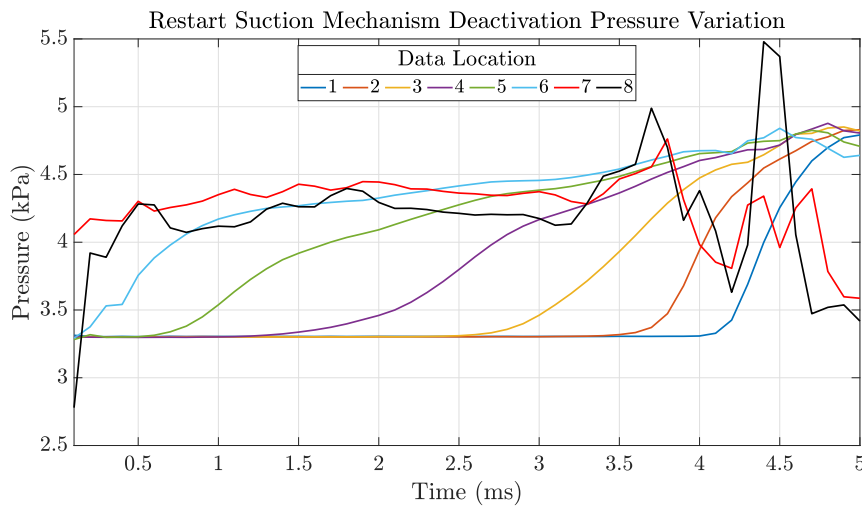
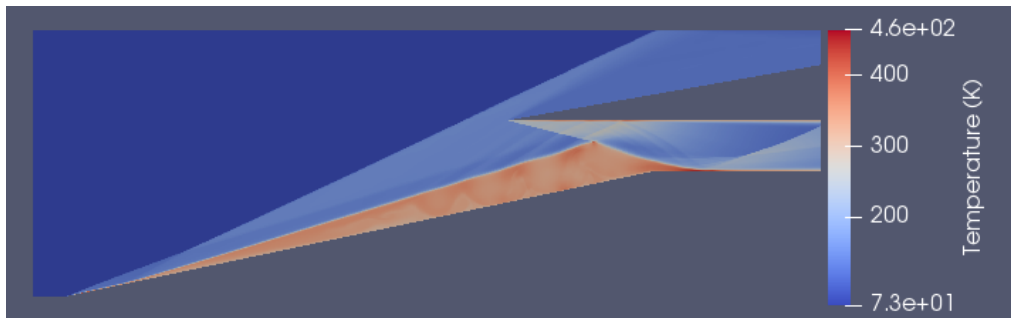


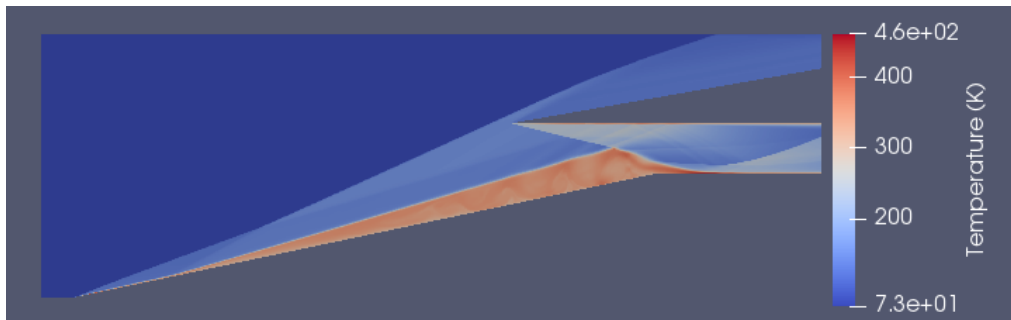
Figure 6.17: Restart suction mechanism deactivation pressure variation (refer to Figure 4.1 for positions of data locations)

6.6.2 Mid-Ramp Injection

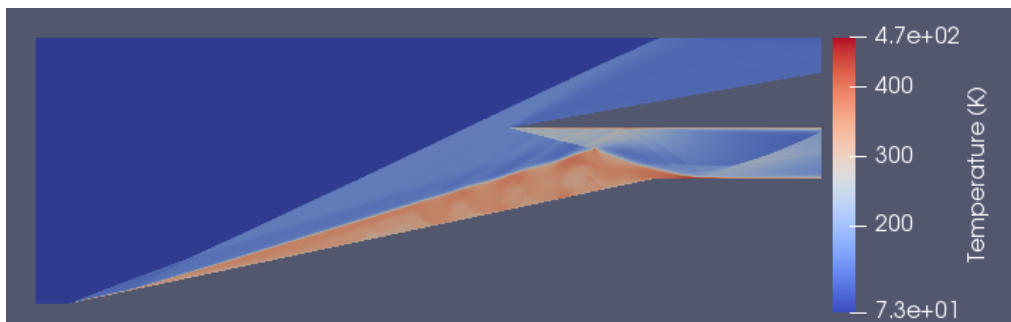
Figure 6.18 shows the inlet flow 5 ms after mid-ramp injection deactivation. Results indicate that the 45 degree injections is able to partially restart the inlet, however, substantial flow spillage over the cowl continued. The 12 and 90 degree injections seem to have made no effect, with the inlet remaining unstirred. Figure 6.19 shows the pressure at data location 6 after removal of mid-ramp injection.



(a) 12 degree injection deactivated



(b) 45 degree injection deactivated



(c) 90 degree injection deactivated

Figure 6.18: Temperature contours of inlets 5 ms after deactivation of the mid-ramp injection

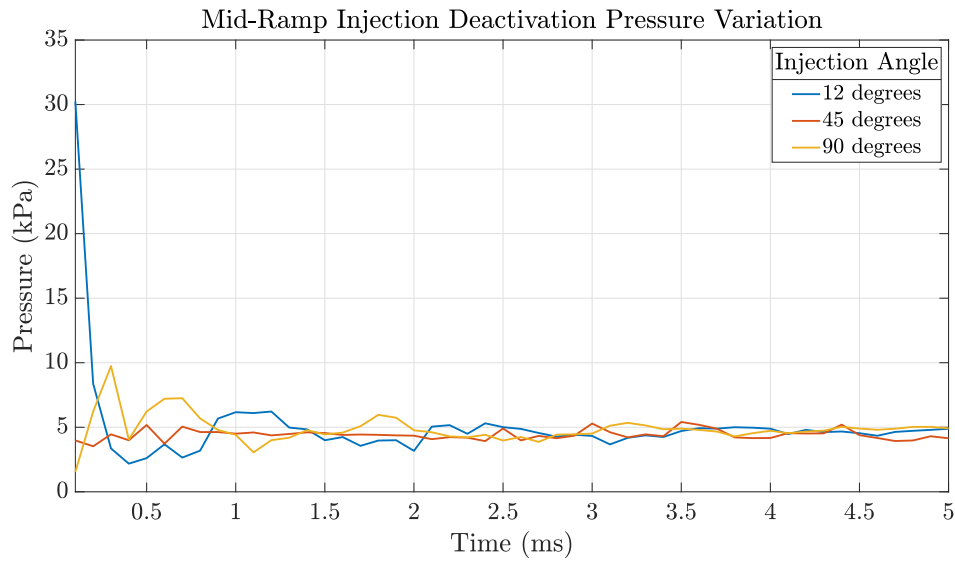


Figure 6.19: Pressure variation at data location 6 with removal of mid-ramp injection

6.6.3 Tip Injection

Figure 6.20 shows simulation results of tip injections. Regardless of tip injection duration, upon deactivation of the injection the inlet is able to restart. The 100 μs injection produced the most effective restart producing no flow spillage compared to other injections. Figure 6.21 shows the variation in pressure collected at location 8 (rear isolator) post to tip injection removal. Referring to 0.4 ms on Figure 6.21, spikes in pressure of varying magnitude are observed as result of removal of each of the injections. However, the 500 μs injection has two spikes in pressure at approximately 0.4 and 0.6 ms of approximately the same magnitude. Moreover, the 100 μs injection had two pressure spikes as well with slightly differing magnitude. Table 6.4 outlines the maximum pressure produced from each tip injection removal over the 5 ms flow duration. These results indicate some correlation between injection duration and the maximum pressure entering the isolator.

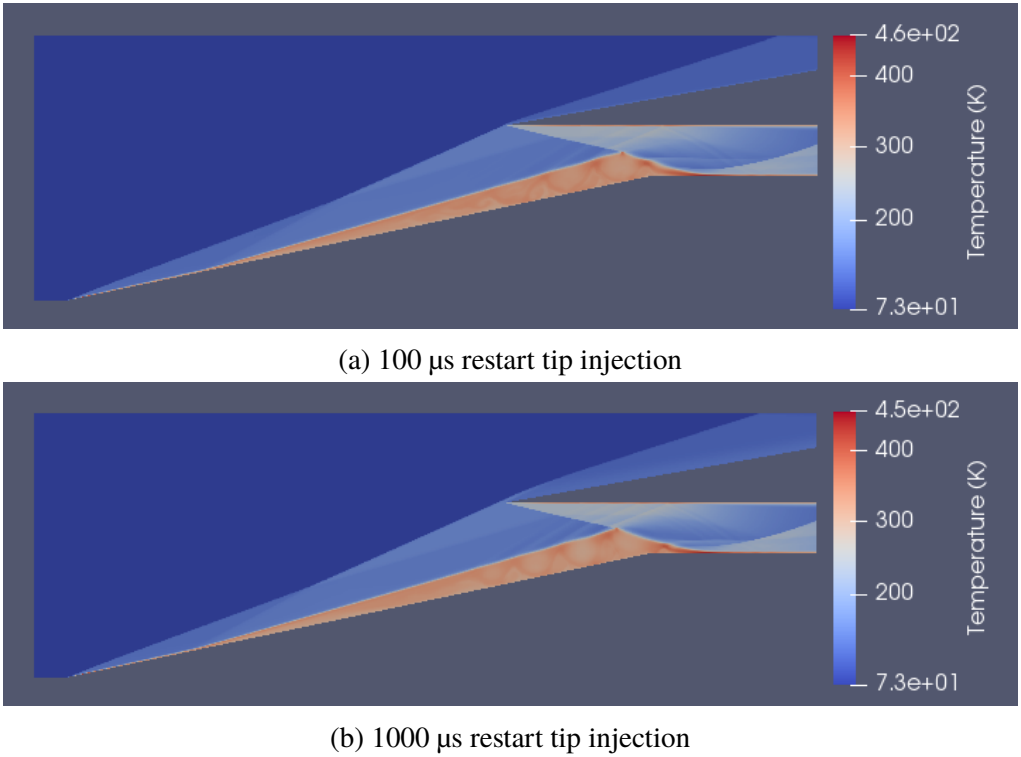


Figure 6.20: Temperature contours of restarted inlets 5 ms after deactivation of restart tip injection

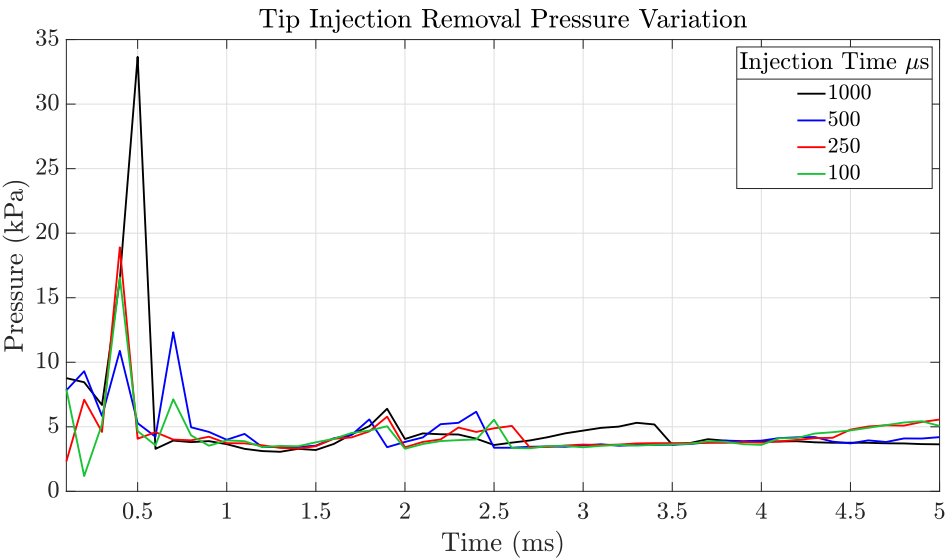


Figure 6.21: Pressure variation at data location 8 with removal of various tip injection durations

Table 6.4: Maximum pressure achieved upon removal of tip injection

<i>Injection Duration</i> (μs)	1000	500	250	100
<i>Max Pressure</i> (kPa)	33.67	12.32	18.90	13.59

6.7 Evaluation of Restart Mechanisms

Both the tip injection and throat suction restart mechanisms both effectively restart the inlet. However, the mid-ramp injections were unable to add enough momentum to the boundary layer to reduce its thickness, and consequently are unable to restart the inlet.

Comparing the tip injection and throat suction methods, using suction reduces the size of the recirculation region and consequently the boundary layer thickness to a greater degree than that observed with the tip injection method. However, the suction pressure used of 200 Pa is very low and may not be achievable in reality. Moreover, the duration required to restart the inlet is approximately 7 ms compared to that of the tip injection method in which of restarting the inlet occurred in approximately 1 to 2 ms. It is desirable to restart an unstarted inlet in as short a time as possible because an unstarted scramjet inlet is likely to critically compromise the net thrust produced by the engine. To validate the effectiveness of the suction restart method, simulations should be conducted at higher suction pressures to confirm if the inlet is still able to restart. However, the increase in suction pressure may result in the restart duration being extended. Experimental investigations will aim to verify the effectiveness of the tip injection method.

Chapter 7

Experimental Methodology

Contents

7.1	Test Model	73
7.2	Test Facility	75
7.3	Experimental Testing Procedures	77
7.4	Instrumentation and Setup	79

This chapter describes procedures and equipment used for experimental testing. The chapter begins by describing the construction of the experimental model and this is followed by a decription TUSQ Hypersonic wind tunnel facility. Different configurations of the inlet are then presented along with the instrumentation setup used to collect data.

7.1 Test Model

Figures 7.1 and 7.2 show the initial test model mounted in the TUSQ hypersonic wind tunnel. The main ramp of the model was manufactured using 3D printed material and a machined mild steel tip. The 3D printed PLA component was used to accommodate the complex injection plenum's and the pressure transducer ports. The steel tip was required to achieve a sharp leading edge on the ramp along with preventing any deflection that may have been caused by the hypersonic flow if 3D printed material were used. The two components were joined using a two part epoxy and sanded flush to remove the interface between the two components, avoiding the formation of additional shock waves. The ramp surface was coated in penetrol to give a smooth surface finish and prevent oxidation of the steel tip. The stand housing the ramp and cowl is made of 10 mm thick plate steel and the base plate was made of 12 mm plate steel. The side windows are constructed from Onyx 3D printed material from with a water jet cut 10 mm thick float glass insert joined using silicon. Appendix G describes the arrangement of the glass windows to more detail. Figure 7.3 shows a rendering of the experimental model.



Figure 7.1: Side view of initial model mounted in TUSQ hypersonic wind tunnel

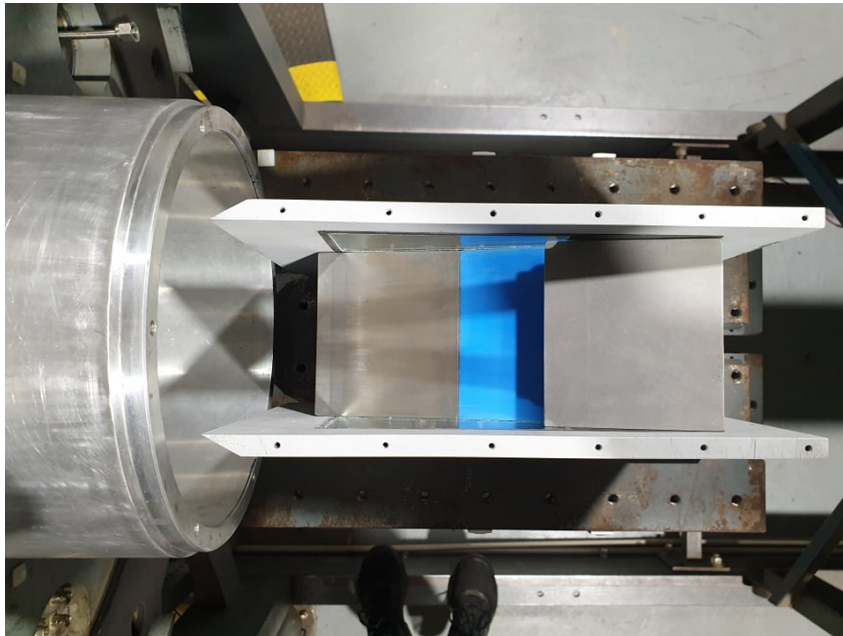


Figure 7.2: Top view of initial model mounted in TUSQ hypersonic wind tunnel

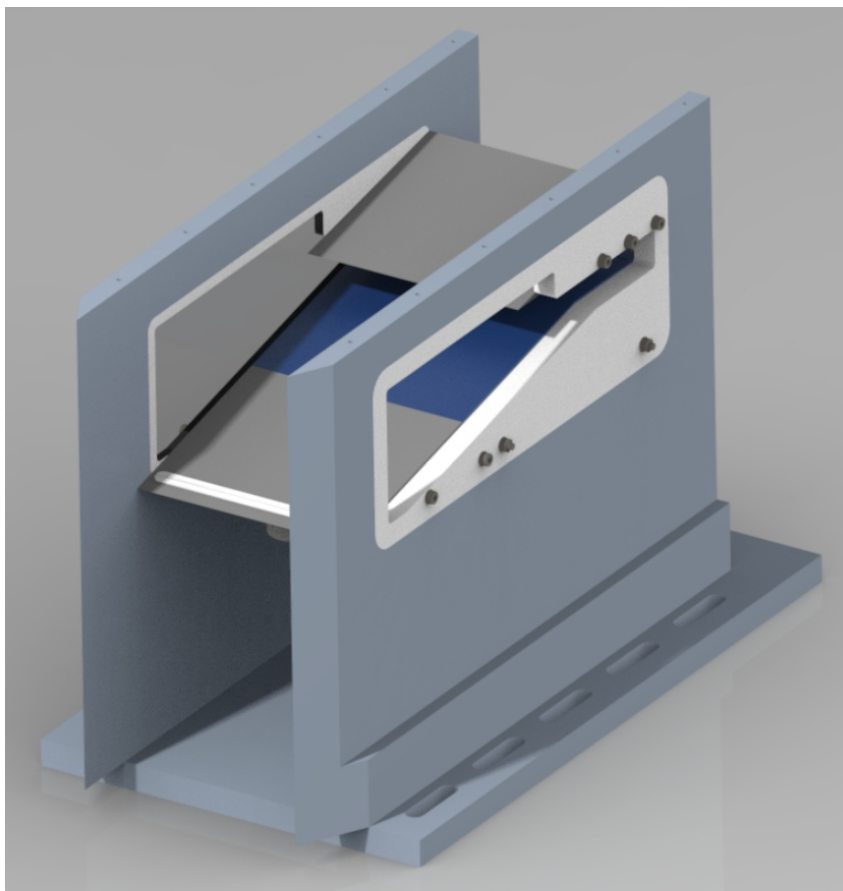


Figure 7.3: Isometric rendering of experimental inlet model

7.2 Test Facility

The test facility used for experimentation is the University of Southern Queensland Hypersonic Wind-Tunnel (TUSQ) illustrated in Figure 7.4. This facility is unique compared to other hypersonic testing facilities in Australia as it provides a comparatively long test flow duration, allowing for the study of unsteady processes such as scramjet inlet start-ability.

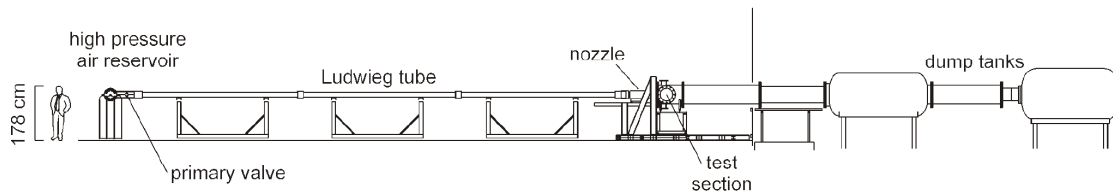


Figure 7.4: General arrangement of the wind tunnel facility (Buttsworth & Smart 2010)

The facility is typically operated as a free piston compression Ludwig tunnel producing supersonic and hypersonic low enthalpy flows to simulate aerodynamic conditions with flow Mach numbers ranging from Mach 2 to Mach 7. Test durations are in the order of 200 ms, but actual duration varies depending on the tunnel configuration. The facility is able to be configured for two modes of operation: either as an atmospheric blow-down facility or as a Ludwig tunnel, with or without free piston compression heating.

For this work the tunnel was used in piston-driven mode with a reservoir pressure of 3 MPa, barrel pressure of approximately 94 kPa and a test section pressure below 1 kPa. A pneumatically actuated ball valve opens to release the high pressure air which pushes the piston forwards, compressing the test gas within the tube. When the air reaches approximately 1 MPa, a 100 μm mylar diaphragm located at the entry of the converging section of the nozzle ruptures, allowing the air to accelerate through the nozzle and enter into the test section. Pressure in the barrel is measured using a PCB 113A03 piezoelectric pressure transducer located 130 mm upstream of the nozzle entrance. The transducer is amplified by a Kistler type 5015 charge amplifier and the signal from this pressure transducer is used to trigger data acquisition equipment. The facility Mach 6 nozzle illustrated in Figure 7.5 has a throat diameter of 28.8 mm, an exit diameter of 217.5 mm

and a length of 1057 mm. A typical barrel pressure trace is presented in Figure 7.6. Table 7.1 presents the test conditions used in the tunnel runs.

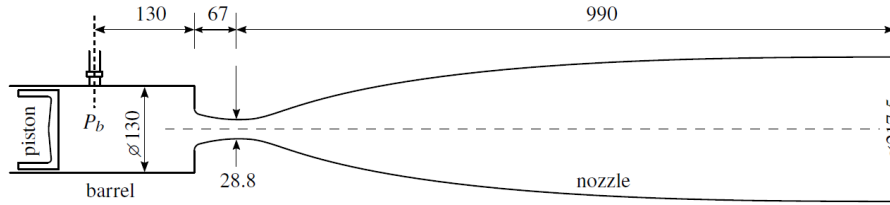


Figure 7.5: TUSQ Mach 6 nozzle sketch (Birch et al. 2018)

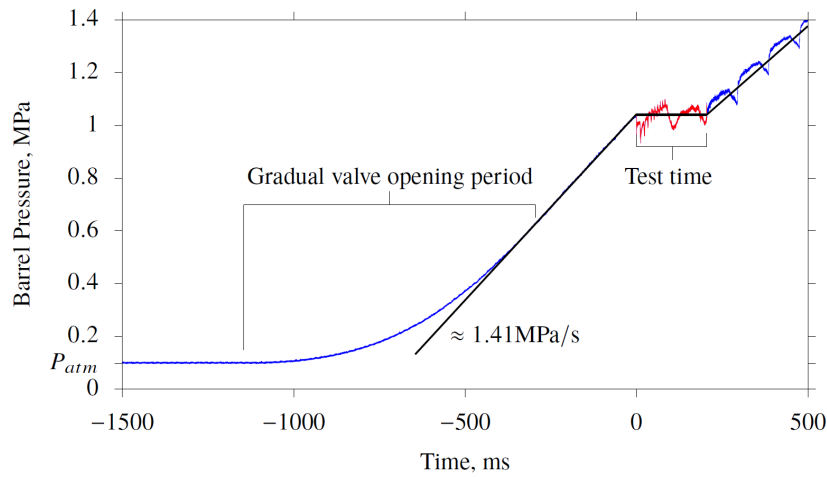


Figure 7.6: Typical barrel pressure history. Time data offset with start of test time at $t = 0$ s (Birch et al. 2018)

Table 7.1 outlines the test conditions used in the tunnel runs.

Table 7.1: Experimental Test Conditions

Run No.	Ambient Conditions		Driver Pressure	Diaphragm Thickness	Test Section Pressure	
	P_{atm} (kPa)	T_{atm} (K)			P_{red} (kPa)	P_{green} (Pa)
915	94.36	21.50	3 MPa	100 μ m	-93.84	610
916	94.44	22.60			-93.59	980
932	95.26	20.0			-94.53	700
933	94.38	25.3			-93.76	720
943	94.38	25.0			-93.75	580

7.3 Experimental Testing Procedures

The experimental component of the investigation was broken into three separate campaigns as follows

- **Startability Assessment** Use the ramp shown in Figure 7.7, assess if the inlet was able to self start under the given flow conditions by taking observations using Schlieren visualisation. The initial investigation determined modifications required for the model and experimental methodology.
- **Ramp Pressure Measurement** Gather pressure measurements along the ramp using the ramp as shown in Figure 7.8. The placement of these pressure measurements is indicated in Figure 4.1.
- **Unstart and Restart Injections** Test final model configuration using the ramp as shown in Figure 7.9. The final ramp integrates slotted sonic air injection ports at the rear for the unstart injection, and at the tip used for the restart mechanism. The unstart injection will first be tested, determining the required injection pressure and duration required to produce a sustained unstart in the inlet. The restart mechanism will then be tested determining the pressure and duration required to restart the inlet.

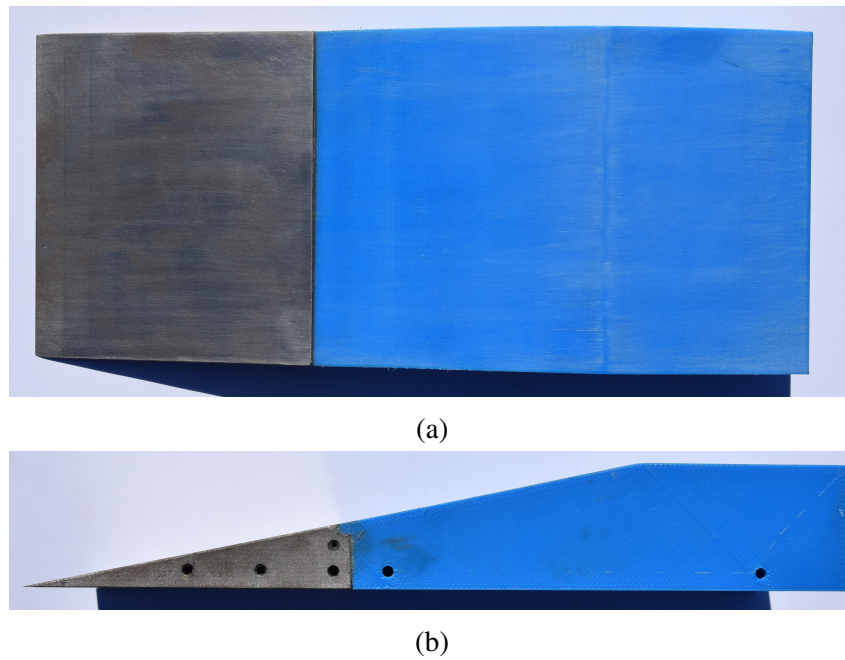


Figure 7.7: Initial model ramp shown in top view (part a) and side view (part b)

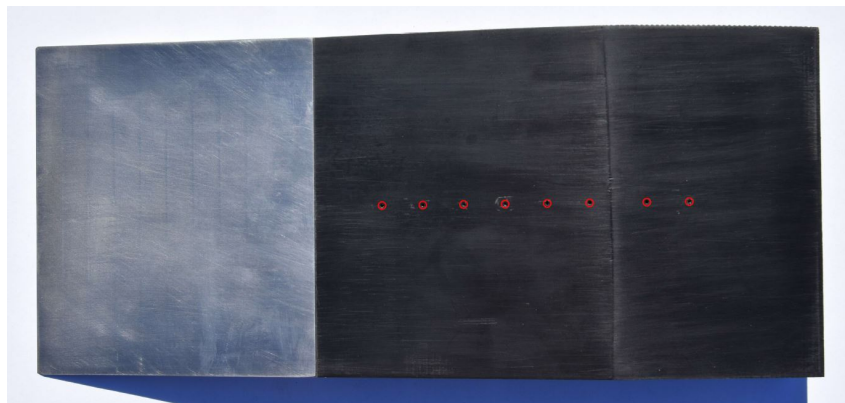


Figure 7.8: Second model ramp with pressure transducer locations equally spaced along mid-line indicated by red circles

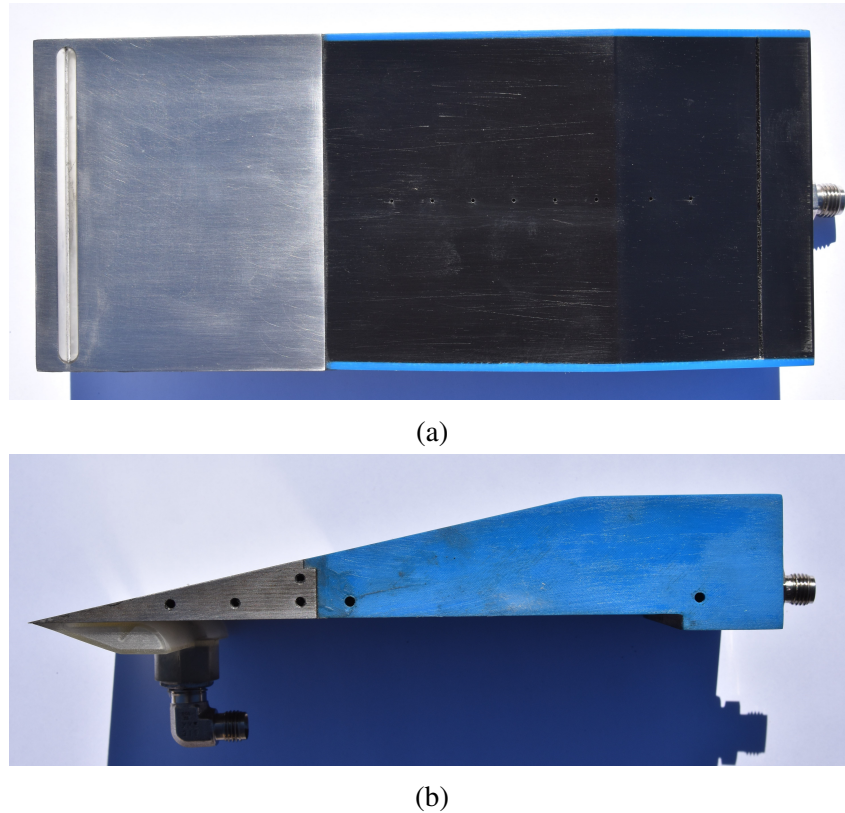


Figure 7.9: Final ramp configuration with pressure transducers equally spaced along the mid-line and slots for air injection at the rear and tip (part a) shows the top view; and (part b) shows the side view

7.4 Instrumentation and Setup

7.4.1 Schlieren Visualisation

The Schlieren set-up used for the TUSQ hypersonic wind tunnel is a variant of a Z-type Schlieren arrangement shown in Figure 7.10. A LED light source with fibre optic coupling was used with a spherical mirror to collimate the light rays through the test section and refocus the light onto a razor's edge which blocked the refracted light rays, allowing the camera to capture an image of the density gradient. The razor's edge was placed in two configurations: cutting off rays refracted upwards in the first orientation and downward refracted rays in the second orientation. The second configuration reversed the density contrast of the image, allowing for clearer visualisation of boundary layers and

shock waves depending on their direction.

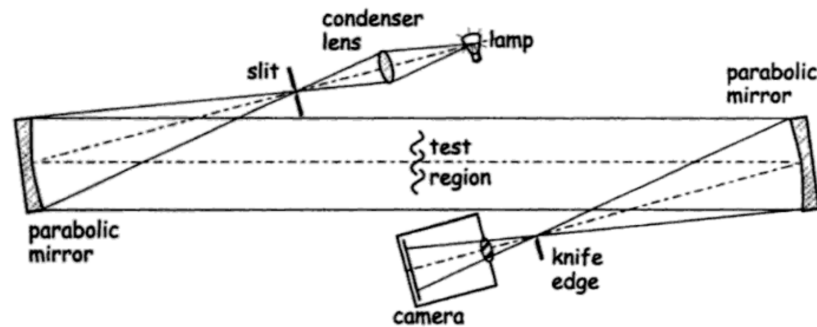


Figure 7.10: Z-type Schlieren System (Cristofolini et al. 2012)

7.4.2 Ramp Pressure Transducers

To take absolute pressure measurements along the inlet ramp, pressure transducers were integrated into the ramp. Referring to Table 4.2, a maximum pressure of approximately 10 kPa is produced in the inlet. However, the unstart simulations with CFD indicate a maximum pressure of 97 kPa. Kulite pressure transducers rated to 1.7 bar were available and had a manufacturer specified rupture pressure of 340 kPa. Two 3.5 bar pressure transducers were used as a safety precaution in the inlet throat (referring to locations 7 and 8 in Figure 4.1) in case a pressure higher than expected occurred during unstart.

If the pneumatic line connecting the pressure transducers to the ramp surface is long, there may be delay in the signal response due to transient compression of air in the line. However, if the transducer tip surface were mounted flush with the ramp surface, unwanted shockwaves may form in the inlet due to deflection of the flow. To keep the delay in pressure measurement to a minimum, the pressure transducer should be mounted as close as possible to the ramp surface. Figure 7.11 shows the mounting arrangement: the transducer is mounted below the ramp surface and connected via a short air cavity. Figure 7.12 shows the mounting arrangement of pressure transducers along the mid-line of the ramp.

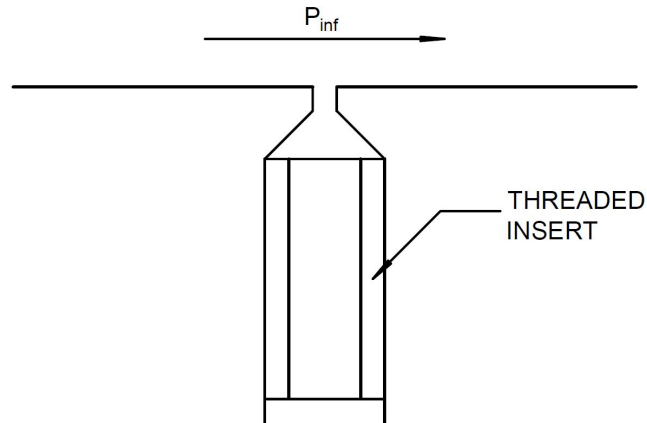


Figure 7.11: Mounting for pressure transducer

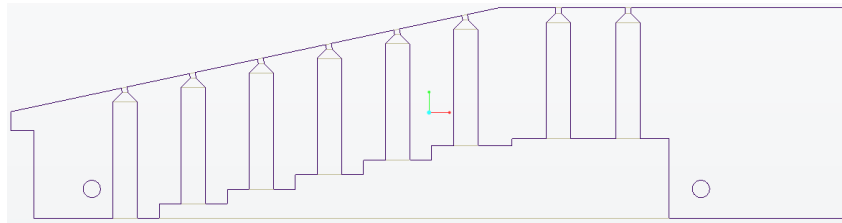


Figure 7.12: Cross-section of 3D printed ramp showing arrangement of transducer mounting. Note: additional transducers aren't added to the rear of the ramp to accommodate unstart injection port

7.4.3 Data acquisition and calibration

Analog output signals from pressure transducers were converted to digital form using a National Instruments PXI-6123 multifunction data acquisition system (DAQ). Data was stored in a text file using NI-DAQmx (National Instruments software) which was then processed further to convert recorded voltage levels into meaningful units via separate calibrated sensitivities of the transducers.

Chapter 8

Experimental Results and Discussion

Contents

8.1	Self-Started Inlet	83
8.2	Unstart Injection	90

Experimental results from the 2D hypersonic inlet are presented in this chapter. Measurements are taken using Schlieren visualisation and pressure measurements along the model inlet ramp. Discussion of the results identifies external effects that may be impacting the data.

8.1 Self-Started Inlet

8.1.1 Initial Model Configuration

The initial model configuration, as presented in the Chapter 7, was used to determine the startability of the inlet based on Schlieren imaging. The imaging was also used to determine if there were a reduction of the core flow Mach cone angle due to test section pressure rise caused by the additional blockage caused from the model.

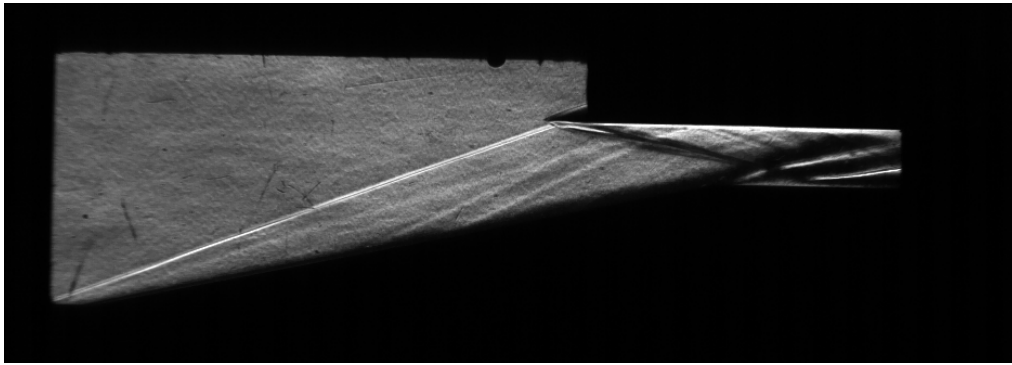


Figure 8.1: Run 915 Schlieren of self-started initial ramp configuration at steady conditions at 30 ms of flow duration

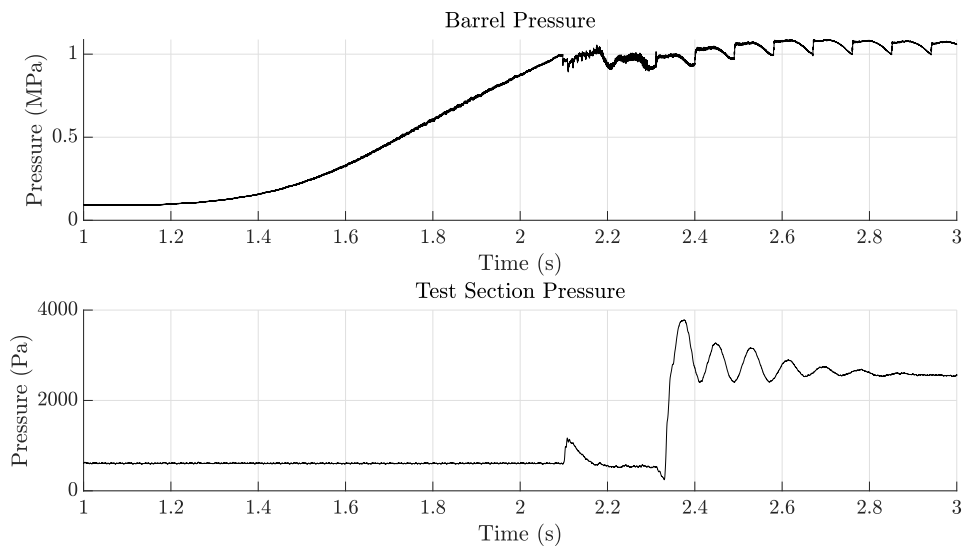


Figure 8.2: Run 915 barrel and test section pressure history

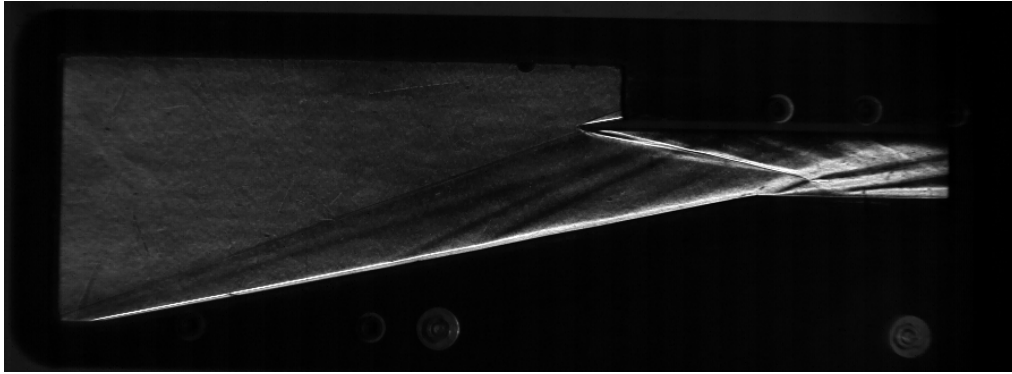


Figure 8.3: Run 916 Schlieren of self-started initial ramp configuration at steady conditions at 30 ms of flow duration. Schlieren knife edge is reversed to better display the boundary layers on the ramp

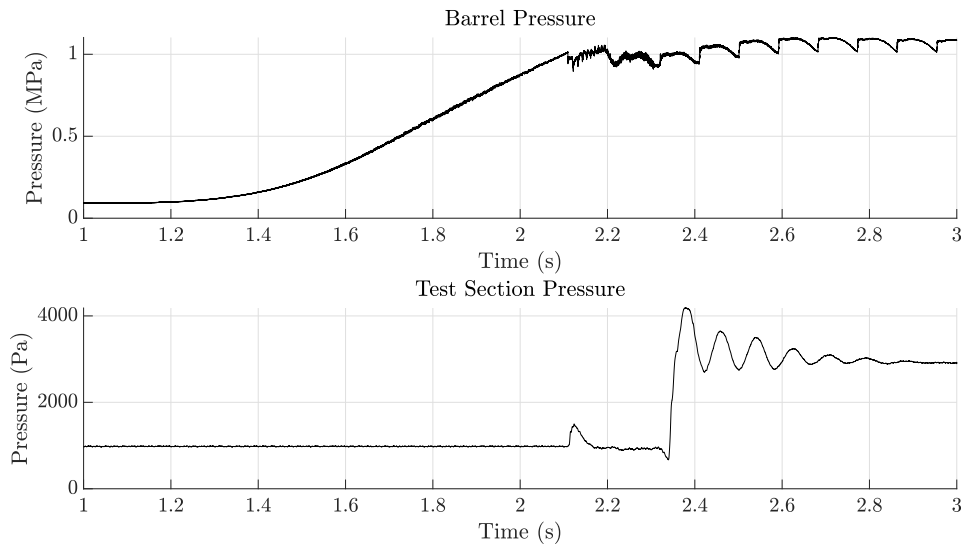


Figure 8.4: Run 916 barrel and test section pressure history

Figures 8.1 and 8.3 show the leading shock wave impinges on the top isolator wall and reflects back down into the inlet, producing a large recirculation region. Note that the shock-on-lip condition is not achieved because the isolator height was 15 mm for these experiments whereas the original design used a 10 mm isolator height. Further analysis of this reflection is presented in Chapter 9. Figure 8.5 shows a line drawing of the reflected leading shock.

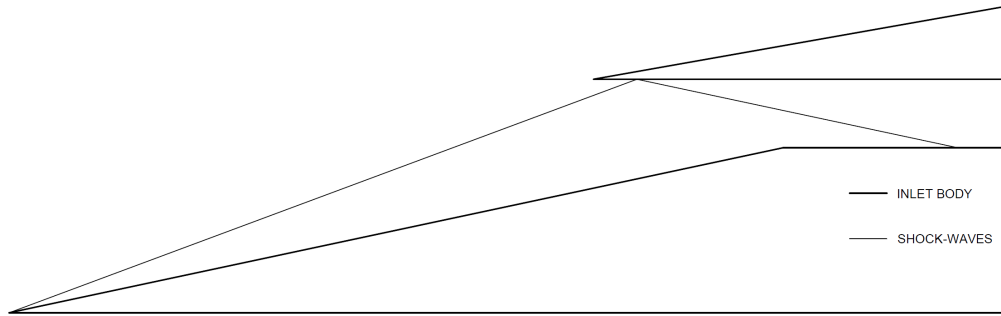


Figure 8.5: Schematic of leading edge shock wave reflected on upper isolator wall

At least two additional shock waves are also observed in Figures 8.1 and 8.3, generated in the middle of the ramp. The shock waves may have been generated from the metal tip to 3D print component interface, however the shock waves seem to be relatively weak, and have minimal effect on the inlet shock structure.

8.1.2 Second Model Configuration

The second ramp configuration was tested to obtain pressure transducer measurements along with Schlieren imaging. Shown in Figure 8.6, the inlet flow field generates a shock structure similar to results to the initial ramp configuration as shown in Figures 8.1 and 8.3. However, comparing test section pressure shown in Figure 8.7 to the test section pressure observed with the initial ramp configuration shown in Figures 8.2 and 8.4, a higher pressure is recorded during the flow duration of approximately pressure of 2.3 kPa. This difference in test section pressure because of additional blockage caused from the pressure transducer fixed to the underside of the model.

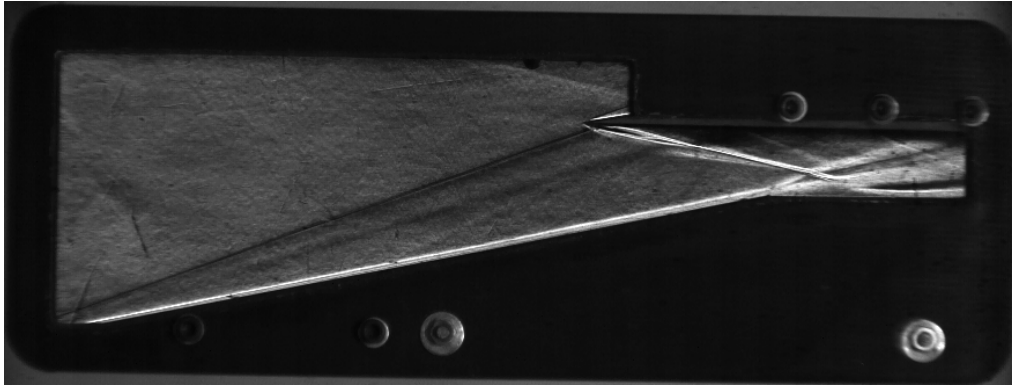


Figure 8.6: Run 943 Schlieren of Self-Started Second model configuration at steady conditions at 30 ms of flow duration

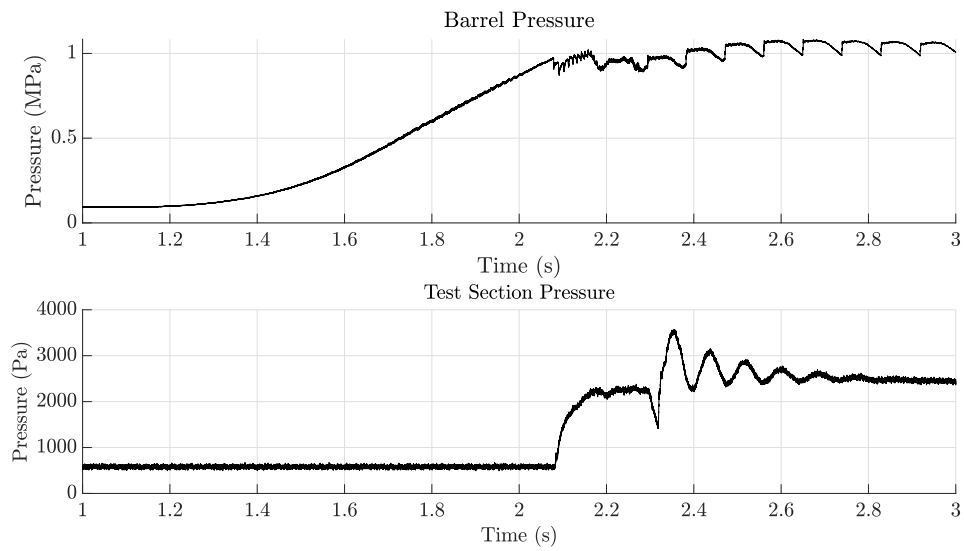


Figure 8.7: Run 934 barrel and test section history

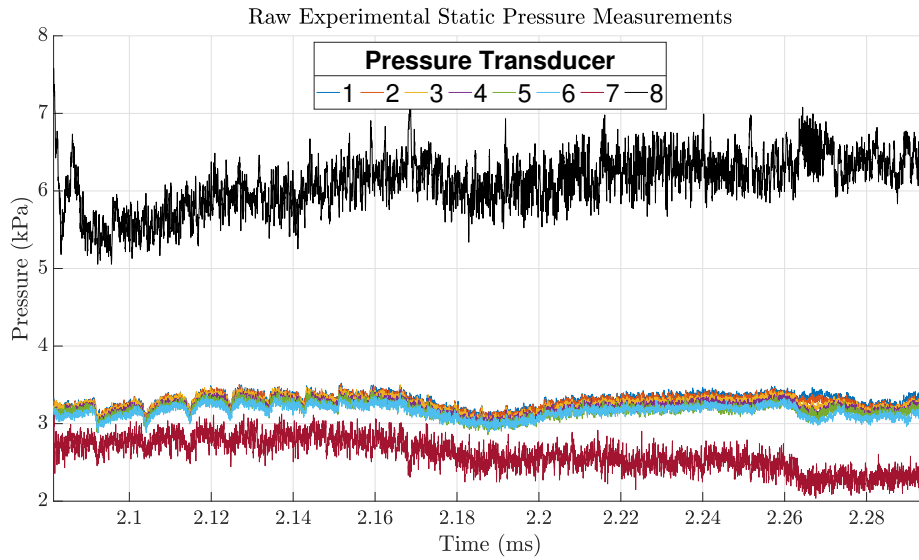


Figure 8.8: Raw experimental static pressure measurements over steady test duration (refer to Figure 4.1 for positions of data locations)

Figure 8.8 presents the data from the pressure transducers on the ramp surface. Locations 1 through 6 share very similar pressures of approximately 3.3 kPa. This indicates that the pressure distribution along the ramp is reasonably constant with upstream effects from the separation region have minimal effect. Upon closer inspection, the pressure at location 1 gradually decreases through to location 6. This change in pressure results from the growth of the boundary layer reducing the turning angle of the leading shock wave, thus reducing the leading shock strength. Moreover, as the flow is turned downward due to curvature of the boundary layer, expansion waves form along the boundary layer leading to a reduction in pressure. At location 7, a reduction in pressure occurs as this position corresponds to the separation region. The slight reduction in pressure results from the expansion wave formed over the separation region, reducing pressure within the recirculation region itself. Location 8 shows a substantially elevated pressure as it is located behind the reflected leading shock wave.

8.1.3 Final Model Configuration

Due to additional blockage to the Mach 6 nozzle flow from the additional injection ports on the final ramp configuration, self-starting tests were initially conducted as outlined in Appendix G. No pressure transducers were used during the run to prevent damage should pressures rise above pressure limits.

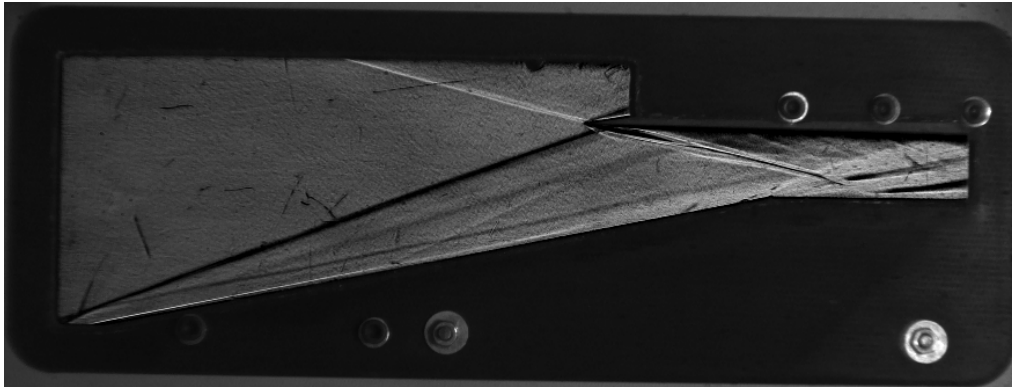


Figure 8.9: Run 932 Schlieren of Self-Started Initial ramp configuration at steady conditions at 30 ms of flow duration.

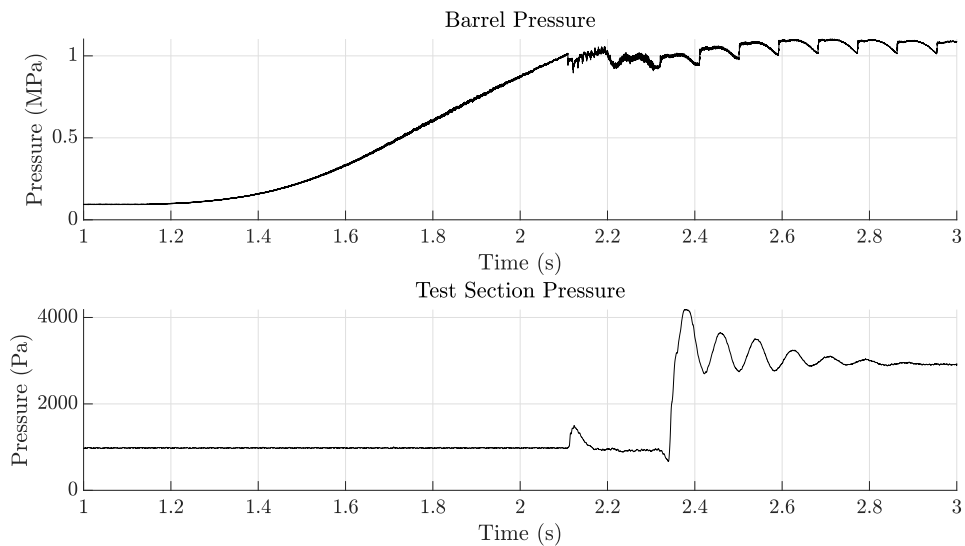


Figure 8.10: Run 932 barrel and test section history

Figure 8.9 illustrates the shock structure largely matches that of the initial and second ramp configurations. Note that the shock wave entering the field of view from above arose because of the addition of a model roof to prevent flow collapse of the Mach cone. However, an additional density feature parallel to the inlet ramp is generated due to the slotted tip injection port (refer Figure 7.9a). Unlike the second ramp configuration, test section pressure as illustrated in Figure 8.10 does not rise to elevated pressures from increased flow blockage from injection component as shown in Figure 7.9b due to an additional wedge which generates two oblique shock waves rather than a large bow shock with the original configuration as illustrated in Figure 8.11.

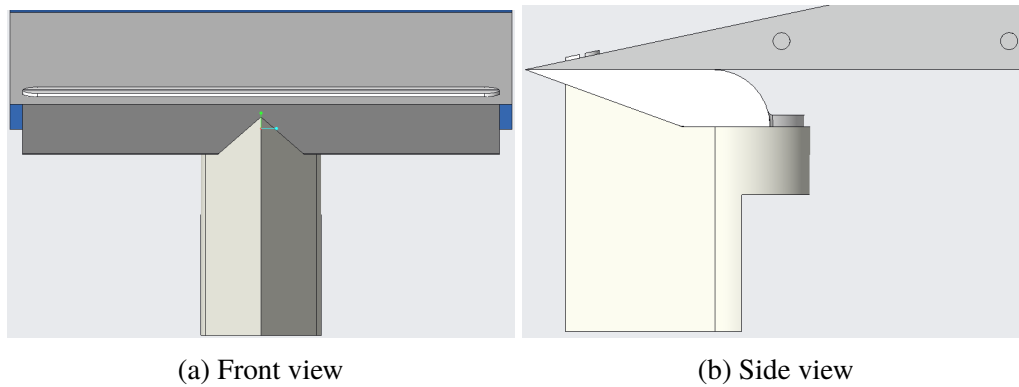


Figure 8.11: Wedge shielding injection components of final ramp configuration

8.2 Unstart Injection

Figures 8.12a and 8.12b shows results from the applied unstart injection using a pressure reservoir at 600 kPa. Due to high pressure loss through the injection plenum, the required injection pressure to cause significant blockage was unable to be achieved. As illustrated in Figure 8.13, minor deflection of reattachment shockwave is observed due to the injection, however no significant effect on the upstream flow characteristics is observed.

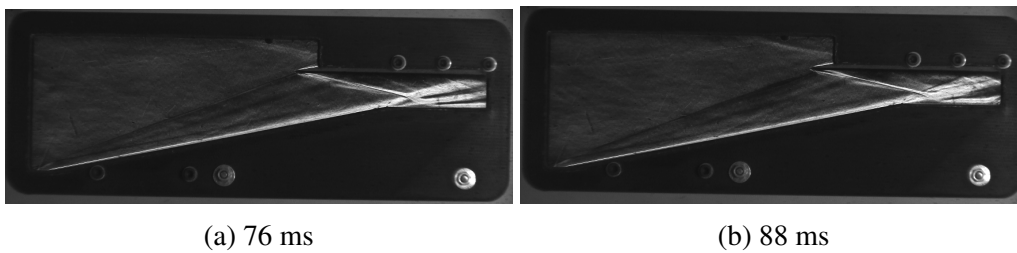


Figure 8.12: Run 933 Schlieren of self-started inlet prior to unstart injection (part a) and upon unstart injection at the isolator rear (part b)

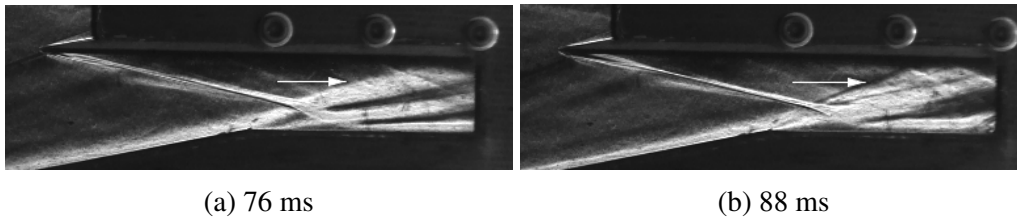


Figure 8.13: Run 933 Schlieren of self-started isolator prior to unstart injection (part a) and upon unstart injection at the isolator rear (part b) - arrow indicates deflected reattachment shockwaves

Chapter 9

Results Analysis and Discussion

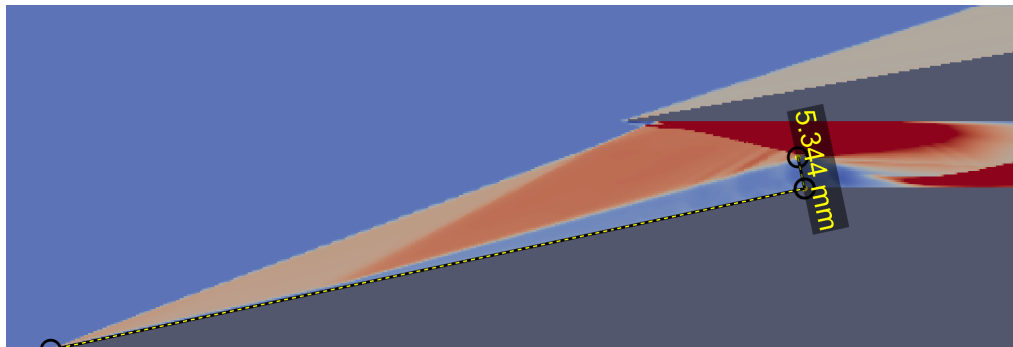
Contents

9.1	Boundary Layer Thickness Comparison	92
9.2	Shock Angle Comparison	93
9.3	Ramp Pressure Comparison	94
9.4	Conclusion of Results	98

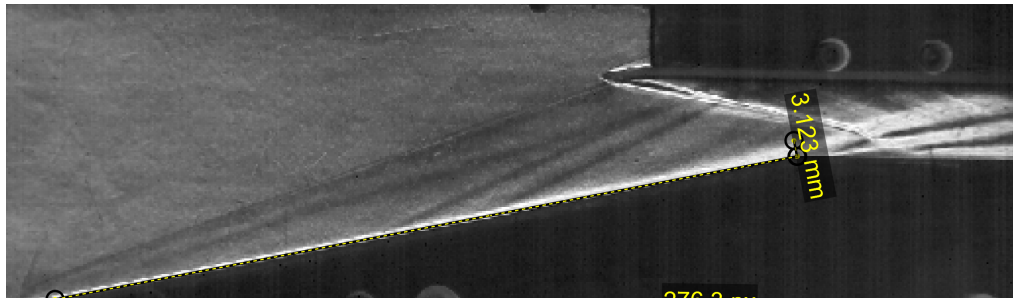
Analysis of analytical, numerical and experimental results is presented. Comparisons of various flow field characteristics including boundary layer thickness, shock wave angles and ramp pressure measurements was investigated. Discussion of the presented results is also made identifying the key reasons for differences between the analysed results. Comparison of the results helps give confidence the restart methods tested numerically will indeed work.

9.1 Boundary Layer Thickness Comparison

Figure 9.1 compares boundary layer thicknesses from steady simulated and experimental results. The presence of the separation region at the inlet throat results in the boundary layer thickness at the top of the ramp being considerably thicker than the analytically calculated value of 1.78 mm.



(a) Simulation



(b) Experimental

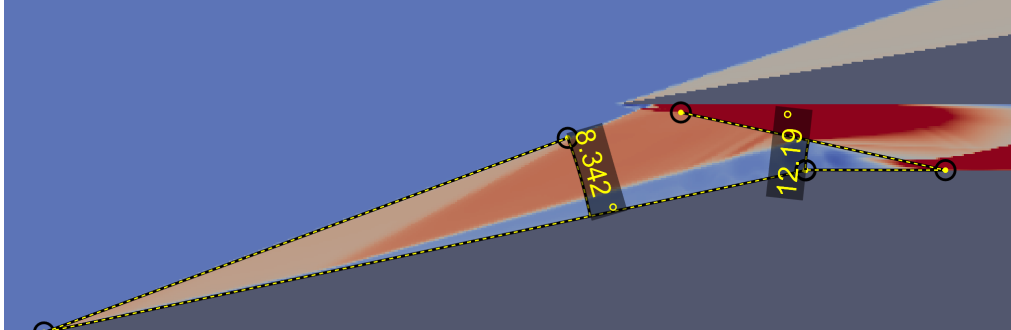
Figure 9.1: Comparison of simulation and experimental boundary layer thickness at steady state conditions

However, the simulated results produced a far thicker boundary layer of approximately 5.344 mm compared to the experimental results producing a boundary layer thickness of 3.123 mm. This possibly occurred as the simulated flow was modelled as perfectly laminar whereas experimental conditions the boundary layer would have at least partially transitioned to turbulent. In turn, the boundary layer in the experimental conditions is less prone to separation, and thus its growth is less severe compared to the simulation results. As the laminar boundary layer separates more readily, the boundary layer thickness is observed to grow rather more upstream resulting in a large separation shock formed

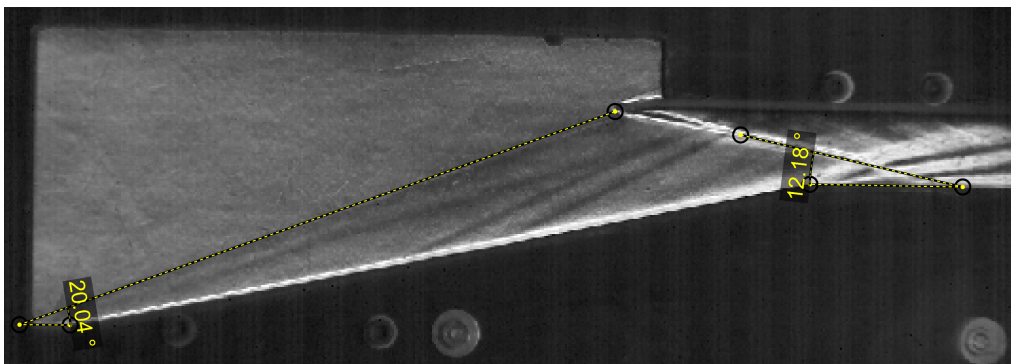
upstream in the inlet, as discussed further in later sections. Moreover, the separation region in the simulation results is observed to move further forward than in the experimental results due to its larger size.

9.2 Shock Angle Comparison

Figure 9.2 compares shock angles from simulation and experimental results. Both simulation and experimental results have similar leading shock angles: 20.3° ($8.3 + 12.0 = 20.3^\circ$) for the simulation case and 20.0° for the experimental case. Due to the additional boundary layer growth in the simulation case, upward movement of the shock wave is expected to be more than that of the experimental case. Furthermore, both simulation and experimental leading shock angles are greater than the analytically calculated leading shock of 19.8° , which is reasonable since no boundary layer displacement effect was included in the analytical shock angle calculation.



(a) Simulation



(b) Experimental

Figure 9.2: Comparison of simulation and experimental shock wave angles at steady state conditions

Measured cowl generated shock waves have smaller angles than the analytically calculated value of 13.5° . In both the experimental and simulation results the cowl-generated shock angle is as shown in Figure 9.2 approximately 12.2° .

Figure 9.3 shows interactions and reflections of the leading shock and cowl shock waves relative to the original design. The cowl shock wave refracts on interaction with the leading shock from the ramp surface, and this leading shock wave also reflects from the cowl surface. This occurred as the cowl was raised by 5 mm.

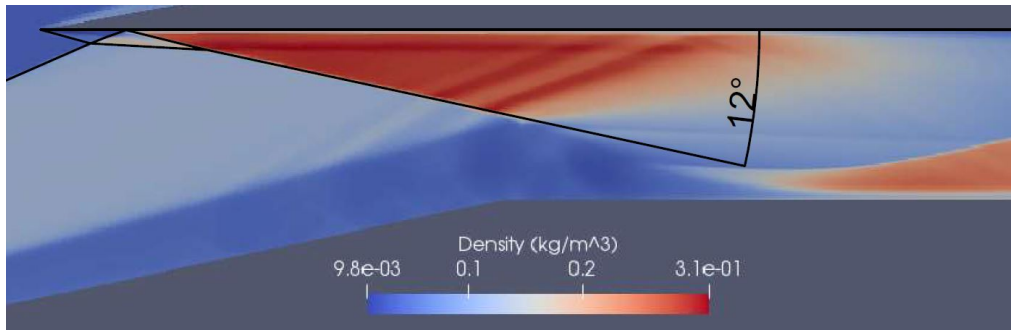


Figure 9.3: Simulated shock interaction and reflection in isolator

9.3 Ramp Pressure Comparison

Figure 9.4 compares pressures at the specified points from the analytical, numerical and experimental results. Pressure for both numerical and experimental results were averaged from 40 to 50 ms of the inlet reaching steady conditions.

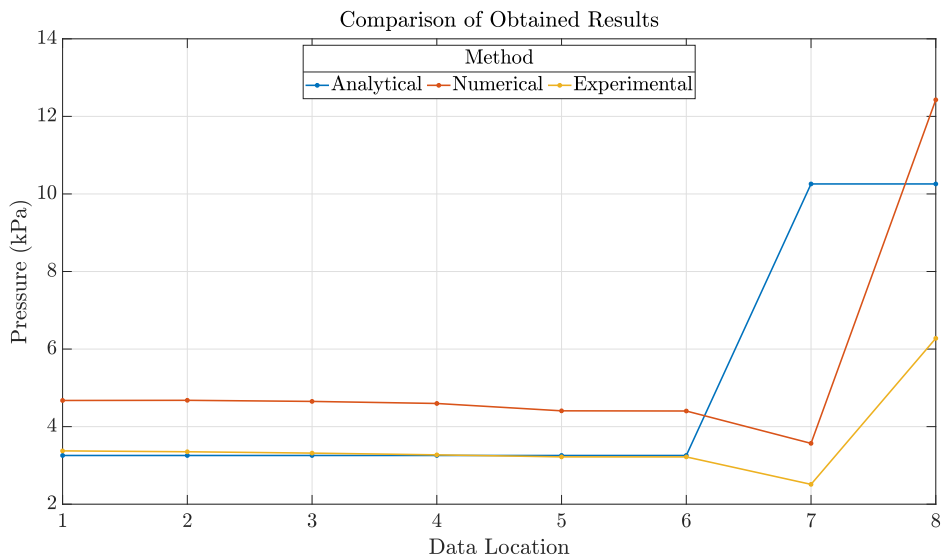


Figure 9.4: Comparison of pressure measurements obtained analytical, numerical and experimental results

Referring to Figure 9.4, there is a strong correlation between the analytical and experimental results for locations 1 through 6. However, numerical results are at a higher pressure compared to analytical results. This difference in pressure occurs due to a separation shock wave formed from boundary layer thickening from the separation region at the inlet throat. Figure 9.5 indicates the angle of the shock to be approximately 15.1°.

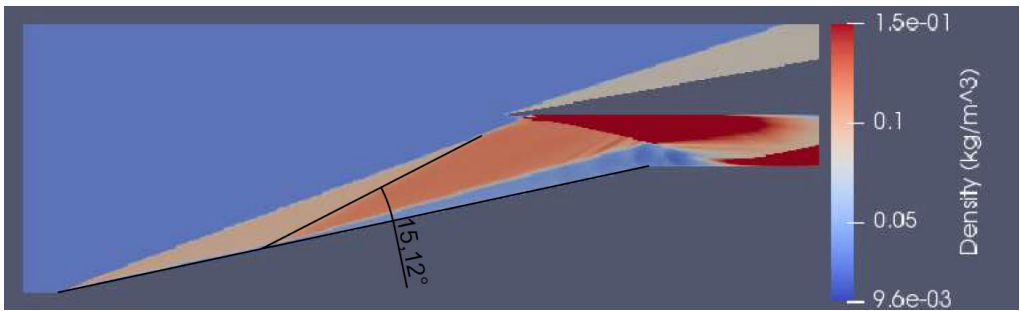


Figure 9.5: Density contour of started inlet indicating separation shock angle

To confirm that this additional shock indeed caused this rise in pressure, the angle of the shock associated with the observed rise in pressure is calculated analytically

Averaging simulated pressure from points one through six we find that

$$p_3 = 4.57 \text{ kPa}$$

Assume pressure and Mach number prior to the shock is equal to analytical calculations as

$$p_2 = 3.26 \text{ kPa}$$

$$M_2 = 4.30$$

Re-arranging Equation 2.6 to find the normal Mach number prior to the shock as

$$M_{n_2} = \sqrt{\frac{(P_3/P_2)(\gamma+1)-\gamma+1}{\gamma+1}} = \sqrt{\frac{(4.57/3.26)(1.4+1)-1.4+1}{1.4+1}} = 1.11$$

Re-arranging Equation 2.10, the shock angle is found as follows

$$\beta_2 = \sin^{-1} \left(\frac{M_{n_2}}{M_2} \right) = \sin^{-1} \left(\frac{1.11}{4.30} \right) = 15.0^\circ$$

This result confirms that the generation of the shock wave results in the additional pressure obtained in simulation results.

The difference in pressure at data point 7 between the numerical, experimental, and the analytical results should also be noted. Referring to Figure 9.6, data location 7 is near the rear of the recirculation region. At this point, a slight reduction of pressure is observed in the experiments and the simulations due to an expansion wave created by turning the supersonic flow from the ramp into the isolator. The effect is more complicated than that due to a simple expansion fan because of the presence of the recirculation zone. The analytical result at location 7 differs substantially from both the experiments and the simulation because it assumes ideal shock-on-lip conditions

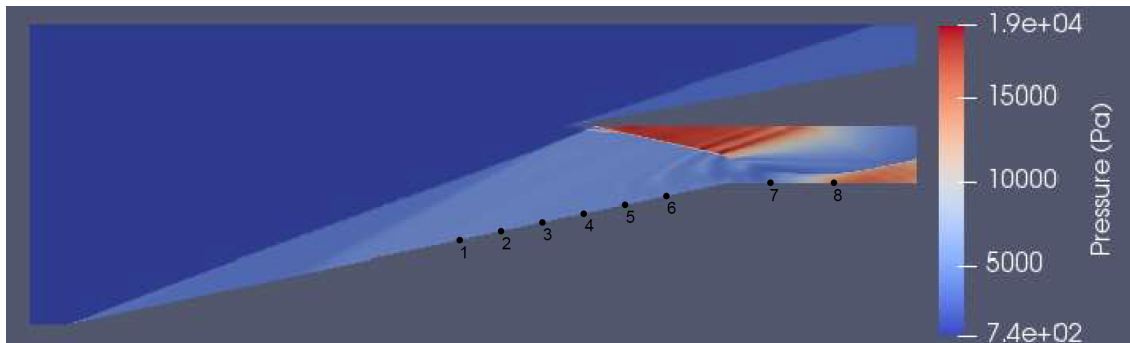
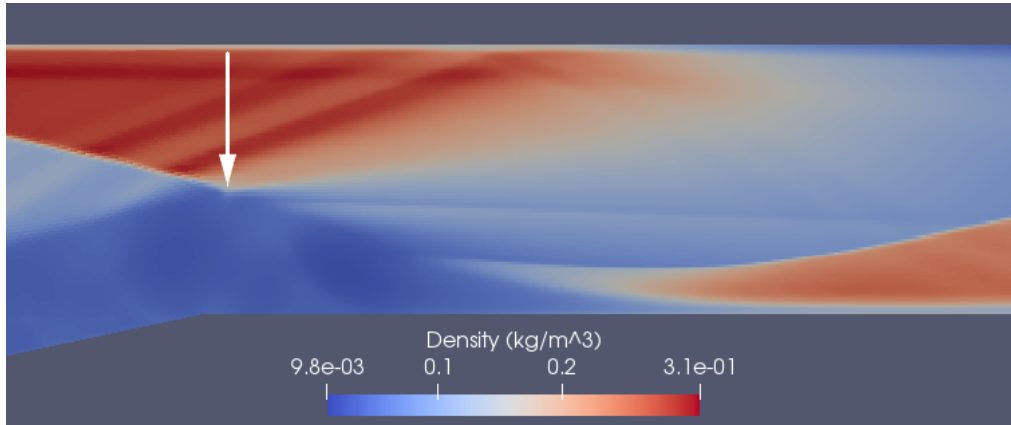
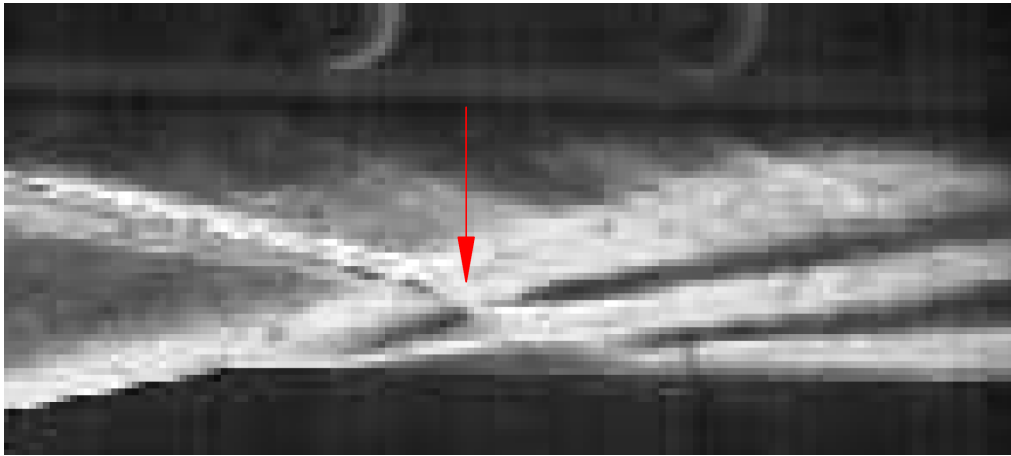


Figure 9.6: Simulated pressure contour with data locations indicated

Compared to the analytical result, the simulation result indicates a higher pressure at location 8. Referring to Figure 9.6, pressure rise is due to the reattachment shock formed at the rear of the recirculation region of which compresses air lowered in pressure from the expansion wave. As for the experimental result, the same process is occurring, however as recirculation region lies further back in the isolator, as shown in Figure 9.7, the air from the separation region is still under recompression, thus resulting in a lower measured pressure.



(a) Simulation



(b) Experimental

Figure 9.7: Comparison of simulation and experimental separation region location within the isolator - arrow indicates central location of the separation region

9.4 Conclusion of Results

The main factor leading to differences between the numerical and experimental results is due to inaccurate modelling of the flow. In experimental conditions, the boundary layer along the ramp would have been at least transitional if not fully turbulent, thus resulting in reduced separation from the swbli. In the simulation however, the boundary layer was modelled to be laminar, leading to increased separation. Using turbulence in the simulation would have produced a more realistic flow. However, the addition of turbulence comes at a great computational cost requiring longer simulation run times.

An additional factor causing a difference in the simulation and experimental results may be due to the presence of side walls on the experimental model. Side walls introduce 3D effects which alter the flow with the development of boundary layers and generate weak waves entering the isolator.

Despite the differences between the results, strong similarities are observed with both the numerical and experimental tests. This suggests that the proposed restart mechanisms should be subjected to a fair assessment when experimental testing proceeds that an unstart is able to be produced similar to that seen in numerical results. This may require a greater flow blockage to cause the required unstart than determined through the computational results because the boundary layer will not as readily separate as occurs in the simulation results.

Chapter 10

Conclusions and Further Work

Contents

10.1 Review of Thesis	100
10.2 Key Findings/Outcomes	101
10.3 Recommendations for Further Work	103

10.1 Review of Thesis

The motivation behind this research was to investigate potential methods of active re-starting that could be realistically applied to scramjet inlets in hypersonic flight. More specifically, the aim was to develop and demonstrate a scramjet inlet at Mach 5.85 which was able to self-start, but when a deliberate unstart was applied the inlet would remain in the unstarted state even after removal of the unstart source. After this, the restart mechanism would be activated, restarting the inlet.

Chapter 1 provided a brief introduction to hypersonic propulsion along with aims of the thesis. Research significance was outlined referencing unstart failures of past supersonic and hypersonic engines such as the SR-71 Blackbird turbo-ramjet engine (Graham 1996)

and X51-A scramjet engine (Li et al. 2018). Background knowledge pertaining to the research was reviewed in Chapter 2. In particular, focus was given to the scramjet operation, hypersonic inlet design parameters and the process of unstart due to thermal choking. Hypersonic flow fundamentals were also addressed along with review of shock interaction and reflections and various hypersonic viscous interactions. Chapter 3 reviewed current work performed in the area of unstart prevention and restart mechanisms. Literature surveyed showed a lack of experimental verification of the proposed restart mechanisms which have been numerically simulated. It was further noted that many unstart prevention mechanisms have the potential to also be applied as restart mechanisms forming the basis for the restart mechanisms to be tested in this work. Geometric design of the inlet along with estimates of the required injection parameters was described in Chapter 4. The inlet was designed using hypersonic theory introduced in Chapter 2. Chapter 5 described the numerical methodology and the restart mechanisms to be tested along with assessment of injection parameters to induce a sustained unstarted inlet. The chapter also describes the CFD hypersonic flow solver used, grid definitions, boundary conditions, sequence of simulations and mesh independence study to be conducted. Numerical results obtained were presented in Chapter 6. The experimental setup was described in Chapter 7. The University of Southern Queensland hypersonic wind tunnel (TUSQ), schlieren visualisation setup and pressure transducers used and the experimental model were also introduced. Chapter 8 presented experimental results and the data presented including schlieren visualisation images, tunnel test section and barrel pressures and ramp pressure measurements. Comparison of analytical, numerical and experimental results was presented in Chapter 9, including analysis of boundary layer thickness correlation, oblique shock wave angle measurement and inlet ramp pressure measurement.

10.2 Key Findings/Outcomes

Analytical design of the inlet using relevant background information was successful from the numerical and experimental results. It was demonstrated that the inlet was able to self-start, achieving near shock-on-lip conditions.

Numerical analysis showed there is a possibility of inlet restarting using slot suction at the inlet throat to remove low momentum air induced by an unstart. The suction restart mechanism using a low pressure of 200 Pa and took approximately 7 ms of activation in order to restart the inlet. Further to this, a restart mechanism using a transverse sonic injection at the inlet ramp tip was also effective in restarting the inlet. The transverse injection caused flow spillage over the inlet due to a large bow shock and when the injection was removed, a large impulse of compressed air entered into the inlet, adding momentum to the unstarted flow. The most effective injection time for inlet restarting found to be a 100 μ s burst of air. A potential restart method using mid-ramp sonic injection, using various injection angles, in an attempt to add momentum to the thick boundary layer in order to reduce its thickness, was also investigated. However, the mass flow rate from the injection was not high enough to re-accelerate the separated flow and restart the inlet.

Experiments were conducted using a model of the inlet and schlieren visualisation and inlet ramp pressure measurements were acquired with the inlet in a self-started mode of operation. Comparing the analytical, numerical and experimental data highlighted some differences in the results. The primary reason for the differences was the modelling of the boundary layer flow in the numerical simulations which treated the boundary layer as perfectly laminar. However, this is a questionable assumption, particularly because the separated flow region located in the inlet throat is likely to generate at the least transitional, if not fully turbulent flow adjacent to the wall.

It appears likely that the boundary layer transitioned to turbulent in the experimental case, so the boundary layer on the inlet ramp did not separate as readily as seen in the simulation results. In turn, an additional separation shock was formed in the simulated inlet causing a second compression past the leading edge shock which was not observed experimentally. Furthermore, the recirculation region in the simulated results moved forward due to the additional boundary layer growth, causing the simulated pressure at the rear of the isolator to vary from the experimental results.

10.3 Recommendations for Further Work

Based on the above key findings, the most promising avenues for further research are:

1. Verify the effectiveness of the restart mechanisms through experimental testing.
2. Development of a numerical model with a turbulent or transitional boundary layer to achieve boundary layer thicknesses observed in experiments. Once a closer match to the experimentally observed thickness is achieved, re-testing of the proposed restart mechanisms is recommended.
3. Further exploration of the tip restarting mechanism varying its injection pressure, speed, direction and smaller slot widths.
4. Testing of the suction restart mechanism at higher suction flows and locations along the inlet throat and potentially along the ramp.
5. Develop a coupled tip injection and throat suction restarting mechanism aiming to reduce the time required to restart the inlet.

Bibliography

- Anderson, J. D. (1989), *Hypersonic and High Temperature Gas Dynamics*, McGraw-Hill series in aeronautical and aerospace engineering, McGraw-Hill Education (ISE Editions).
- Anderson, J. D. (1990), *Modern compressible flow: with historical perspective*, Vol. 12, McGraw-Hill New York.
- Anderson, J. D. (2010), *Fundamentals of aerodynamics*, Vol. 116, Cambridge University Press (CUP).
- Andreadis, D. (2004), 'Scramjet engines enabling the seamless integration of air & space operations', *The Industrial Physicist* pp. 16–19.
- Birch, B., Buttsworth, D., Choudhury, R. & Stern, N. (2018), Characterization of a ludwig tube with free piston compression heating in Mach 6 configuration, in '22nd AIAA International Space Planes and Hypersonics Systems and Technologies Conference', American Institute of Aeronautics and Astronautics, p. 5266.
- Buttsworth, D. & Smart, M. (2010), Development of a ludwig tube with free piston compression heating for scramjet inlet starting experiments, in '48th AIAA Aerospace Sciences Meeting Including the New Horizons Forum and Aerospace Exposition', American Institute of Aeronautics and Astronautics, p. 588.
- Cantwell, B. (1996), Fundamentals of compressible flow. AA210, Department of Aeronautics and Astronautics.

- Chang, J. & Fan, Y. (2009), 'Effects of boundary-layers bleeding on performance parameters of hypersonic inlets', *Aircraft Engineering and Aerospace Technology* **81**(3), 204–211.
- Chang, J., Fan, Y., Bao, W., Yu, D. & Shen, Y. (2019), 'Unstart margin control of hypersonic inlets', *Acta Astronautica* **66**(1-2), 78–87.
- Chang, J., Li, N., Xu, K., Bao, W. & Yu, D. (2017), 'Recent research progress on unstart mechanism, detection and control of hypersonic inlet', *Progress in Aerospace Sciences* **89**, 1–22.
- Cristofolini, A., Neretti, G., Roveda, F. & Borghi, C. A. (2012), 'Schlieren imaging in a dielectric barrier discharge actuator for airflow control', *Journal of Applied Physics* **111**(3), 033302.
- Curran, E. & Murthy, S. (2001), *Scramjet Propulsion*, Vol. 189, American Institute of Aeronautics and Astronautics.
- Curran, E. T., Heiser, W. H. & Pratt, D. T. (1996), 'Fluid phenomena in scramjet combustion systems', *Annual Review of Fluid Mechanics* **28**(1), 323–360.
- Dharavath, M., Manna, P. & Chakraborty, D. (2018), 'Computational study of transverse slot injection in supersonic flow', *Defence Science Journal* **68**(2), 121–128.
- Doerffer, P. P. & Bohning, R. (2003), 'Shock wave – boundary layer interaction control by wall ventilation', *Aerospace Science and Technology* **7**(3), 171–179.
- Flores, A., Shih, T., Davis, D. & Willis, B. (1999), Bleed of supersonic boundary-layer flow through rows of normal and inclined holes, in '35th Joint Propulsion Conference and Exhibit', American Institute of Aeronautics and Astronautics, p. 2112.
- Geerts, J. S. & Yu, K. H. (2016), 'Shock train/boundary-layer interaction in rectangular isolators', *AIAA Journal* **54**(11), 3450–3464.
- Graham, R. H. (1996), *SR-71 Revealed: The Untold Story*, Zenith Imprint.

- Hank, J., Murphy, J. & Mutzman, R. (2008), The X-51A scramjet engine flight demonstration program, *in* '15th AIAA International Space Planes and Hypersonic Systems and Technologies Conference', American Institute of Aeronautics and Astronautics.
- Heiser, W., Pratt, D., Daley, D. & Mehta, U. (1994), *Hypersonic Airbreathing Propulsion*, American Institute of Aeronautics and Astronautics, Inc.
- Jacobs, P. & Gollan, R. (2016), 'Implementation of a compressible-flow simulation code in the d programming language', *Applied Mechanics and Materials* **846**, 54–60.
- Jaiman, R. K., Loth, E. & Dutton, J. C. (2004), 'Simulations of normal shock-wave/boundary-layer interaction control using mesoflaps', *Journal of Propulsion and Power* **20**(2), 344–352.
- Li, N., Chang, J., Jiang, C., Yu, D., Bao, W., Song, Y. & Jiao, X. (2018), 'Unstart/restart hysteresis characteristics analysis of an over–under TBCC inlet caused by backpressure and splitter', *Aerospace Science and Technology* **72**(4), 418–425.
- Mahoney, J. (1990), *Inlets for Supersonic Missiles*, American Institute of Aeronautics and Astronautics, Inc.
- Mashio, S., Kurashina, K., Bamba, T., Okimoto, S. & Kaji, S. (2001), Unstart phenomenon due to thermal choke in scramjet module, *in* '10th AIAA/NAL-NASDA-ISAS International Space Planes and Hypersonic Systems and Technologies Conference', American Institute of Aeronautics and Astronautics, p. 1887.
- Matsuo, K. (2003), 'Shock train and pseudo-shock phenomena in supersonic internal flows', *Journal of Thermal Science* **12**(3), 204–208.
- Moelder, S. & Szpiro, E. J. (1966), 'Busemann inlet for hypersonic speeds.', *Journal of Spacecraft and Rockets* **3**(8), 1303–1304.
- Pasquariello, V., Grilli, M., Hickel, S. & Adams, N. A. (2014), 'Large-eddy simulation of passive shock-wave/boundary-layer interaction control', *International Journal of Heat and Fluid Flow* **49**, 116–127. 8th Symposium on Turbulence & Shear Flow Phenomena (TSFP8).

- Pritchard, P. (2010), *Fox and McDonald's Introduction to Fluid Mechanics, 8th Edition*, John Wiley & Sons.
- Rimlinger, M. J., Shih, T. I.-P. & Chyu, W. J. (1996), 'Shock-wave/boundary-layer interactions with bleed through rows of holes', *Journal of Propulsion and Power* **12**(2), 217–224.
- Rudd, L. V. & Lewis, M. J. (1998), 'Comparison of shock calculation methods', *Journal of Aircraft* **35**(4), 647–649.
- Sandham, N. (2011), *Shock Wave–Boundary-Layer Interactions*, Cambridge University Press.
- Schmidt, B. (2015), *Schlieren Visualization*, California Institute of Technology.
- Shneider, M. N., Macheret, S. O. & Miles, R. B. (2004), 'Analysis of magnetohydrodynamic control of scramjet inlets', *AIAA Journal* **42**(11), 2303–2310.
- Smith, A., Babinsky, H., Fulker, J. L. & Ashill, P. R. (2004), Shock wave/ boundary-layer interaction control using streamwise slots in transonic flows, in '11th ICTAM Symposium', Vol. 41, American Institute of Aeronautics and Astronautics (AIAA), pp. 540–546.
- Souverein, L. & Debiève, J.-F. (2010), 'Effect of air jet vortex generators on a shock wave boundary layer interaction', *Experiments in Fluids* **49**(5), 1053–1064.
- Tan, H.-J., Li, L.-G., Wen, Y.-F. & Zhang, Q.-F. (2011), 'Experimental investigation of the unstart process of a generic hypersonic inlet', *AIAA Journal* **49**(2), 279–288.
- Wie, D. V. & Molder, S. (1992), Applications of busemann inlet designs for flight at hypersonic speeds, in 'Aerospace Design Conference', American Institute of Aeronautics and Astronautics.
- Wise, D. (2015), Experimental investigation of a three dimensional scramjet engine at hypervelocity conditions, PhD thesis.

- Yuan, H.-c. & Liang, D.-w. (2006), 'Analysis of characteristics of restart performance for a hypersonic inlet', *Journal of Propulsion Technology* **27**(5), 390.

Appendix

Appendix A - Project Specification

ENG 4111/2 Research Project

Project Specification

For: **Lachlan Noller**

Topic: Investigation of active air injection flow control to Restart a 2D Hypersonic Inlet at Mach 6

Supervisors: Prof. David Buttsworth
Dr. Fabian Zander

Sponsorship: Faculty of Health, Engineering & Sciences

Project Aim: This project is focused to develop a new method of restarting a 2D internal-external single ramp scramjet inlet configuration at a nominal flow speed of Mach 6 with unstart occurring due to a combination SWBLI's and high isolator backpressures simulating pressures due to combustion. Pressure transducers and Schlieren visualisations will gather numerical and visual measurements respectively from the experimental model to determine the effect of the restart mechanism, identifying the magnitude of the separation bubble size and assess whether the inlet has restarted. The proposed restart control mechanism will be air injection upstream of the inlet throat going into the boundary layer as a means of momentum addition, attempting to reduce the separation bubble size. Numerical methods will include a simulation produced using Eilmer4 of the model to replicate the experimental model and restart mechanism to serve as a comparison.

Program:

1. Research background information on hypersonic flow theory, swept oblique shock analysis and shock wave/ boundary-layer interactions.
2. Review scramjet fundamental operation, specific inlet and isolator flow character-

istics, unstart, and currently explored methods of unstart prevention and restarting mechanisms.

3. Perform analytical calculations to develop scramjet geometry, unstarting injection and restarting injection parameters respective to flow conditions.
4. Design experimental model with ramp pressure transducers along with cross-sectional view ports for Schlieren visualisation.
5. Develop numerical simulation of model using Eilmer4, taking pressure measurements along with visual observations.
6. Perform experiment in TUSQ hypersonic wind tunnel taking ramp pressure measurements and Schlieren visualisation observations.
7. Compare experimental, analytical and numerical results using MATLAB.

As time and resources permit:

1. Explore use of secondary active control, possibly suction of the recirculation zone, to remove low momentum boundary layer.
2. Introduce particles into the injection flow as means of additional momentum addition

Agreed:

Student Name: Lachlan Noller

Date: 16/11/2018

1st Supervisor Name: Prof. David Buttsworth

2nd Supervisor Name: Dr. Fabian Zander

Date: 16/11/2018

Appendix B - Project Requirements

ENG 4111/2 Research Project

Project Resources

Requirements:

1. The student will require adequate access to a personal computer, already within possession. This will be used for literature review research, document processing, and basic analysis of results.
2. The student requires access to a computer running Linux software for the use of Eilmer4 for running initial simulations. This is facilitated over at one of the computers in P10.
3. To perform final simulations of the model, access to use the TUSQ high performance computer (HPC) is required. Appropriate training for use will be done, facilitated by supervisor.
4. Organisation with TUSQ Engineering workshop staff is required to manufacture required model parts. Funding to pay for these parts will also need to be organised.
5. Access to the TUSQ epoxy 3D printer is needed for the production of the final ramp component with precise internal injection geometry.
6. Enough time to test the experimental model in the TUSQ Hypersonic Wind Tunnel will also be required with access to be organised by supervisor.

Appendix C - Project Plan

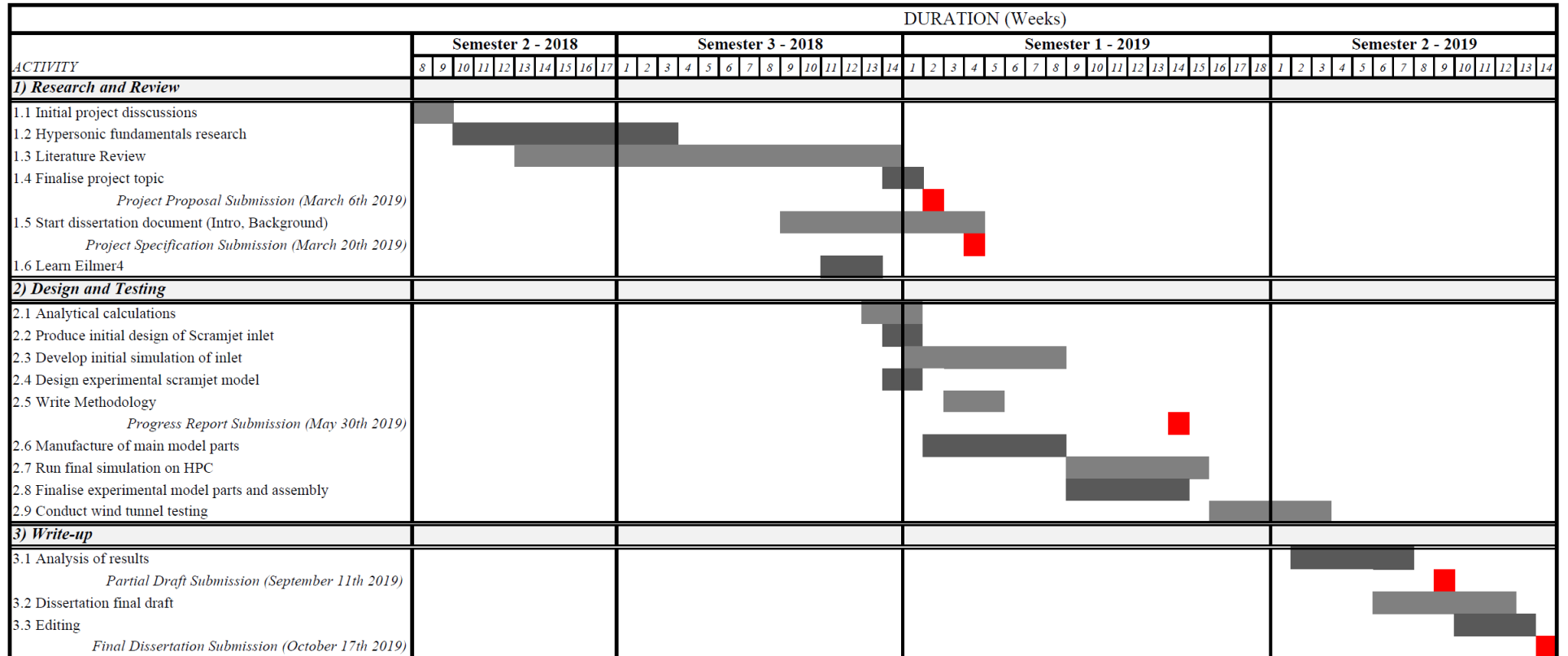


Figure C.1: Project Plan

Appendix D - Risk Assessment

Using a risk assessment matrix, the risks involved in the research are identified. Generally used within industry, the risk assessment matrix ensures potential hazards are minimised as much as reasonable. Figure D.1 identifies the likelihood of the event occurring along with the occurring potential consequences. Each identified risk is assessed and placed into the appropriate category. Any risk higher than low should have appropriate measures to ensure that it is minimised. Table 10.1 notes the final risks involved with the proposed research.

			Consequences				
			1 – Insignificant Dealt with by in-house first aid, etc	2 – Minor Medical help needed. Treatment by medical professional/hospital outpatient, etc	3 – Moderate Significant non-permanent injury. Overnight hospitalisation (inpatient)	4 – Major Extensive permanent injury (eg loss of finger/s) Extended hospitalisation	5 – Catastrophic Death. Permanent disabling injury (eg blindness, loss of hand/s, quadriplegia)
Likelihood	A	Almost certain to occur in most circumstances	High (H)	High (H)	Extreme (X)	Extreme (X)	Extreme (X)
	B	Likely to occur frequently	Moderate (M)	High (H)	High (H)	Extreme (X)	Extreme (X)
	C	Possible and likely to occur at some time	Low (L)	Moderate (M)	High (H)	Extreme (X)	Extreme (X)
	D	Unlikely to occur but could happen	Low (L)	Low (L)	Moderate (M)	High (H)	Extreme (X)
	E	May occur but only in rare and exceptional circumstances	Low (L)	Low (L)	Moderate (M)	High (H)	High (H)

Figure D.1: Risk Assessment Matrix

Table 10.1: Risk Assessment

Activity: Testing of Scramjet Inlet with restart control in TUSQ Wind Tunnel		Completed By: Lachlan Noller	
Identified Risks	Current Control Measures	Level of Risk	Actions Required
Working around pressurised air: Pressurised air may cause particles blown into the eyes of the operator and surrounding people. There is also potential for hearing damage when connection and disconnection the air hose. (Note No air gun is used)	<ul style="list-style-type: none"> - Ensure fittings are not pointed at operators face - Gradual release of air when initial bench top testing is taking place - Operator does not leave test piece until the air is completely discharged. 	D2 – Low Risk	No further actions required
Moving Parts: Working around moving parts there is a potential pinching and crushing risk.	<ul style="list-style-type: none"> - All moving parts are underneath the test piece and are not easily assessable. To make this more so when bench top testing occurs the test piece is kept low relative to the bench. - When testing occurs hands and other equipment are kept away from the area at all times. - When the test is complete air is disconnected (air is the actuation method) before adjusting parts 	E1 – Low Risk	No further actions required
Sharp edges/ points: The scramjet model has many sharp points and edges that could potentially cut the operator.	<ul style="list-style-type: none"> - The point at the tip of the inlet always has a section of rubber hose over it to keep the tip out of the way. - Once assembled the sharp leading edge of the two guide plates are almost inaccessible and it almost runs flush with the inlet taking away the potential to slice across it. - Only operated by people who are aware of the edges and know how the test piece works. 	D2 – Low Risk	No further actions required
Electrical hazard when operating solenoid and power supply: There is the potential of an electric shock when operating the power supply and solenoid	<ul style="list-style-type: none"> - Make sure power supply, wires and solenoid are kept away from water - Make sure power supply is turned off as soon as test is complete. - Solenoid is powered by 12 V so this is a low voltage application. 	E1 - Low Risk	No further actions required
Soldering: Risk of burns	<ul style="list-style-type: none"> - Eye protection worn - Stands used to prevent fingers getting too close to work 	D1 – Low Risk	No further actions required

Appendix E - MATLAB Code

E.1 Scramjet Inlet Geometry Calculations

9/25/19 8:29 AM C:\...\SCRAMJET GEOMETRY CALCS LaTeX.m 1 of 4

```
%% SCRAMJET INLET GEOMETRY CALCULATIONS

% The following code calculates a 2D, single ramp, dual shock
% scramjet inlet geometric dimensions to the Kantrowitz
% contraction limit. Moreover, calculations are made to
% determine the displacement thickness of the compressible
% boundary layer along the main ramp.

% Written by: Lachlan J Noller
% Date written: 21/1/2019

clear
clc
close all
%% CONSTANTS
% Ideal Gas Constant
R = 287;
% Air ratio of specific heats
gamma = 1.4;
% Free Stream Mach No.
M_1 = 5.85;
% First Compression Ramp Turning Angle (Degrees)
Theta_1 = 12;
% Second Compression Ramp Turning Angle (Degrees)
Theta_2 = Theta_1;
% Free Stream Pressure (Pa)
P_1 = 740;
% Free Stream Temperature (K)
T_1 = 73;
% Capture Height (m)
h_c = 0.15;
% Free Stream Density (kg/m^3)
rho_1 = P_1 / (R * T_1);
% Isolator height (m)
i_h = 0.01;
% Cowl Angle (degrees)
c_deg = 10;
% Isolator length (m)
i_L = 0.05;
% Isolator Height (m)
h_4 = 0.01;

%% 1ST SHOCK CALCS
Beta_1 = beta(M_1,Theta_1,gamma,0);
M_n1 = M_1*sind(Beta_1);
P_2 = ((2 * gamma * (M_n1^2) - gamma + 1) / (gamma + 1)) * P_1;
rho_2 = (((gamma + 1) * M_n1^2)/(2 + (gamma - 1) * M_n1^2)) ...
    * rho_1;
T_2 = P_2 / (R * rho_2);
M_n2 = ((1+(gamma - 1)/2*M_n1^2)/...
    (gamma*M_n1^2 - ((gamma - 1)/2)))^0.5;
M_2 = M_n2 / sind(Beta_1 - Theta_1);
```

9/25/19 8:29 AM C:\...\SCRAMJET GEOMETRY CALCS LaTeX.m 2 of 4

```

%% 2ND SHOCK CALCS
Beta_2 = rad2deg(asin(1/M_2));
M_n2 = M_2*sind(beta(M_2,Theta_1,gamma,0));
P_3 = (2 * gamma * M_n2^2 - gamma + 1)/(gamma + 1) * P_2;
rho_3 = ((gamma + 1) * M_n2^2)/(2 + (gamma - 1) * M_n2^2) * rho_2;
T_3 = P_3 / (R * rho_3);
M_n3 = ((1+(gamma - 1)/2*M_n2^2)/(gamma*M_n2^2 - ((gamma - 1)/2)))^0.5;
M_3 = M_n3 / sind(beta(M_2,Theta_1,gamma,0) - Theta_2);

%% KANTROWITZ LIMIT
KL = (1/M_2)*(((gamma + 1)*M_2^2)/((gamma - 1)*M_2^2 + 2)) ...
    ^((gamma)/(gamma - 1))*((gamma + 1)/ ...
    (2*gamma*M_2^2 - (gamma - 1)))^(1/(gamma - 1)) * ...
    ((1+((gamma-1)/2)*M_2^2)/((gamma + 1)/2)) ...
    ^((gamma + 1)/(2*(gamma - 1)));

%% DISPLAYING RESULTS

T = table([P_1;P_2;P_3],[rho_1;rho_2;rho_3],[T_1;T_2;T_3],[M_1;M_2;M_3], ...
    'VariableNames',...
    {'Pressure_Pa','Density_kg_m_3','Temperature_K','Mach_No'},...
    'RowNames',{'Free Stream','First Shock','Second Shock'})

%% INLET GEOMETRY
m_1 = tand(Beta_1);
m_2 = -tand(Beta_2);
m_4 = tand(Theta_1);

R_H = m_1*((i_h - (m_4*i_h)/m_2)/(m_1 - m_4)) - i_h;
R_L = R_H/m_4;
C_L = i_h/tan(degtorad(Beta_2)) + i_L;
C_H = R_H + i_h;
CR = (i_h - ((m_4*i_h)/m_2))/(i_h);

% Pressure transducer locations
L_t = 0.10792;
L_i = 0.17422;

x0 = L_t*cosd(Theta_1); y0 = L_t*sind(Theta_1);
x1 = (L_t+0.012)*cosd(Theta_1); y1 = (L_t+0.012)*sind(Theta_1);
x2 = (L_t+0.022)*cosd(Theta_1); y2 = (L_t+0.022)*sind(Theta_1);
x3 = (L_t+0.032)*cosd(Theta_1); y3 = (L_t+0.032)*sind(Theta_1);
x4 = (L_t+0.042)*cosd(Theta_1); y4 = (L_t+0.042)*sind(Theta_1);
x5 = (L_t+0.052)*cosd(Theta_1); y5 = (L_t+0.052)*sind(Theta_1);
x6 = L_i*cosd(Theta_1) + 0.01; y6 = R_H;
x7 = x6 + 0.015; y7 = R_H;

xn = [x0,x1,x2,x3,x4,x5,x6,x7];
yn = [y0,y1,y2,y3,y4,y5,y6,y7];

%% GRAPH
figure(1)
axis image

```

9/25/19 8:29 AM C:\...\SCRAMJET GEOMETRY CALCS LaTeX.m 3 of 4

```

grid on
title('Ideal Inlet Geometry')
x = [0 R_L]; y = [0 R_H];
a = line('Xdata',x,'Ydata',y,'linewidth',1.0);

x = [R_L (R_L + i_L)];
y = [R_H R_H];
b = line('Xdata',x,'Ydata',y,'linewidth',1.0);

x = [(R_L + i_L - C_L) (R_L + i_L)];
y = [C_H C_H];
c = line('Xdata',x,'Ydata',y,'linewidth',1.0);

x = [(R_L + i_L - C_L) (R_L + i_L)];
y = [C_H (C_L * tan(deg2rad(c_deg)) + C_H)];
d = line('Xdata',x,'Ydata',y,'linewidth',1.0);

x = [0 (R_L + i_L - C_L)];
y = [0 C_H];
e = line('Xdata',x,'Ydata',y,'Color','red','LineStyle','--','linewidth',1.0);

x = [(R_L + i_L - C_L) R_L];
y = [C_H R_H];
f = line('Xdata',x,'Ydata',y,'Color','red','LineStyle','--','linewidth',1.0);

x = [0 (R_L + i_L)];
y = [0 0];
g = line('Xdata',x,'Ydata',y,'linewidth',1.0);

hold on
pn = plot(xn,yn,'x','linewidth',1.0);

hleg = legend([a e pn]...
    , 'Wall Boundaries'...
    , 'Shock Waves','Pressure Transducers','Location','northwest');
htitle = get(hleg,'Title');
set(htitle,'String','Legend')
xlabel('x (m)')
ylabel('y (m)')
saveas(gcf,'scramjet.png')
matlab2tikz('scramjet.tex')

%% Displacement Thickness
% Equations from Fundamentals of Compressible Flow by Cantwell

% Length of Plate(m)
L = sqrt(R_H^2 + R_L^2);
% Location along Plate (m)
x = [10e-3:10e-3:L];
% free stream velocity (m/s)
v_2 = M_2*sqrt(gamma*R*T_2);
% free stream Dynamic viscosity
mu_2 = viscosity(T_2,'air','keyes');
```

9/25/19 8:29 AM C:\...\SCRAMJET GEOMETRY CALCS LaTeX.m 4 of 4

```
% free stream Reynolds number
Re_2 = (rho_2*v_2*L)/mu_2;
% Spatial similarity variable at maximum boundary layer thickness
alpha = 3.469+1.67912*((gamma-1)/2)*M_2^2;
% Maximum Displacement Thickness
dis_ys = alpha./sqrt((rho_2.*v_2)./(2.*mu_2.*L));
```

E.2 Oblique Shock Wave Angle Function

9/25/19 8:46 AM C:\Users\lachl\Dropbox\FINAL...\beta.m 1 of 1

```
% This function returns the oblique shock wave angle (beta)
% for a given deflection angle (theta) in degrees and ratio
% of specific heats (gamma) and Mach number M. Specify 0
% for the weak oblique shock or 1 for the strong shock.

% Syntax:
% beta(M,theta,gamma,n)
% - where n specifies weak or strong shock returned
%
% NOTE: Angles supplied and returned from this function are
% in DEGREES.
%
% Written by: Lachlan Noller on 6/12/2018

function Beta=beta(M,theta,gamma,n)

theta=theta*pi/180;           % convert to radians
mu=asin(1/M);                 % Mach wave angle
c=tan(mu)^2;
a=((gamma-1)/2+(gamma+1)*c/2)*tan(theta);
b=((gamma+1)/2+(gamma+3)*c/2)*tan(theta);
d=sqrt(4*(1-3*a*b)^3/((27*a^2*c+9*a*b-2)^2)-1);
Beta=atan((b+9*a*c)/(2*(1-3*a*b))-(d*(27*a^2*c+9*a*b-2))/(6*a*(1-3*a*b)))*tan(
(n*pi/3+1/3*atan(1/d)))*180/pi;
```

E.3 Viscosity Function

9/25/19 8:50 AM C:\Users\lachl\Dropbox...\viscosity.m 1 of 2

```
function mu=viscosity(T,gastype,law);
%
% David R Buttsworth
% October 1995
% September 2002
%
% Keyes viscosity model
% Review and Assessment of Turbulence Models for
% Hypersonic Flows: 2D/Axisymmetric Cases
% Christopher J. Roy, and Frederick G. Blottner
% AIAA 2006-713

% typical call ...
% T = [50:1:130]';
% mu_s = viscosity(T,'nitrogen','sutherland');
% mu_k = viscosity(T,'nitrogen','keyes');
% mu_sk = viscosity(T,'nitrogen','sutherland-keyes');
% plot(T,mu_s,'s',T,mu_k,'d',T,mu_sk,'rx')

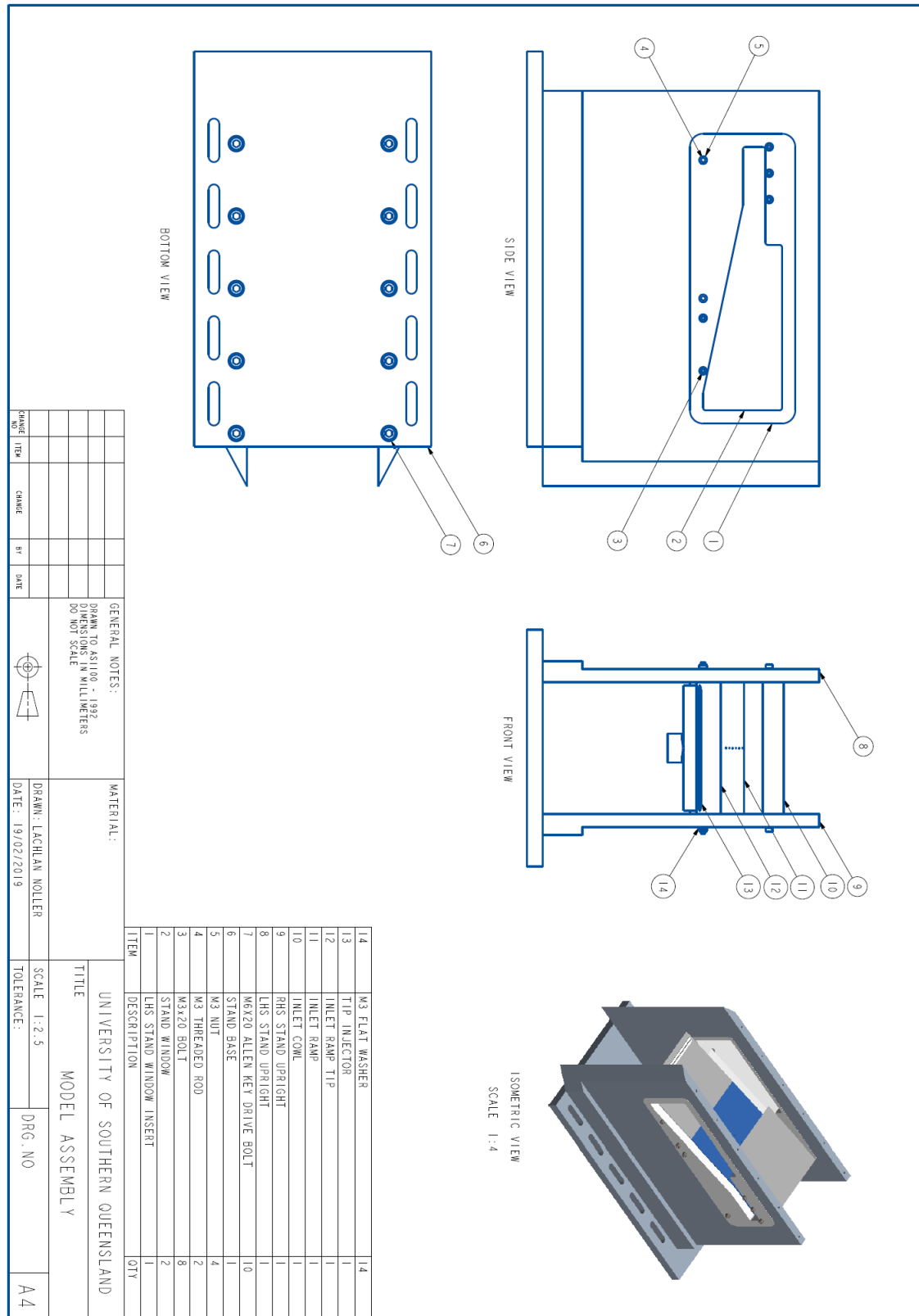
T0=273;
%
switch gastype
case 'nitrogen'
    mu0=1.663e-5; S=107; % Sutherland
    a0 = 1.418; a1 = 116.4; a2 = 5.0; % Keyes
case 'oxygen'
    mu0=1.919e-5; S=139;
    a0 = NaN; a1 = NaN; a2 = NaN; % Keyes -- not yet defined
case 'hydrogen'
    mu0=8.411e-6; S=97;
    a0 = NaN; a1 = NaN; a2 = NaN; % Keyes -- not yet defined
case 'air'
    mu0=1.716e-5; S=111;
    a0 = 1.488; a1 = 122.1; a2 = 5.0; % Keyes
end

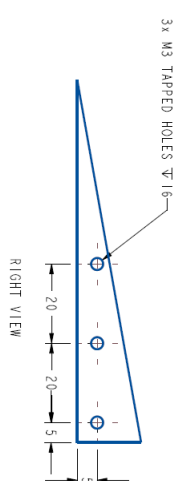
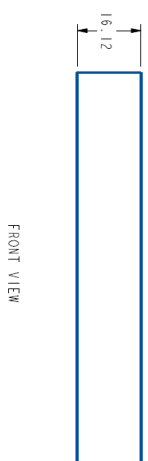
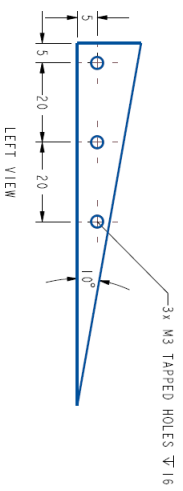
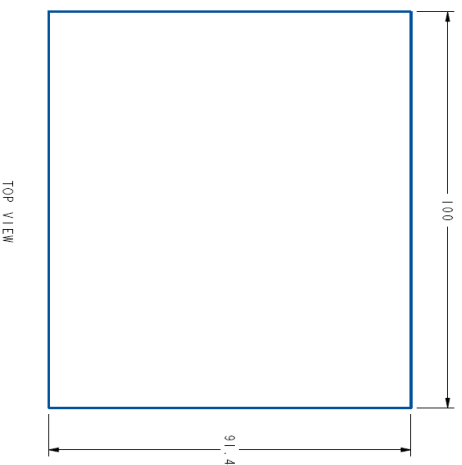
mu_sutherland = mu0*(T/T0).^1.5*(T0+S)./(T+S);
mu_keyes = a0*1e-6*sqrt(T)./(1+a1*(10.^(-a2./T))./T);

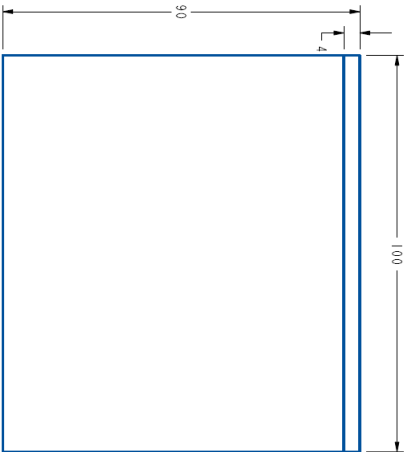
switch law
case 'sutherland'
    mu = mu_sutherland;
case 'keyes'
    mu = mu_keyes;
case 'sutherland-keyes'
    % https://www.grc.nasa.gov/www/winddocs/user/keywords/viscosity.html
    % linear transition between 160 degR and 180 degR
    % K = R*5/9 --> 160*5/9 degR = 88.8889 K
    %          180*5/9 = 100 K
    f = (T-88.8889)/(100-88.8889);
    mu_transition = f.*mu_sutherland + (1-f).*mu_keyes;
    N_sutherland = find(T >= 100);
```

```
N_keyes = find(T <= 88.8889);  
mu = mu_transition;  
mu(N_sutherland) = mu_sutherland(N_sutherland);  
mu(N_keyes) = mu_keyes(N_keyes);  
%figure(2)  
%plot(T,mu_transition)  
end
```

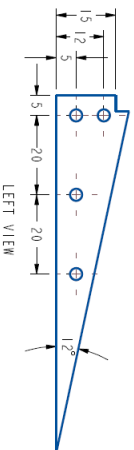

Appendix F - Model Drawings



[illegible]



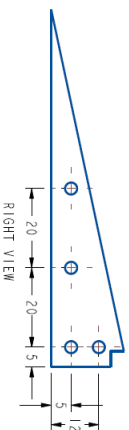
TOP VIEW




LEFT VIEW

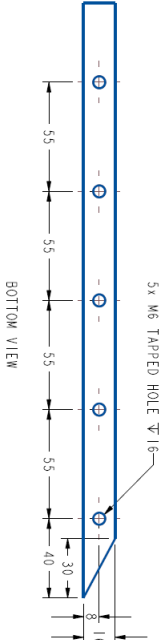
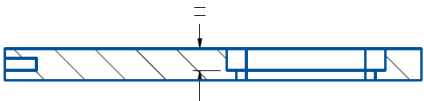
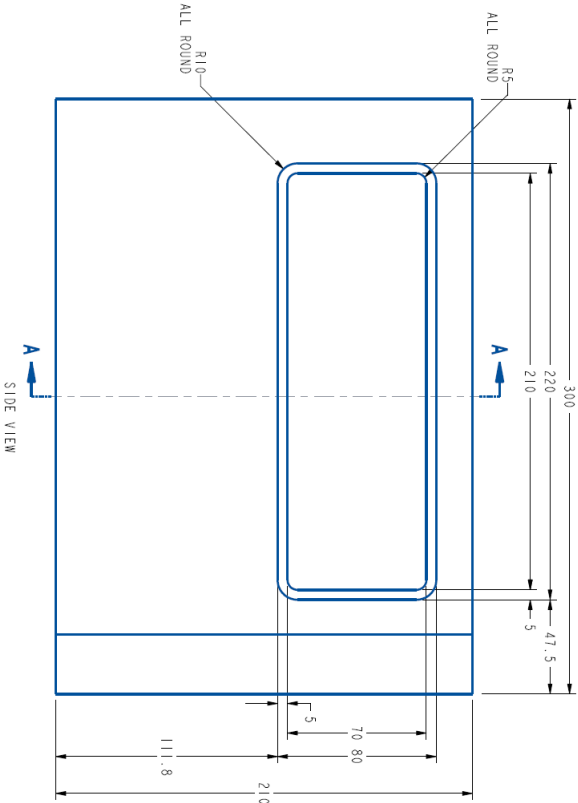


FRONT VIEW

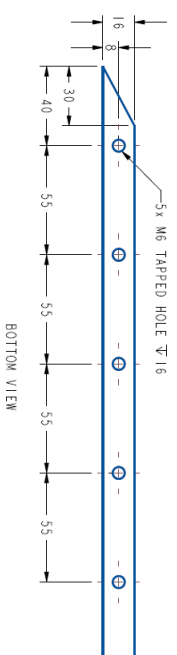
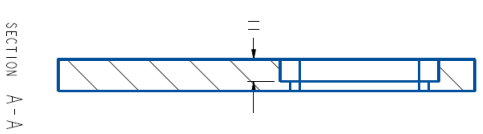
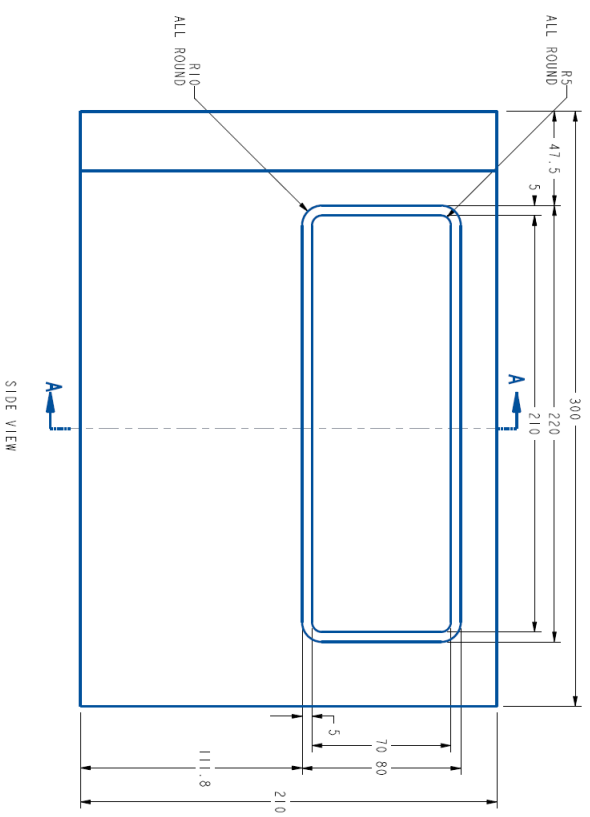


RIGHT VIEW

		GENERAL NOTES:		MATERIAL:		UNIVERSITY OF SOUTHERN QUEENSLAND	
		DRAWN TO AS1100 - 1992				TITLE	
		DIMENSIONS IN MILLIMETERS				INLET RAMP TIP	
		DO NOT SCALE				TOLERANCE:	
				DRAWN: LACHLAN NOLLER		DRG. NO	
				DATE: 20/02/2019		A4	



GENERAL NOTES:				MATERIAL:				UNIVERSITY OF SOUTHERN QUEENSLAND			
DRAWN TO AS1100 - 1992								TITLE			
DIMENSIONS IN MILLIMETERS								LHS STAND UPRIGHT			
DO NOT SCALE								SCALE 1:2			
								TOLERANCE:			
								DRG. NO			
								A4			
CHANGE NO.	ITEM	CHANGE	BY	DATE							



		UNIVERSITY OF SOUTHERN QUEENSLAND	
		TITLE	
		RHS STAND UPRIGHT	
		DRAWN: LACHLAN NOLLER	
		DATE: 19/02/2019	
		SCALE 1:2	
		TOLERANCE:	
		DRG. NO	
		A4	
		GENERAL NOTES:	
		DRAWN TO AS1100 - 1992	
		UNLESS NOTED OTHERWISE ALL DIMENSIONS	
		DO NOT SCALE	
PARTS LIST		BY DATE	
NAME			

Appendix G - Model Modifications

G.1 Tip Injection

Upon completion of simulations, once a final restart mechanism had been established, modifications to the existing ramp component were required. From simulations, the slot Mach 1 injection is located 10 mm in the x direction from the ramp tip. A 3D printed injection plenum shown in Figure G.1 was designed which would insert through a 6 mm slot milled through the ramp tip illustrated in Figure G.2.

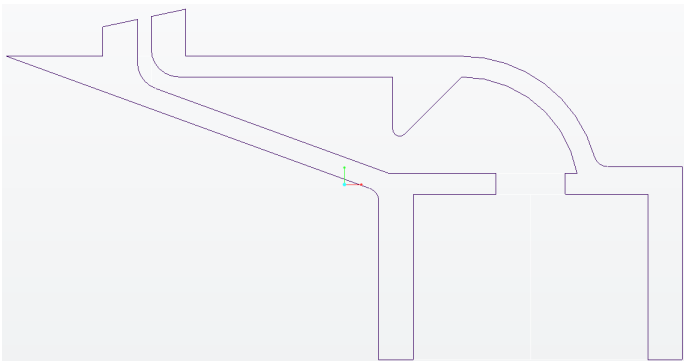


Figure G.1: Injector plenum cross-section

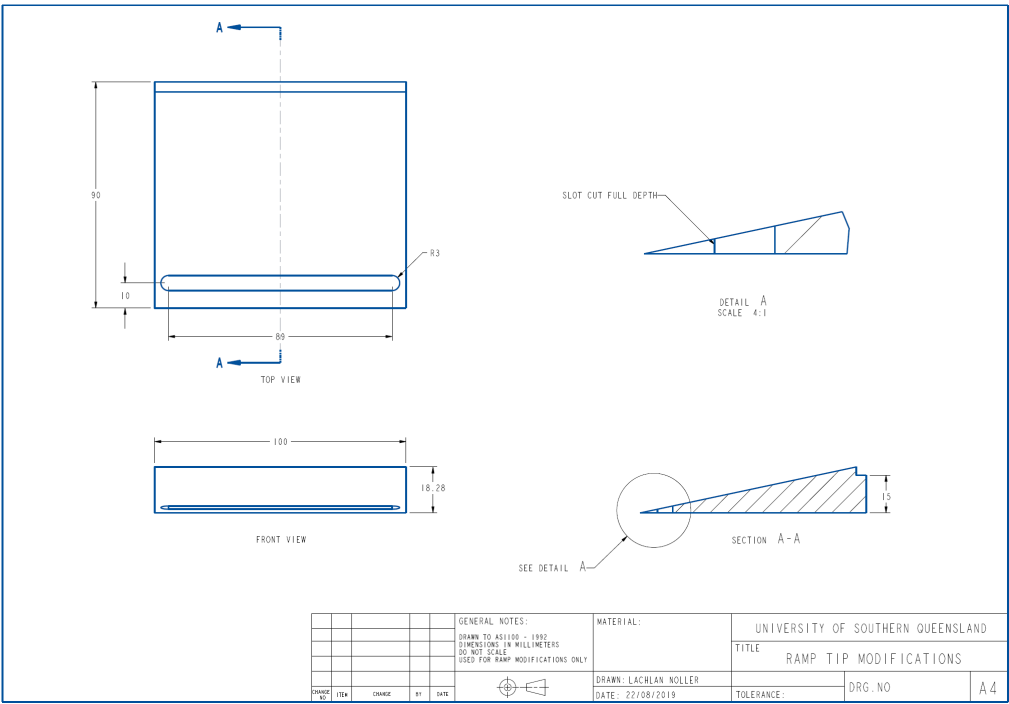


Figure G.2: Ramp tip modifications with 6 mm slot

Figures G.3 and G.4 below show the final assembled model ramp.



Figure G.3: Final ramp assembly side view

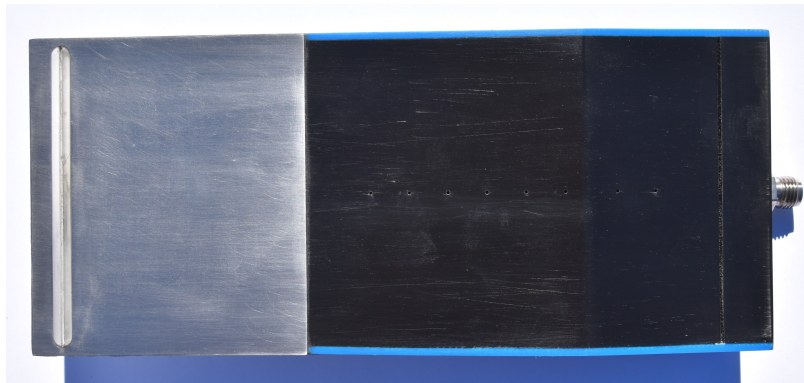


Figure G.4: Final ramp assembly side view

G.2 Side Wall Thickness

Figure G.5 below shows Schlieren visualisation result from a primary test of the inlet at 32 ms of flow duration.

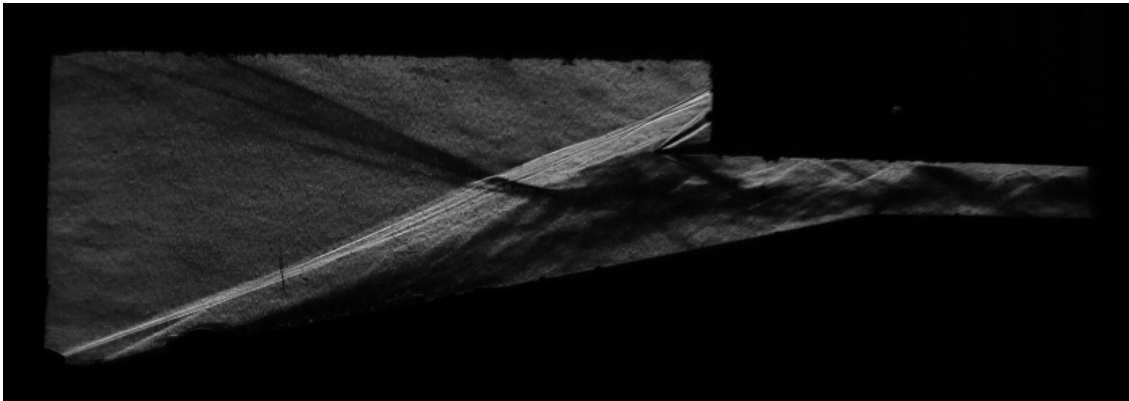


Figure G.5: Primary model test Schlieren visualisation result at 32 ms of flow duration

Due to significant blockage caused by the model, the backpressure in tunnel begins to rise. This leads to the collapse the Mach cone which drives into the inlet, disturbing its shock system. To reduce the amount of blockage produced by the model, 6 mm of material was removed from the model side walls along with a total overall height reduction (refer to Figures G.6 and G.7). It should be additionally noted that to help relieve the pressure in the isolator and reduce overall backpressure during runs, the isolator height was increased from 10 mm to 15 mm. Furthermore, a strong shock was generated at the metal tip and 3D printed ramp component interface due to poor surface finish. This would have also contributed to the blockage generated by the model.

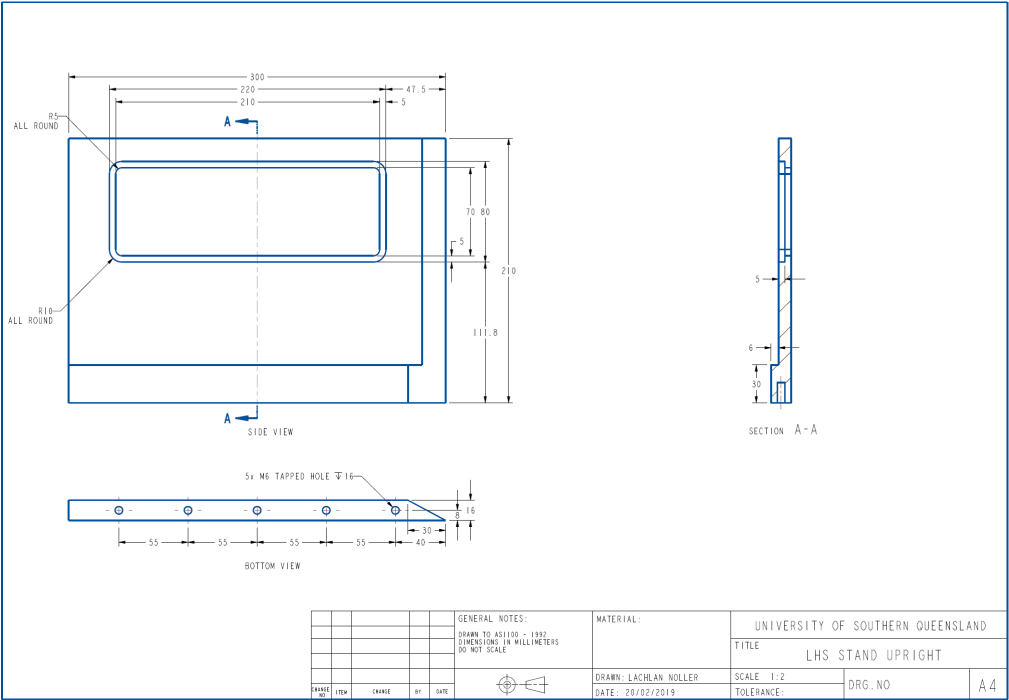


Figure G.6: Modifications made to left hand side model stand

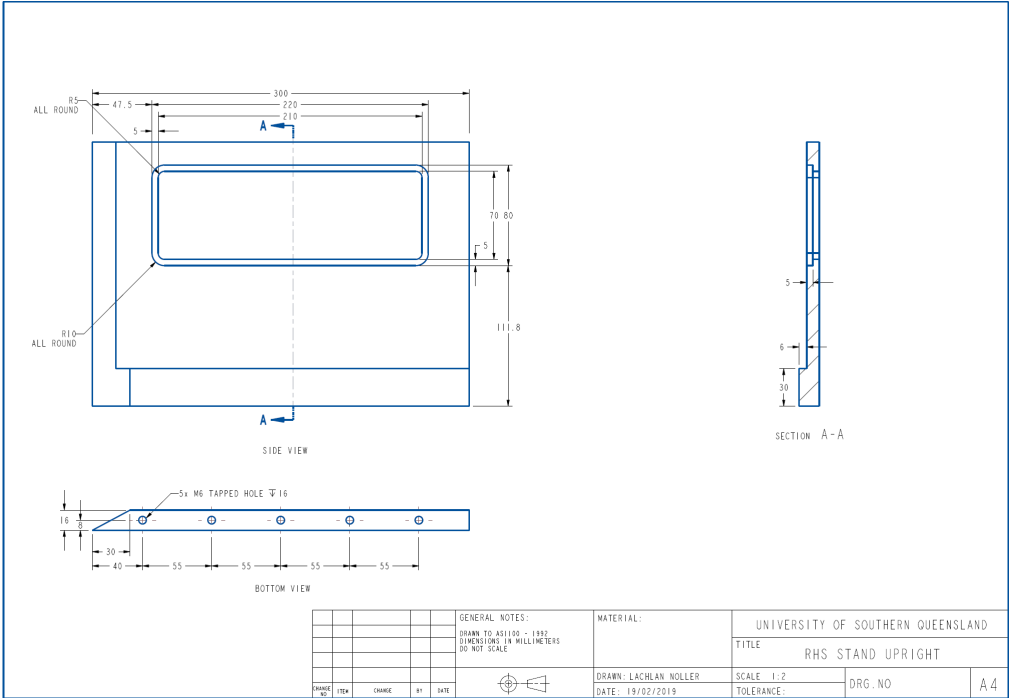


Figure G.7: Modifications made to right hand side model stand

G.3 Window Design

To allow for optical access into the inlet flow field, windows were required to be integrated to the model design. When initially designing the model, the ability to adjust the design if required was one factor leading to the use of 3D printed inserts rather than cutting one specific window profile in the steel side uprights. Three iterations of the window design were used in an attempt to find the best design. Figure G.8 shows the first window design.

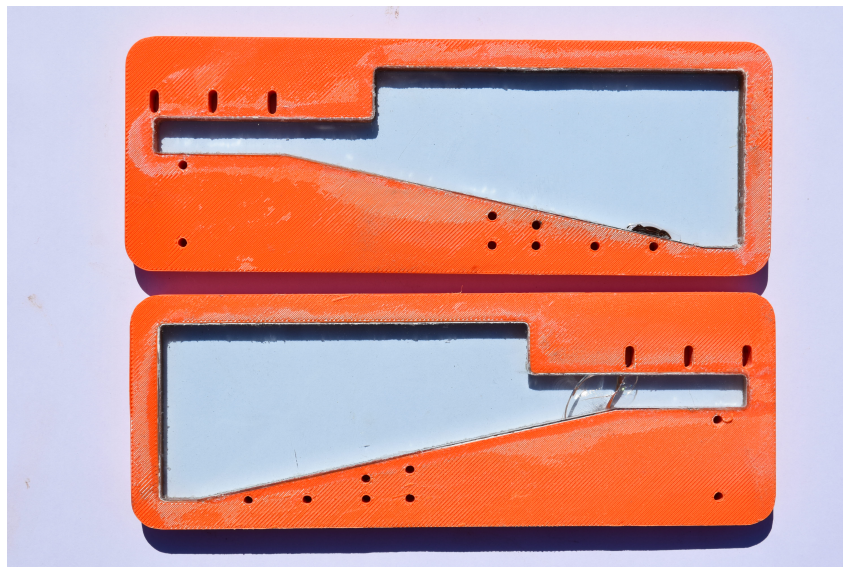


Figure G.8: First window design

This initial design uses a 3D printed insert with mounting holes for the ramp and cowl along with float glass cut to fit the inner 3D printed profile. The primary issue with this design was that due to the slotted cowl mounting holes, the cowl would move upwards during runs due to high pressure generated in the isolator. Moreover, as the glass was epoxy-glued into the 3D print, running of the glue into small cracks on the edge of the glass occurred, disrupting visualisation of the flow field. Moreover, as the 3D print compressed locally when tightened by bolts to hold the ramp and cowl, the glass would also compress leading to fracture of the glass. To resolve these issues, a second pair of windows was manufactured as illustrated in refer Figure G.9.

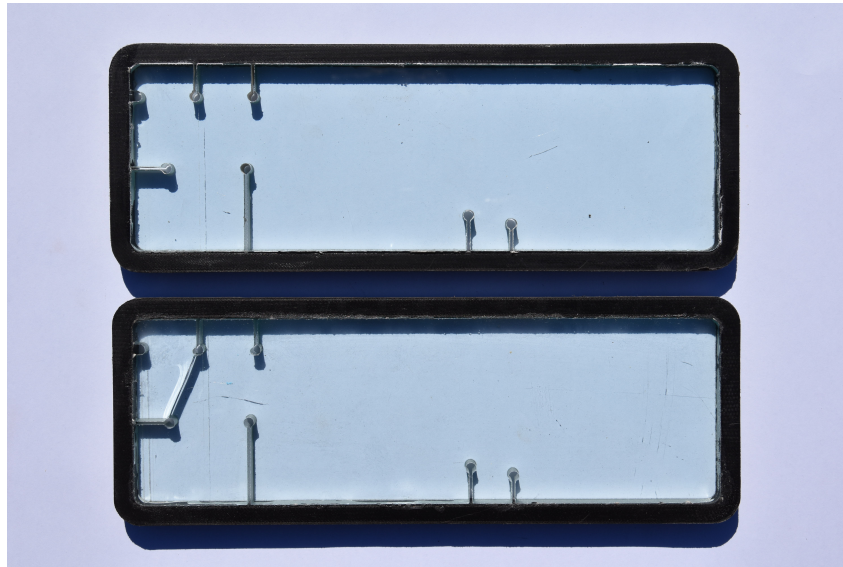


Figure G.9: Second window design

In an attempt to eliminate the possibility of glue entering the flow field, the glass windows used integrated bolting holes for the ramp and cowl components. This however made localised stress raisers which immediately fractured the glass. Returning to the initial design, the final window components are seen in Figure G.10.



Figure G.10: Final window design

This final window design was much the same as the first design with some modifications

made. Rather than the PLA 3D print used in the first iteration, onyx 3D print material was used to minimise compression that may cause glass fracture. Secondly, silicon was used as an adhesive rather than epoxy to minimise compression of the glass during assembly and operation. Finally, rather than slotted bolt holes for the cowl, round non-adjustable holes were used to set a permanent isolator height of 15 mm.

G.4 Model Roof

Due to additional blockage added with the tip injection plenum on the underside of the model, test section pressure rise occurred resulting in an increase in the Mach cone angle as shown in Figure G.11. This caused an unstart of the inlet as shown in Figure G.12.

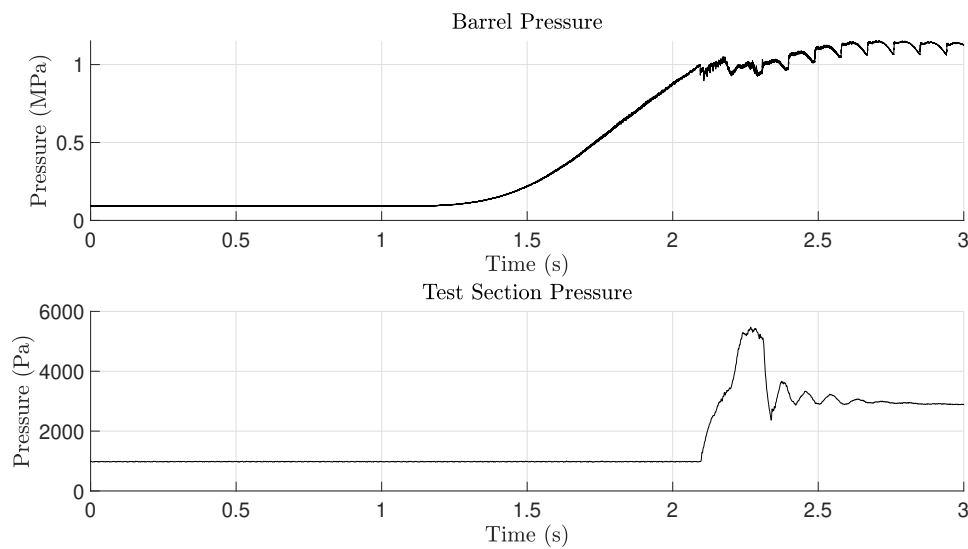


Figure G.11: Run 928 Tunnel and Barrel pressure history.

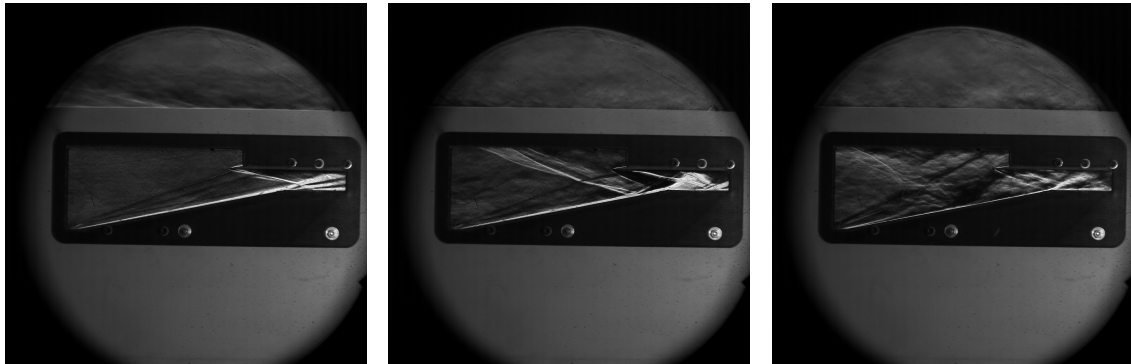


Figure G.12: Flow collapse progression from a started condition at 4 ms of flow *left* to the increasing backpressure increasing the Mach cone angle at seen at 60 ms *centre* and total unstart at 70 ms *right*.

As seen in Figure G.12, collapse of the Mach cone results in impingement of an external shock wave into the inlet shock structure. This results in shock-shock interaction occurring with the leading edge shock wave, in turn forming multiple reflected shocks in the isolator, increasing isolator pressure leading to inlet unstart as indicated in Figure G.11. To prevent this external shock impingement, the addition of a model roof was applied to protect the inlet flow field. However, this roof generated an additional shock wave which, depending on its positioning, could impinge into the inlet generated shock structure. Multiple tests were conducted to determine a roof location for which the roof shock would impinge on top of the inlet cowl rather than enter the duct.

Appendix H - Eilmer4 Input Scripts

H.1 Self-Started Inlet Script

```

1  -- 12-deg-inlet.lua
2  -- Lachlan J Noller created 18/02/2019
3  -- Model of 2D single ramp inlet with 12 degree ramp
4
5  config.title = "2D Inlet with 12 degree ramp"
6  print(config.title)
7  config.dimensions = 2
8
9  -- Flow conditions
10
11  R = 287
12  gamma = 1.4
13  M_inf = 5.85
14  p_inf = 740 -- Pa
15  T_inf = 73 -- degree K
16  u_inf = M_inf*math.sqrt(gamma*R*T_inf) -- m/s
17  T_ramp = 300 -- degree K
18
19  nsp, nmodes = setGasModel('ideal-air-gas-model.lua')
20  print("GasModel set to ideal air. nsp= ", nsp, " nmodes= ", nmodes)
21  inflow = FlowState:new{p=p_inf, velx=u_inf, T=T_inf}
22  initial = FlowState:new{p=500.0, velx=0.0, T=300.0}
23
24  -- Flow Domain
25
26  mm = 1.0e-3 -- metres per mm
27
28  -- Set measurements
29
30  L_A_B = 10*mm -- i direction inlet to flow domain
31  L_B_D = 170.4*mm -- i direction ramp length
32  L_B_E = 220*mm -- i direction total length
33  L_B_C = 128.6*mm -- i direction distance to cowl lip from origin
34  H_C = 15*mm -- j direction combustor height
35  H_E = 10*mm -- j direction addition flow above cowl
36  alpha = 12*math.pi/180.0 -- Ramp angle (radians)
37  tan_alpha = math.tan(alpha)
38  beta = 10*math.pi/180.0 -- Cowl angle (radians)
39  tan_beta = math.tan(beta)
40
41  -- Inflow points
42
43  a0 = Vector3:new{x=-L_A_B, y=0.0}
44  a1 = a0+Vector3:new{x=0.0, y=L_B_D*tan_alpha + H_C}
45  a2 = a1+Vector3:new{x=0.0, y=((L_B_E - L_B_C)*tan_beta) + H_E}
46  b0 = a0+Vector3:new{x=L_A_B, y=0.0}
47  b1 = a1+Vector3:new{x=L_A_B, y=0.0}
48  b2 = a2+Vector3:new{x=L_A_B, y=0.0}
49
50  -- Internal Entrance points
51
52  c0 = b0+Vector3:new{x=L_B_C, y=0.0}
53  c1 = Vector3:new{x=L_B_C, y=L_B_C*tan_alpha}
54  c2 = b1+Vector3:new{x=L_B_C, y=0.0}
55  c3 = b2+Vector3:new{x=L_B_C, y=0.0}
56
57  -- Inlet Throat points
58
59  d0 = Vector3:new{x=L_B_D, y=0.0}
60  d1 = d0+Vector3:new{x=0.0, y=L_B_D*tan_alpha}
61  d2 = d1+Vector3:new{x=0.0, y=H_C}
62
63  -- Outflow points
64
65  e0 = Vector3:new{x=L_B_E, y=0.0}
66  e1 = e0+Vector3:new{x=0.0, y=L_B_D*tan_alpha}
67  e2 = e1+Vector3:new{x=0.0, y=H_C}
68  e3 = e2+Vector3:new{x=0.0, y=((L_B_E - L_B_C)*tan_beta)}
69  e4 = e3+Vector3:new{x=0.0, y=H_E}
70
71  -- Defining Patches
72

```



```

73 patch={}
74 patch[0] = CoonsPatch:new{p00=a0, p10=b0, p11=b1, p01=a1}
75 patch[1] = CoonsPatch:new{p00=a1, p10=b1, p11=b2, p01=a2}
76 patch[2] = CoonsPatch:new{p00=b0, p10=c1, p11=c2, p01=b1}
77 patch[3] = CoonsPatch:new{p00=b1, p10=c2, p11=c3, p01=b2}
78 patch[4] = CoonsPatch:new{p00=c1, p10=d1, p11=d2, p01=c2}
79 patch[5] = CoonsPatch:new{p00=c2, p10=e3, p11=e4, p01=c3}
80 patch[6] = CoonsPatch:new{p00=d1, p10=e1, p11=e2, p01=d2}
81
82 -- Discretization of the flow domain
83 -- Cluster cells on ramp and isolator faces of boundary layer interest
84
85 factor = 15 -- Discretization scale factor
86 ni0 = math.floor(1*factor); nj0 = math.floor(1*factor)
87
88 rcfL = RobertsFunction:new{end0=true, end1=false, beta=1.2} -- Custer only South
89 rcf = RobertsFunction:new{end0=true, end1=true, beta=1.2} -- Custer South and
90 North edge
91
92 grid={}
93 grid[0] = StructuredGrid:new{psurface=patch[0], niv=2*ni0+1, njv=8*nj0+1,
94 cflist={east=rcfL,west=rcfL}}
95 grid[1] = StructuredGrid:new{psurface=patch[1], niv=2*ni0+1, njv=5*nj0+1}
96 grid[2] = StructuredGrid:new{psurface=patch[2], niv=30*ni0+1, njv=8*nj0+1,
97 cflist={east=rcf,west=rcfL}}
98 grid[3] = StructuredGrid:new{psurface=patch[3], niv=30*ni0+1, njv=5*nj0+1}
99 grid[4] = StructuredGrid:new{psurface=patch[4], niv=15*ni0+1, njv=8*nj0+1,
100 cflist={east=rcf,west=rcf}}
101 grid[5] = StructuredGrid:new{psurface=patch[5], niv=15*ni0+1, njv=5*nj0+1}
102 grid[6] = StructuredGrid:new{psurface=patch[6], niv=20*ni0+1, njv=8*nj0+1,
103 cflist={east=rcf,west=rcf}}
104
105 -- Building flow block and setting boundary conditions
106 blk0 = FluidBlockArray{grid=grid[0], initialState=initial, nib=1, njb=5,
107 bcList={west=InFlowBC_Supersonic:new{flowState=inflow}}}
108 blk1 = FluidBlockArray{grid=grid[1], initialState=initial, nib=1, njb=5,
109 bcList={west=InFlowBC_Supersonic:new{flowState=inflow},
110 north=OutFlowBC_FixedPT:new{p_outside=p_inf, T_outside=T_inf}}}
111 blk2 = FluidBlockArray{grid=grid[2], initialState=initial, nib=4, njb=5,
112 bcList={south=WallBC_NoSlip_FixedT:new{Twall=T_ramp}}}
113 blk3 = FluidBlockArray{grid=grid[3], initialState=initial, nib=4, njb=5,
114 bcList={north=OutFlowBC_FixedPT:new{p_outside=p_inf, T_outside=T_inf}}}
115 blk4 = FluidBlockArray{grid=grid[4], initialState=initial, nib=4, njb=5,
116 bcList={north=WallBC_NoSlip_FixedT:new{Twall=T_ramp},
117 south=WallBC_NoSlip_FixedT:new{Twall=T_ramp}}}
118 blk5 = FluidBlockArray{grid=grid[5], initialState=initial, nib=4, njb=5,
119 bcList={north=OutFlowBC_FixedPT:new{p_outside=p_inf, T_outside=T_inf},
120 south=WallBC_WithSlip:new{,
121 east=OutFlowBC_FixedPT:new{p_outside=p_inf, T_outside=T_inf}}}
122 blk6 = FluidBlockArray{grid=grid[6], initialState=initial, nib=4, njb=5,
123 bcList={north=WallBC_NoSlip_FixedT:new{Twall=T_ramp},
124 south=WallBC_NoSlip_FixedT:new{Twall=T_ramp},
125 east=OutFlowBC_FixedPT:new{p_outside=p_inf, T_outside=T_inf}}}
126
127 identifyBlockConnections()
128
129 -- History points
130 a = 112.92*mm -- first pressure transducer location along ramp
131 b = 174.22*mm -- ramp length
132
133 x0 = a*math.cos(alpha)
134 y0 = a*math.sin(alpha)
135 x1 = (a+12*mm)*math.cos(alpha)
136 y1 = (a+12*mm)*math.sin(alpha)
137 x2 = (a+22*mm)*math.cos(alpha)
138 y2 = (a+22*mm)*math.sin(alpha)
139 x3 = (a+32*mm)*math.cos(alpha)
140 y3 = (a+32*mm)*math.sin(alpha)
141 x4 = (a+42*mm)*math.cos(alpha)
142 y4 = (a+42*mm)*math.sin(alpha)

```



```
143 x5 = (a+52*mm)*math.cos(alpha)
144 y5 = (a+52*mm)*math.sin(alpha)
145 x6 = b*math.cos(alpha)+10*mm
146 y6 = b*math.sin(alpha)
147 x7 = x6+15*mm
148 y7 = y6
149
150 setHistoryPoint{x=x0, y=y0}
151 setHistoryPoint{x=x1, y=y1}
152 setHistoryPoint{x=x2, y=y2}
153 setHistoryPoint{x=x3, y=y3}
154 setHistoryPoint{x=x4, y=y4}
155 setHistoryPoint{x=x5, y=y5}
156 setHistoryPoint{x=x6, y=y6}
157 setHistoryPoint{x=x7, y=y7}
158
159 -- Setting history time step recording
160 config.dt_history = 10.0e-5
161
162
163 -- Flow time and step assignment
164
165 config.viscous = true
166 config.cfl_value = 0.5
167 config.max_time = 0.005
168 config.max_step = 2000000
169 config.dt_init = 1.0e-8
170 config.dt_plot = config.max_time/30
```

H.2 Unstart Injection Inlet Script

```

1  -- 12-deg-inlet-unstart.lua
2  -- Lachlan J Noller created 05/03/2019
3  -- Unstart of 2D single ramp inlet with 12 degree ramp from started state with a
   Mach 1 injection is the
4  isolator
5
6  -- Flow Solution from 12-deg-inlet.lua
7  fsol = FlowSolution:new{jobName="12-deg-inlet",
   dir="../../1-START/12-deg-inlet-dis15-v1", tindx=30, nBl
8  ocks=110}
9
10 -- Gas Model
11 nsp, nmodes = setGasModel('ideal-air-gas-model.lua')
12 print("GasModel set to ideal air. nsp= ", nsp, " nmodes= ", nmodes)
13
14 -- Inflow and Injection Flow Conditions
15
16 R = 287 -- Ideal Gas Constant
17 gamma = 1.4 -- N/m^3
18
19 M_inf = 5.85 -- Inflow Mach No.
20 p_inf = 740.0 -- Inflow Pressure (Pa)
21 T_inf = 73.0 -- Inflow Temperature (K)
22 u_inf = M_inf*math.sqrt(gamma*R*T_inf) -- Inflow Velocity (m/s)
23 inflow = FlowState:new{p=p_inf, velx=u_inf, T=T_inf}
24
25 M_inj = 1.0 -- Injection Mach No.
26 p_inj = 100.0e3 -- Injection Pressure (Pa)
27 T_inj = 300.0 -- Injection Temperature (K)
28 u_inj = M_inj*math.sqrt(gamma*R*T_inj) -- Injection Velocity (m/s)
29 injection = FlowState:new{p=p_inj, vely=u_inj, T=T_inj}
30
31 T_ramp = 300 -- degree K
32
33 -- Flow Domain
34
35 mm = 1.0e-3 -- metres per mm
36
37 -- Set measurements
38
39 L_A_B = 10*mm -- i direction inlet to flow domain
40 L_B_D = 170.4*mm -- i direction ramp length
41 L_B_E = 220*mm -- i direction total length
42 L_B_C = 128.6*mm -- i direction distance to cowl lip
43 H_C = 15*mm -- j direction combustor height
44 H_E = 10*mm -- j direction addition flow above cowl
45 alpha = 12*math.pi/180.0 -- Ramp angle (radians)
46 tan_alpha = math.tan(alpha)
47 beta = 10*math.pi/180.0 -- Cowl angle (radians)
48 tan_beta = math.tan(beta)
49 L_F_G = 16.5*mm -- i direction distance after injection
50 L_F_E = 1.0*mm -- i direction unstart injection port
51
52 -- Inflow points
53
54 a0 = Vector3:new{x=-L_A_B, y=0.0}
55 a1 = a0+Vector3:new{x=0.0, y=L_B_D*tan_alpha + H_C}
56 a2 = a1+Vector3:new{x=0.0, y=((L_B_E - L_B_C)*tan_beta) + H_E}
57 b0 = a0+Vector3:new{x=L_A_B, y=0.0}
58 b1 = a1+Vector3:new{x=L_A_B, y=0.0}
59 b2 = a2+Vector3:new{x=L_A_B, y=0.0}
60
61 -- Internal Entrance points
62
63 c0 = b0+Vector3:new{x=L_B_C, y=0.0}
64 c1 = Vector3:new{x=L_B_C, y=L_B_C*tan_alpha}
65 c2 = b1+Vector3:new{x=L_B_C, y=0.0}
66 c3 = b2+Vector3:new{x=L_B_C, y=0.0}
67
68 -- Inlet Throat points
69
70 d0 = Vector3:new{x=L_B_D, y=0.0}

```

```

71 d1 = d0+Vector3:new{x=0.0, y=L_B_D*tan_alpha}
72 d2 = d1+Vector3:new{x=0.0, y=H_C}
73
74 -- Outflow points
75
76 g0 = Vector3:new{x=L_B_E, y=0.0}
77 g1 = g0+Vector3:new{x=0.0, y=L_B_D*tan_alpha}
78 g2 = g1+Vector3:new{x=0.0, y=H_C}
79 g3 = g2+Vector3:new{x=0.0, y=((L_B_E - L_B_C)*tan_beta)}
80 g4 = g3+Vector3:new{x=0.0, y=H_E}
81
82 -- Injection points
83
84 f1 = g1-Vector3:new{x=L_F_G, y=0.0}
85 f2 = g2-Vector3:new{x=L_F_G, y=0.0}
86 e1 = f1-Vector3:new{x=L_F_E, y=0.0}
87 e2 = f2-Vector3:new{x=L_F_E, y=0.0}
88
89 -- Defining Patches
90
91 patch={}
92 patch[0] = CoonsPatch:new{p00=a0, p10=b0, p11=b1, p01=a1}
93 patch[1] = CoonsPatch:new{p00=a1, p10=b1, p11=b2, p01=a2}
94 patch[2] = CoonsPatch:new{p00=b0, p10=c1, p11=c2, p01=b1}
95 patch[3] = CoonsPatch:new{p00=b1, p10=c2, p11=c3, p01=b2}
96 patch[4] = CoonsPatch:new{p00=c1, p10=d1, p11=d2, p01=c2}
97 patch[5] = CoonsPatch:new{p00=c2, p10=g3, p11=g4, p01=c3}
98 patch[6] = CoonsPatch:new{p00=d1, p10=e1, p11=e2, p01=d2}
99 patch[7] = CoonsPatch:new{p00=e1, p10=f1, p11=f2, p01=e2}
100 patch[8] = CoonsPatch:new{p00=f1, p10=g1, p11=g2, p01=f2}
101
102 -- Discretization of the flow domain
103 -- Cluster cells on ramp and isolator faces of boundary layer interest
104
105 factor = 15 -- Discretization scale factor
106 ni0 = math.floor(1*factor); nj0 = math.floor(2*factor)
107
108 rcfL = RobertsFunction:new{end0=true, end1=false, beta=1.1} -- Custer only South
109 rcf = RobertsFunction:new{end0=true, end1=true, beta=1.1} -- Custer South and
110 North edge
111
112 grid={}
113 grid[0] = StructuredGrid:new{psurface=patch[0], niv=2*ni0+1, njv=4*nj0+1,
114   cfList={east=rcfL,west=rcfL}}
115 grid[1] = StructuredGrid:new{psurface=patch[1], niv=2*ni0+1, njv=2*nj0+1}
116 grid[2] = StructuredGrid:new{psurface=patch[2], niv=25*ni0+1, njv=4*nj0+1,
117   cfList={east=rcf,west=rcfL}}
118 grid[3] = StructuredGrid:new{psurface=patch[3], niv=25*ni0+1, njv=2*nj0+1}
119 grid[4] = StructuredGrid:new{psurface=patch[4], niv=10*ni0+1, njv=4*nj0+1,
120   cfList={east=rcf,west=rcf}}
121 grid[5] = StructuredGrid:new{psurface=patch[5], niv=15*ni0+1, njv=2*nj0+1}
122 grid[6] = StructuredGrid:new{psurface=patch[6], niv=10*ni0+1, njv=4*nj0+1,
123   cfList={east=rcf,west=rcf}}
124 grid[7] = StructuredGrid:new{psurface=patch[7], niv=0.5*ni0+1, njv=4*nj0+1,
125   cfList={east=rcf,west=rcf}}
126 grid[8] = StructuredGrid:new{psurface=patch[8], niv=6*ni0+1, njv=4*nj0+1,
127   cfList={east=rcf,west=rcf}}
128
129 -- Building flow block and setting boundary conditions
130
131 n0i = 1
132 n1i = n0i
133 n2i = 4
134 n3i = n2i
135 n4i = 4
136 n5i = 4
137 n6i = 4
138 n7i = 1
139 n8i = 2
140 n0j = 5
141 n2j = n0j

```

```

141 n4j = n0j
142 n6j = n0j
143 n7j = n0j
144 n8j = n0j
145 n1j = 5
146 n3j = n1j
147 n5j = n1j
148
149 blk0 = FluidBlockArray{grid=grid[0], initialState=fsol, nib=n0i, njb=n0j,
150   bcList={west=InFlowBC_Supersonic:new{flowState=inflow}}}
151 blk1 = FluidBlockArray{grid=grid[1], initialState=fsol, nib=n1i, njb=n1j,
152   bcList={west=InFlowBC_Supersonic:new{flowState=inflow},
153     north=OutFlowBC_FixedPT:new{p_outside=p_inf, T_outside=T_inf}}}
154 blk2 = FluidBlockArray{grid=grid[2], initialState=fsol, nib=n2i, njb=n2j,
155   bcList={south=WallBC_NoSlip_FixedT:new{Twall=T_ramp}}}
156 blk3 = FluidBlockArray{grid=grid[3], initialState=fsol, nib=n3i, njb=n3j,
157   bcList={north=OutFlowBC_FixedPT:new{p_outside=p_inf, T_outside=T_inf}}}
158 blk4 = FluidBlockArray{grid=grid[4], initialState=fsol, nib=n4i, njb=n4j,
159   bcList={north=WallBC_NoSlip_FixedT:new{Twall=T_ramp},
160     south=WallBC_NoSlip_FixedT:new{Twall=T_ramp}}}
161 blk5 = FluidBlockArray{grid=grid[5], initialState=fsol, nib=n5i, njb=n5j,
162   bcList={north=OutFlowBC_FixedPT:new{p_outside=p_inf, T_outside=T_inf},
163     south=WallBC_WithSlip:new{},
164     east=OutFlowBC_FixedPT:new{p_outside=p_inf, T_outside=T_inf}}}
165 blk6 = FluidBlockArray{grid=grid[6], initialState=fsol, nib=n6i, njb=n6j,
166   bcList={north=WallBC_NoSlip_FixedT:new{Twall=T_ramp},
167     south=WallBC_NoSlip_FixedT:new{Twall=T_ramp}}}
168 blk7 = FluidBlockArray{grid=grid[7], initialState=fsol, nib=n7i, njb=n7j,
169   bcList={south=InFlowBC_Supersonic:new{flowState=injection},
170     north=WallBC_NoSlip_FixedT:new{Twall=T_ramp}}}
171 blk8 = FluidBlockArray{grid=grid[8], initialState=fsol, nib=n8i, njb=n8j,
172   bcList={north=WallBC_NoSlip_FixedT:new{Twall=T_ramp},
173     south=WallBC_NoSlip_FixedT:new{Twall=T_ramp},
174     east=OutFlowBC_FixedPT:new{p_outside=p_inf, T_outside=T_inf}}}
175
176 identifyBlockConnections()
177
178 -- History points
179 a = 112.92*mm -- first pressure transducer location along ramp
180 b = 174.22*mm -- ramp length
181
182 x0 = a*math.cos(alpha)
183 y0 = a*math.sin(alpha)
184 x1 = (a+10*mm)*math.cos(alpha)
185 y1 = (a+10*mm)*math.sin(alpha)
186 x2 = (a+20*mm)*math.cos(alpha)
187 y2 = (a+20*mm)*math.sin(alpha)
188 x3 = (a+30*mm)*math.cos(alpha)
189 y3 = (a+30*mm)*math.sin(alpha)
190 x4 = (a+40*mm)*math.cos(alpha)
191 y4 = (a+40*mm)*math.sin(alpha)
192 x5 = (a+50*mm)*math.cos(alpha)
193 y5 = (a+50*mm)*math.sin(alpha)
194 x6 = b*math.cos(alpha)+15*mm
195 y6 = b*math.sin(alpha)
196 x7 = x6+10*mm
197 y7 = y6
198
199 setHistoryPoint{x=x0, y=y0}
200 setHistoryPoint{x=x1, y=y1}
201 setHistoryPoint{x=x2, y=y2}
202 setHistoryPoint{x=x3, y=y3}
203 setHistoryPoint{x=x4, y=y4}
204 setHistoryPoint{x=x5, y=y5}
205 setHistoryPoint{x=x6, y=y6}
206 setHistoryPoint{x=x7, y=y7}
207
208 -- Setting history time step recording
209 config.dt_history = 10.0e-5
210
211 -- Flow time and step assignment
212

```

```
213 config.viscous = true
214 config.cfl_value = 0.5
215 config.max_time = 0.005
216 config.max_step = 2000000
217 config.dt_init = 1.0e-8
218 config.dt_plot = config.max_time/30
```

H.3 Unstarted Inlet Script

```

1  -- 12-deg-inlet-unstart-stop.lua
2  -- Lachlan J Noller created 18/02/2019
3  -- Model of 2D single ramp inlet with 12 degree ramp with isolator injection turned
   off attempting to so sustain unstarted flow
4
5
6  config.title = "2D Inlet with 12 degree ramp"
7  print(config.title)
8  config.dimensions = 2
9
10 -- Flow conditions
11
12 R = 287
13 gamma = 1.4
14 M_inf = 5.85
15 p_inf = 740 -- Pa
16 T_inf = 73 -- degree K
17 u_inf = M_inf*math.sqrt(gamma*R*T_inf) -- m/s
18
19 T_ramp = 300 -- degree K
20
21 nsp, nmodes = setGasModel('ideal-air-gas-model.lua')
22 print("GasModel set to ideal air. nsp= ", nsp, " nmodes= ", nmodes)
23 inflow = FlowState:new{p=p_inf, velx=u_inf, T=T_inf}
24
25
26 -- Flow Solution from 12-deg-inlet-unstart.lua
27 fsol = FlowSolution:new{jobName="12-deg-inlet-unstart",
   dir="../../2-UNSTART_INJECTION/12-deg-inlet-unstart-dis15-v1-100kPa", tindx=30,
   nBlocks=125}
28
29 -- Flow Domain
30
31 mm = 1.0e-3 -- metres per mm
32
33 -- Set measurements
34
35 L_A_B = 10*mm -- i direction inlet to flow domain
36 L_B_D = 170.4*mm -- i direction ramp length
37 L_B_E = 220*mm -- i direction total length
38 L_B_C = 128.6*mm -- i direction distance to cowl lip from origin
39 H_C = 15*mm -- j direction combustor height
40 H_E = 10*mm -- j direction addition flow above cowl
41 alpha = 12*math.pi/180.0 -- Ramp angle (radians)
42 tan_alpha = math.tan(alpha)
43 beta = 10*math.pi/180.0 -- Cowl angle (radians)
44 tan_beta = math.tan(beta)
45
46 -- Inflow points
47
48 a0 = Vector3:new{x=-L_A_B, y=0.0}
49 a1 = a0+Vector3:new{x=0.0, y=L_B_D*tan_alpha + H_C}
50 a2 = a1+Vector3:new{x=0.0, y=((L_B_E - L_B_C)*tan_beta) + H_E}
51 b0 = a0+Vector3:new{x=L_A_B, y=0.0}
52 b1 = a1+Vector3:new{x=L_A_B, y=0.0}
53 b2 = a2+Vector3:new{x=L_A_B, y=0.0}
54
55 -- Internal Entrance points
56
57 c0 = b0+Vector3:new{x=L_B_C, y=0.0}
58 c1 = Vector3:new{x=L_B_C, y=L_B_C*tan_alpha}
59 c2 = b1+Vector3:new{x=L_B_C, y=0.0}
60 c3 = b2+Vector3:new{x=L_B_C, y=0.0}
61
62 -- Inlet Throat points
63
64 d0 = Vector3:new{x=L_B_D, y=0.0}
65 d1 = d0+Vector3:new{x=0.0, y=L_B_D*tan_alpha}
66 d2 = d1+Vector3:new{x=0.0, y=H_C}
67
68 -- Outflow points
69

```

```

70 e0 = Vector3:new{x=L_B_E, y=0.0}
71 e1 = e0+Vector3:new{x=0.0, y=L_B_D*tan_alpha}
72 e2 = e1+Vector3:new{x=0.0, y=H_C}
73 e3 = e2+Vector3:new{x=0.0, y=((L_B_E - L_B_C)*tan_beta)}
74 e4 = e3+Vector3:new{x=0.0, y=H_E}
75
76 -- Defining Patches
77
78 patch={}
79 patch[0] = CoonsPatch:new{p00=a0, p10=b0, p11=b1, p01=a1}
80 patch[1] = CoonsPatch:new{p00=a1, p10=b1, p11=b2, p01=a2}
81 patch[2] = CoonsPatch:new{p00=b0, p10=c1, p11=c2, p01=b1}
82 patch[3] = CoonsPatch:new{p00=b1, p10=c2, p11=c3, p01=b2}
83 patch[4] = CoonsPatch:new{p00=c1, p10=d1, p11=d2, p01=c2}
84 patch[5] = CoonsPatch:new{p00=c2, p10=e3, p11=e4, p01=c3}
85 patch[6] = CoonsPatch:new{p00=d1, p10=e1, p11=e2, p01=d2}
86
87 -- Discretization of the flow domain
88 -- Cluster cells on ramp and isolator faces of boundary layer interest
89
90 factor = 15 -- Discretization scale factor
91 ni0 = math.floor(1*factor); nj0 = math.floor(2*factor)
92
93 rcfL = RobertsFunction:new{end0=true, end1=false, beta=1.2} -- Cluster only South
94 rcf = RobertsFunction:new{end0=true, end1=true, beta=1.2} -- Cluster South and
95 North edge
96
97 grid={}
98 grid[0] = StructuredGrid:new{psurface=patch[0], niv=2*ni0+1, njv=8*nj0+1,
99 cfList={east=rcfL,west=rcfL}}
100 grid[1] = StructuredGrid:new{psurface=patch[1], niv=2*ni0+1, njv=5*nj0+1}
101 grid[2] = StructuredGrid:new{psurface=patch[2], niv=30*ni0+1, njv=8*nj0+1,
102 cfList={east=rcf,west=rcfL}}
103 grid[3] = StructuredGrid:new{psurface=patch[3], niv=30*ni0+1, njv=5*nj0+1}
104 grid[4] = StructuredGrid:new{psurface=patch[4], niv=15*ni0+1, njv=8*nj0+1,
105 cfList={east=rcf,west=rcf}}
106 grid[5] = StructuredGrid:new{psurface=patch[5], niv=15*ni0+1, njv=5*nj0+1}
107 grid[6] = StructuredGrid:new{psurface=patch[6], niv=20*ni0+1, njv=8*nj0+1,
108 cfList={east=rcf,west=rcf}}
109
110 -- Building flow block and setting boundary conditions
111
112 blk0 = FluidBlockArray{grid=grid[0], initialState=fsol, nib=1, njb=5,
113 bcList={west=InFlowBC_Supersonic:new{flowState=inflow}}}
114 blk1 = FluidBlockArray{grid=grid[1], initialState=fsol, nib=1, njb=5,
115 bcList={west=InFlowBC_Supersonic:new{flowState=inflow},
116 north=OutFlowBC_FixedPT:new{p_outside=p_inf, T_outside=T_inf}}}
117 blk2 = FluidBlockArray{grid=grid[2], initialState=fsol, nib=4, njb=5,
118 bcList={south=WallBC_NoSlip_FixedT:new{Twall=T_ramp}}}
119 blk3 = FluidBlockArray{grid=grid[3], initialState=fsol, nib=4, njb=5,
120 bcList={north=OutFlowBC_FixedPT:new{p_outside=p_inf, T_outside=T_inf}}}
121 blk4 = FluidBlockArray{grid=grid[4], initialState=fsol, nib=4, njb=5,
122 bcList={north=WallBC_NoSlip_FixedT:new{Twall=T_ramp},
123 south=WallBC_NoSlip_FixedT:new{Twall=T_ramp}}}
124 blk5 = FluidBlockArray{grid=grid[5], initialState=fsol, nib=4, njb=5,
125 bcList={north=OutFlowBC_FixedPT:new{p_outside=p_inf, T_outside=T_inf},
126 south=WallBC_WithSlip:new{},
127 east=OutFlowBC_SimpleExtrapolate:new{xOrder=0}}}
128 blk6 = FluidBlockArray{grid=grid[6], initialState=fsol, nib=4, njb=5,
129 bcList={north=WallBC_NoSlip_FixedT:new{Twall=T_ramp},
130 south=WallBC_NoSlip_FixedT:new{Twall=T_ramp},
131 east=OutFlowBC_FixedPT:new{p_outside=p_inf, T_outside=T_inf}}}
132
133 identifyBlockConnections()
134
135 -- History points
136 a = 112.92*mm -- first pressure transducer location along ramp
137 b = 174.22*mm -- ramp length
138
139 x0 = a*math.cos(alpha)
140 y0 = a*math.sin(alpha)

```

```
140 x1 = (a+10*mm)*math.cos(alpha)
141 y1 = (a+10*mm)*math.sin(alpha)
142 x2 = (a+20*mm)*math.cos(alpha)
143 y2 = (a+20*mm)*math.sin(alpha)
144 x3 = (a+30*mm)*math.cos(alpha)
145 y3 = (a+30*mm)*math.sin(alpha)
146 x4 = (a+40*mm)*math.cos(alpha)
147 y4 = (a+40*mm)*math.sin(alpha)
148 x5 = (a+50*mm)*math.cos(alpha)
149 y5 = (a+50*mm)*math.sin(alpha)
150 x6 = b*math.cos(alpha)+15*mm
151 y6 = 41.22*mm
152 x7 = x6+10*mm
153 y7 = y6
154
155 setHistoryPoint{x=x0, y=y0}
156 setHistoryPoint{x=x1, y=y1}
157 setHistoryPoint{x=x2, y=y2}
158 setHistoryPoint{x=x3, y=y3}
159 setHistoryPoint{x=x4, y=y4}
160 setHistoryPoint{x=x5, y=y5}
161 setHistoryPoint{x=x6, y=y6}
162 setHistoryPoint{x=x7, y=y7}
163
164 -- Setting history time step recording
165 config.dt_history = 10.0e-5
166
167 -- Flow time and step assignment
168
169 config.viscous = true
170 config.cfl_value = 0.5
171 config.max_time = 0.005
172 config.max_step = 2000000
173 config.dt_init = 1.0e-8
174 config.dt_plot = config.max_time/30
```


H.4 Restart Mechanism Inlet Script

```

1  -- 12-deg-inlet-restart-mech.lua
2  -- Lachlan J Noller created 26/07/2019
3  -- Restart mechanism with ramp tip injection applied to 2D single ramp inlet with 12
   degree ramp from unstarted state
4
5  -- Flow Solution
6  fsol = FlowSolution:new{jobName="12-deg-inlet-unstart-stop",
   dir="../../3-UNSTART_STOP/12-deg-inlet-unstart-stop-100kPa", tindx=30, nBlocks=110}
7
8  -- Gas Model
9  nsp, nmodes = setGasModel('ideal-air-gas-model.lua')
10 print("GasModel set to ideal air. nsp= ", nsp, " nmodes= ", nmodes)
11
12 -- Inflow and Injection Flow Conditions
13
14 R = 287 -- Ideal Gas Constant
15 gamma = 1.4 -- N/m^3
16
17 M_inf = 5.85 -- Inflow Mach No.
18 p_inf = 740.0 -- Inflow Pressure (Pa)
19 T_inf = 73.0 -- Inflow Temperature (K)
20 u_inf = M_inf*math.sqrt(gamma*R*T_inf) -- Inflow Velocity (m/s)
21 inflow = FlowState:new{p=p_inf, velx=u_inf, T=T_inf}
22
23 M_inj = 1.0 -- Injection Mach No.
24 p_inj = 100.0e3 -- Injection Pressure (Pa)
25 T_inj = 300.0 -- Injection Temperature (K)
26 u_inj = M_inj*math.sqrt(gamma*R*T_inj) -- Injection Velocity (m/s)
27 injection = FlowState:new{p=p_inj, vely=u_inj, T=T_inj}
28 T_ramp = 300 -- Degree K
29 -- Flow Domain
30
31 mm = 1.0e-3 -- metres per mm
32
33 -- Set measurements
34
35 L_A_B = 10*mm -- i direction inlet to flow domain
36 L_B_F = 170.4*mm -- i direction ramp length
37 L_B_G = 220*mm -- i direction total length
38 L_B_E = 128.6*mm -- i direction distance to cowl lip
39 H_C = 15*mm -- j direction combustor height
40 H_E = 10*mm -- j direction addition flow above cowl
41 alpha = 12*math.pi/180.0 -- Ramp angle (radians)
42 tan_alpha = math.tan(alpha)
43 beta = 10*math.pi/180.0 -- Cowl angle (radians)
44 tan_beta = math.tan(beta)
45 L_B_C = 10*mm -- i direction ramp tip to injection
46 L_C_D = 1*mm -- i direction slot injection width
47
48 -- Inflow points
49
50 a0 = Vector3:new{x=-L_A_B, y=0.0}
51 a1 = a0+Vector3:new{x=0.0, y=L_B_F*tan_alpha + H_C}
52 a2 = a1+Vector3:new{x=0.0, y=((L_B_G - L_B_E)*tan_beta) + H_E}
53 b0 = a0+Vector3:new{x=L_A_B, y=0.0}
54 b1 = a1+Vector3:new{x=L_A_B, y=0.0}
55 b2 = a2+Vector3:new{x=L_A_B, y=0.0}
56
57 -- Injection Points
58 c0 = b0+Vector3:new{x=L_B_C, y=0.0}
59 c1 = c0+Vector3:new{x=0.0, y=L_B_C*tan_alpha}
60 c2 = b1+Vector3:new{x=L_B_C, y=0.0}
61 c3 = b2+Vector3:new{x=L_B_C, y=0.0}
62 d0 = c0+Vector3:new{x=L_C_D, y=0.0}
63 d1 = c1+Vector3:new{x=L_C_D, y=L_C_D*tan_alpha}
64 d2 = c2+Vector3:new{x=L_C_D, y=0.0}
65 d3 = c3+Vector3:new{x=L_C_D, y=0.0}
66
67 -- Internal Entrance points
68
69 e0 = b0+Vector3:new{x=L_B_E, y=0.0}
70 e1 = Vector3:new{x=L_B_E, y=L_B_E*tan_alpha}

```

```

71 e2 = b1+Vector3:new{x=L_B_E, y=0.0}
72 e3 = b2+Vector3:new{x=L_B_E, y=0.0}
73
74 -- Inlet Throat points
75
76 f0 = Vector3:new{x=L_B_F, y=0.0}
77 f1 = f0+Vector3:new{x=0.0, y=L_B_F*tan_alpha}
78 f2 = f1+Vector3:new{x=0.0, y=H_C}
79
80 -- Outflow points
81
82 g0 = Vector3:new{x=L_B_G, y=0.0}
83 g1 = g0+Vector3:new{x=0.0, y=L_B_F*tan_alpha}
84 g2 = g1+Vector3:new{x=0.0, y=H_C}
85 g3 = g2+Vector3:new{x=0.0, y=((L_B_G - L_B_E)*tan_beta)}
86 g4 = g3+Vector3:new{x=0.0, y=H_E}
87
88 -- Defining Patches
89
90 patch={}
91 patch[0] = CoonsPatch:new{p00=a0, p10=b0, p11=b1, p01=a1}
92 patch[1] = CoonsPatch:new{p00=a1, p10=b1, p11=b2, p01=a2}
93 patch[2] = CoonsPatch:new{p00=b0, p10=c1, p11=c2, p01=b1}
94 patch[3] = CoonsPatch:new{p00=b1, p10=c2, p11=c3, p01=b2}
95 patch[4] = CoonsPatch:new{p00=c1, p10=d1, p11=d2, p01=c2}
96 patch[5] = CoonsPatch:new{p00=c2, p10=d2, p11=d3, p01=c3}
97 patch[6] = CoonsPatch:new{p00=d1, p10=e1, p11=e2, p01=d2}
98 patch[7] = CoonsPatch:new{p00=d2, p10=e2, p11=e3, p01=d3}
99 patch[8] = CoonsPatch:new{p00=e1, p10=f1, p11=f2, p01=e2}
100 patch[9] = CoonsPatch:new{p00=e2, p10=g3, p11=g4, p01=e3}
101 patch[10] = CoonsPatch:new{p00=f1, p10=g1, p11=g2, p01=f2}
102
103 -- Discretization of the flow domain
104 -- Cluster cells on ramp and isolator faces of boundary layer interest
105
106 factor = 15 -- Discretization scale factor
107 ni0 = math.floor(1*factor); nj0 = math.floor(2*factor)
108
109 rcfL = RobertsFunction:new{end0=true, end1=false, beta=1.1} -- Cluster only South
110 edge
111 rcf = RobertsFunction:new{end0=true, end1=true, beta=1.1} -- Cluster South and
112 North edge
113
114 grid={}
115 grid[0] = StructuredGrid:new{psurface=patch[0], niv=2*ni0+1, njv=4*nj0+1,
116 cfList={east=rcfL,west=rcfL}}
117 grid[1] = StructuredGrid:new{psurface=patch[1], niv=2*ni0+1, njv=2*nj0+1}
118 grid[2] = StructuredGrid:new{psurface=patch[2], niv=2*ni0+1, njv=4*nj0+1,
119 cfList={east=rcfL,west=rcfL}}
120 grid[3] = StructuredGrid:new{psurface=patch[3], niv=2*ni0+1, njv=2*nj0+1}
121 grid[4] = StructuredGrid:new{psurface=patch[4], niv=0.5*ni0+1, njv=4*nj0+1,
122 cfList={east=rcfL,west=rcfL}}
123 grid[5] = StructuredGrid:new{psurface=patch[5], niv=0.5*ni0+1, njv=2*nj0+1}
124 grid[6] = StructuredGrid:new{psurface=patch[6], niv=16*ni0+1, njv=4*nj0+1,
125 cfList={east=rcf,west=rcfL}}
126 grid[7] = StructuredGrid:new{psurface=patch[7], niv=16*ni0+1, njv=2*nj0+1}
127 grid[8] = StructuredGrid:new{psurface=patch[8], niv=6*ni0+1, njv=4*nj0+1,
128 cfList={east=rcf,west=rcf}}
129 grid[9] = StructuredGrid:new{psurface=patch[9], niv=12*ni0+1, njv=2*nj0+1}
130 grid[10] = StructuredGrid:new{psurface=patch[10], niv=8*ni0+1, njv=4*nj0+1,
131 cfList={east=rcf,west=rcf}}
132
133 -- Building flow block and setting boundary conditions
134
135 n0i = 1
136 n1i = n0i
137 n2i = 1
138 n3i = n2i
139 n4i = 1
140 n5i = n4i
141 n6i = 8
142 n7i = n6i

```

```

141  n8i = 2
142  n9i = 4
143  n10i = 3
144  n0j = 5
145  n2j = n0j
146  n4j = n0j
147  n6j = n0j
148  n8j = n0j
149  n10j = n0j
150  n1j = 5
151  n3j = n1j
152  n5j = n1j
153  n7j = n1j
154  n9j = n1j
155
156  blk0 = FluidBlockArray{grid=grid[0], initialState=fsol, nib=n0i, njb=n0j,
157      bcList={west=InFlowBC_Supersonic:new{flowState=inflow}}}
158  blk1 = FluidBlockArray{grid=grid[1], initialState=fsol, nib=n1i, njb=n1j,
159      bcList={west=InFlowBC_Supersonic:new{flowState=inflow},
160      north=OutFlowBC_FixedPT:new{p_outside=p_inf, T_outside=T_inf}}}
161  blk2 = FluidBlockArray{grid=grid[2], initialState=fsol, nib=n2i, njb=n2j,
162      bcList={south=WallBC_NoSlip_FixedT:new{Twall=T_ramp}}}
163  blk3 = FluidBlockArray{grid=grid[3], initialState=fsol, nib=n3i, njb=n3j,
164      bcList={north=OutFlowBC_FixedPT:new{p_outside=p_inf, T_outside=T_inf}}}
165  blk4 = FluidBlockArray{grid=grid[4], initialState=fsol, nib=n4i, njb=n4j,
166      bcList={south=InFlowBC_Supersonic:new{flowState=injection}}}
167  blk5 = FluidBlockArray{grid=grid[5], initialState=fsol, nib=n5i, njb=n5j,
168      bcList={north=OutFlowBC_FixedPT:new{p_outside=p_inf, T_outside=T_inf}}}
169  blk6 = FluidBlockArray{grid=grid[6], initialState=fsol, nib=n6i, njb=n6j,
170      bcList={south=WallBC_NoSlip_FixedT:new{Twall=T_ramp}}}
171  blk7 = FluidBlockArray{grid=grid[7], initialState=fsol, nib=n7i, njb=n7j,
172      bcList={north=OutFlowBC_FixedPT:new{p_outside=p_inf, T_outside=T_inf}}}
173  blk8 = FluidBlockArray{grid=grid[8], initialState=fsol, nib=n8i, njb=n8j,
174      bcList={north=WallBC_NoSlip_FixedT:new{Twall=T_ramp},
175      south=WallBC_NoSlip_FixedT:new{Twall=T_ramp}}}
176  blk9 = FluidBlockArray{grid=grid[9], initialState=fsol, nib=n9i, njb=n9j,
177      bcList={north=OutFlowBC_FixedPT:new{p_outside=p_inf, T_outside=T_inf},
178      south=WallBC_WithSlip:new{},
179      east=OutFlowBC_FixedPT:new{p_outside=p_inf, T_outside=T_inf}}}
180  blk10 = FluidBlockArray{grid=grid[10], initialState=fsol, nib=n10i, njb=n10j,
181      bcList={north=WallBC_NoSlip_FixedT:new{Twall=T_ramp},
182      south=WallBC_NoSlip_FixedT:new{Twall=T_ramp},
183      east=OutFlowBC_FixedPT:new{p_outside=p_inf, T_outside=T_inf}}}
184
185  identifyBlockConnections()
186
187  -- History points
188  a = 112.92*mm -- first pressure transducer location along ramp
189  b = 174.22*mm -- ramp length
190
191  x0 = a*math.cos(alpha)
192  y0 = a*math.sin(alpha)
193  x1 = (a+10*mm)*math.cos(alpha)
194  y1 = (a+10*mm)*math.sin(alpha)
195  x2 = (a+20*mm)*math.cos(alpha)
196  y2 = (a+20*mm)*math.sin(alpha)
197  x3 = (a+30*mm)*math.cos(alpha)
198  y3 = (a+30*mm)*math.sin(alpha)
199  x4 = (a+40*mm)*math.cos(alpha)
200  y4 = (a+40*mm)*math.sin(alpha)
201  x5 = (a+50*mm)*math.cos(alpha)
202  y5 = (a+50*mm)*math.sin(alpha)
203  x6 = b*math.cos(alpha)+15*mm
204  y6 = b*math.sin(alpha)
205  x7 = x6+10*mm
206  y7 = y6
207
208  setHistoryPoint{x=x0, y=y0}
209  setHistoryPoint{x=x1, y=y1}
210  setHistoryPoint{x=x2, y=y2}
211  setHistoryPoint{x=x3, y=y3}
212  setHistoryPoint{x=x4, y=y4}

```

H.5 Restarted Inlet Script

```

1  -- 12-deg-inlet-restart.lua
2  -- Lachlan J Noller created 18/02/2019
3  -- Model of 2D single ramp inlet with 12 degree ramp with restart mechanism removed
   to see if the inlet will restart
4
5
6  config.title = "2D Inlet with 12 degree ramp"
7  print(config.title)
8  config.dimensions = 2
9
10 -- Flow conditions
11
12 R = 287
13 gamma = 1.4
14 M_inf = 5.85
15 p_inf = 740 -- Pa
16 T_inf = 73 -- degree K
17 u_inf = M_inf*math.sqrt(gamma*R*T_inf) -- m/s
18 T_ramp = 300 -- degree K
19
20 nsp, nmodes = setGasModel('ideal-air-gas-model.lua')
21 print("GasModel set to ideal air. nsp= ", nsp, " nmodes= ", nmodes)
22 inflow = FlowState:new{p=p_inf, velx=u_inf, T=T_inf}
23
24
25 -- Flow Solution from 12-deg-inlet-unstart.lua
26 fsol = FlowSolution:new{jobName="12-deg-inlet-restart-mech",
   dir="../../4-RESTART_MECHANSIM/12-deg-inlet-restart-mech-dis15-100kPa-1ms",
   tindx=30, nBlocks=155}
27
28 -- Flow Domain
29
30 mm = 1.0e-3 -- metres per mm
31
32 -- Set measurements
33
34 L_A_B = 10*mm -- i direction inlet to flow domain
35 L_B_D = 170.4*mm -- i direction ramp length
36 L_B_E = 220*mm -- i direction total length
37 L_B_C = 128.6*mm -- i direction distance to cowl lip from origin
38 H_C = 15*mm -- j direction combustor height
39 H_E = 10*mm -- j direction addition flow above cowl
40 alpha = 12*math.pi/180.0 -- Ramp angle (radians)
41 tan_alpha = math.tan(alpha)
42 beta = 10*math.pi/180.0 -- Cowl angle (radians)
43 tan_beta = math.tan(beta)
44
45 -- Inflow points
46
47 a0 = Vector3:new{x=-L_A_B, y=0.0}
48 a1 = a0+Vector3:new{x=0.0, y=L_B_D*tan_alpha + H_C}
49 a2 = a1+Vector3:new{x=0.0, y=((L_B_E - L_B_C)*tan_beta) + H_E}
50 b0 = a0+Vector3:new{x=L_A_B, y=0.0}
51 b1 = a1+Vector3:new{x=L_A_B, y=0.0}
52 b2 = a2+Vector3:new{x=L_A_B, y=0.0}
53
54 -- Internal Entrance points
55
56 c0 = b0+Vector3:new{x=L_B_C, y=0.0}
57 c1 = Vector3:new{x=L_B_C, y=L_B_C*tan_alpha}
58 c2 = b1+Vector3:new{x=L_B_C, y=0.0}
59 c3 = b2+Vector3:new{x=L_B_C, y=0.0}
60
61
62 -- Inlet Throat points
63
64 d0 = Vector3:new{x=L_B_D, y=0.0}
65 d1 = d0+Vector3:new{x=0.0, y=L_B_D*tan_alpha}
66 d2 = d1+Vector3:new{x=0.0, y=H_C}
67
68 -- Outflow points
69

```

```

70 e0 = Vector3:new{x=L_B_E, y=0.0}
71 e1 = e0+Vector3:new{x=0.0, y=L_B_D*tan_alpha}
72 e2 = e1+Vector3:new{x=0.0, y=H_C}
73 e3 = e2+Vector3:new{x=0.0, y=((L_B_E - L_B_C)*tan_beta)}
74 e4 = e3+Vector3:new{x=0.0, y=H_E}
75
76 -- Defining Patches
77
78 patch={}
79 patch[0] = CoonsPatch:new{p00=a0, p10=b0, p11=b1, p01=a1}
80 patch[1] = CoonsPatch:new{p00=a1, p10=b1, p11=b2, p01=a2}
81 patch[2] = CoonsPatch:new{p00=b0, p10=c1, p11=c2, p01=b1}
82 patch[3] = CoonsPatch:new{p00=b1, p10=c2, p11=c3, p01=b2}
83 patch[4] = CoonsPatch:new{p00=c1, p10=d1, p11=d2, p01=c2}
84 patch[5] = CoonsPatch:new{p00=c2, p10=e3, p11=e4, p01=c3}
85 patch[6] = CoonsPatch:new{p00=d1, p10=e1, p11=e2, p01=d2}
86
87 -- Discretization of the flow domain
88 -- Cluster cells on ramp and isolator faces of boundary layer interest
89
90 factor = 15 -- Discretization scale factor
91 ni0 = math.floor(1*factor); nj0 = math.floor(2*factor)
92
93 rcfL = RobertsFunction:new{end0=true, end1=false, beta=1.2} -- Cluster only South
94 rcf = RobertsFunction:new{end0=true, end1=true, beta=1.2} -- Cluster South and
95 North edge
96
97 grid={}
98 grid[0] = StructuredGrid:new{psurface=patch[0], niv=2*ni0+1, njv=8*nj0+1,
99 cfList={east=rcfL,west=rcfL}}
100 grid[1] = StructuredGrid:new{psurface=patch[1], niv=2*ni0+1, njv=5*nj0+1}
101 grid[2] = StructuredGrid:new{psurface=patch[2], niv=30*ni0+1, njv=8*nj0+1,
102 cfList={east=rcf,west=rcfL}}
103 grid[3] = StructuredGrid:new{psurface=patch[3], niv=30*ni0+1, njv=5*nj0+1}
104 grid[4] = StructuredGrid:new{psurface=patch[4], niv=15*ni0+1, njv=8*nj0+1,
105 cfList={east=rcf,west=rcf}}
106 grid[5] = StructuredGrid:new{psurface=patch[5], niv=15*ni0+1, njv=5*nj0+1}
107 grid[6] = StructuredGrid:new{psurface=patch[6], niv=20*ni0+1, njv=8*nj0+1,
108 cfList={east=rcf,west=rcf}}
109
110 -- Building flow block and setting boundary conditions
111
112 blk0 = FluidBlockArray{grid=grid[0], initialState=fsol, nib=1, njb=5,
113 bcList={west=InFlowBC_Supersonic:new{flowState=inflow}}}
114 blk1 = FluidBlockArray{grid=grid[1], initialState=fsol, nib=1, njb=5,
115 bcList={west=InFlowBC_Supersonic:new{flowState=inflow},
116 north=OutFlowBC_FixedPT:new{p_outside=p_inf, T_outside=T_inf}}}
117 blk2 = FluidBlockArray{grid=grid[2], initialState=fsol, nib=4, njb=5,
118 bcList={south=WallBC_NoSlip_FixedT:new{Twall=T_ramp}}}
119 blk3 = FluidBlockArray{grid=grid[3], initialState=fsol, nib=4, njb=5,
120 bcList={north=OutFlowBC_FixedPT:new{p_outside=p_inf, T_outside=T_inf}}}
121 blk4 = FluidBlockArray{grid=grid[4], initialState=fsol, nib=4, njb=5,
122 bcList={north=WallBC_NoSlip_FixedT:new{Twall=T_ramp},
123 south=WallBC_NoSlip_FixedT:new{Twall=T_ramp}}}
124 blk5 = FluidBlockArray{grid=grid[5], initialState=fsol, nib=4, njb=5,
125 bcList={north=OutFlowBC_FixedPT:new{p_outside=p_inf, T_outside=T_inf},
126 south=WallBC_WithSlip:new{},
127 east=OutFlowBC_FixedPT:new{p_outside=p_inf, T_outside=T_inf}}}
128 blk6 = FluidBlockArray{grid=grid[6], initialState=fsol, nib=4, njb=5,
129 bcList={north=WallBC_NoSlip_FixedT:new{Twall=T_ramp},
130 south=WallBC_NoSlip_FixedT:new{Twall=T_ramp},
131 east=OutFlowBC_FixedPT:new{p_outside=p_inf, T_outside=T_inf}}}
132
133 identifyBlockConnections()
134
135 -- History points
136 a = 112.92*mm -- first pressure transducer location along ramp
137 b = 174.22*mm -- ramp length
138
139 x0 = a*math.cos(alpha)
140 y0 = a*math.sin(alpha)

```

```
140 x1 = (a+10*mm)*math.cos(alpha)
141 y1 = (a+10*mm)*math.sin(alpha)
142 x2 = (a+20*mm)*math.cos(alpha)
143 y2 = (a+20*mm)*math.sin(alpha)
144 x3 = (a+30*mm)*math.cos(alpha)
145 y3 = (a+30*mm)*math.sin(alpha)
146 x4 = (a+40*mm)*math.cos(alpha)
147 y4 = (a+40*mm)*math.sin(alpha)
148 x5 = (a+50*mm)*math.cos(alpha)
149 y5 = (a+50*mm)*math.sin(alpha)
150 x6 = b*math.cos(alpha)+15*mm
151 y6 = 41.22*mm
152 x7 = x6+10*mm
153 y7 = y6
154
155 setHistoryPoint{x=x0, y=y0}
156 setHistoryPoint{x=x1, y=y1}
157 setHistoryPoint{x=x2, y=y2}
158 setHistoryPoint{x=x3, y=y3}
159 setHistoryPoint{x=x4, y=y4}
160 setHistoryPoint{x=x5, y=y5}
161 setHistoryPoint{x=x6, y=y6}
162 setHistoryPoint{x=x7, y=y7}
163
164 -- Setting history time step recording
165 config.dt_history = 10.0e-5
166
167 -- Flow time and step assignment
168
169 config.viscous = true
170 config.cfl_value = 0.5
171 config.max_time = 0.005
172 config.max_step = 2000000
173 config.dt_init = 1.0e-8
174 config.dt_plot = config.max_time/30
175
```